THESIS FOR THE DEGREE OF DOCTOR OF PHILOSOPHY

Reducing Alkali Chloride-Induced High Temperature Corrosion by Sulphur Containing Additives

A Combined Laboratory and Field Study

SOFIA KARLSSON

Reducing Alkali Chloride-Induced High Temperature Corrosion by Sulphur Containing Additives

A Combined Laboratory and Field Study

Sofia Karlsson

Cover: BSE image of a cross-section of a 304L sample exposed in a waste-fired boiler for 24 hours at 600°C.

Reducing Alkali Chloride-Induced High Temperature Corrosion by Sulphur Containing
Additives – A Combined Laboratory and Field Study
Sofia Karlsson
Department of Chemistry and Chemical Engineering
Chalmers University of Technology

ASTRACT

In order to achieve a more sustainable society renewable fuels such as biomass and waste are attractive alternatives to fossil fuels for power production. However, fireside corrosion is a serious concern in boilers combusting biomass or waste. The high corrosion rates are often linked to large amounts of alkali chlorides in the flue gas. One way of mitigating the corrosion is to change the corrosive environment in the boiler, e.g. by increasing the availability of $SO_x(g)$ in order to sulphate the alkali chlorides to less corrosive alkali sulphates. However, the reaction releases the corrosive gas HCl and the presence of high concentrations of SO_2 is often associated with increased corrosion rates. Hence, this thesis aims to investigate the interplay between different corrosion mechanisms by connecting the reaction kinetics to the corrosion attacks.

The results showed that the presence of KCl accelerated the corrosion of the stainless steel 304L by two types of corrosion attack: general corrosion and steel grain boundary attack. The general corrosion has been proved to be initiated by chromate formation while the steel grain boundary attack is suggested to be accelerated by HCl, released from the chromate formation reaction.

Increasing the availability of $SO_x(g)$ in the flue gas was shown to decrease the corrosion rate. If the alkali chlorides were sulphated in the flue gas a non-corrosive deposit was formed on the steel and the corrosion attack was negligible. However, during a simultaneous presence of $SO_x(g)$ and alkali chlorides (e.g. KCl(s)) on the steel surface, competing reactions such as sulphation of the alkali chloride and chromate formation occurred. The chromate formation resulted in a general corrosion attack. However, the oxide growth was significantly reduced due to the fast simultaneous sulphation of the alkali chlorides. In contrast, the steel grain boundary attack increased in the presence of SO_2. It is proposed that this attack is accelerated by HCl released from the sulphation reaction as well as metal sulphides formation in the steel grain boundaries.

Keywords: High Temperature Corrosion, Biomass, Waste, Stainless Steels, Alkali Chlorides, Sulphur, Additives, Co-combustion

List of publications

This thesis is based primarily on the work contained in the following appended papers.

Paper I
Karlsson, S., Pettersson, J., Johansson, L.-G., Svensson, J.-E.
"Alkali Induced High Temperature Corrosion of Stainless Steel – The Influence of NaCl, KCl and CaCl$_2$"
Oxidation of Metals, (2012), **78**, (1-2), pp 83-102.

Paper II
Karlsson, S., Pettersson, J., Svensson, J.-E., Johansson, L.-G.
"KCl-Induced High Temperature Corrosion of Austenitic Stainless Steel 304L – The Influence of SO$_2$"
Material Science Forum, (2011), **696**, pp 224-229.

Paper III
Karlsson, S., Åmand, L.-E., Liske, J.
"Reducing high-temperature corrosion on high-alloyed stainless steel superheaters by co-combustion of municipal sewage sludge in a fluidised bed boiler"
Fuel, (2015), **139**, pp 482–493.

Paper IV
Karlsson, S., Jonsson, T., Hall, J., Svensson J.-E., Liske, J.
"Mitigation of Fireside Corrosion of Stainless Steel in Power Plants: A Laboratory Study of the Influences of SO$_2$ and KCl on Initial Stages of Corrosion"
Energy Fuels (2014), **28**, 3102−3109

Paper V
Jonsson, T., Karlsson, S., Hooshyar, H., Sattari, M, Liske, J., Svensson, J.-E., Johansson, L.-G.
"Oxidation after breakdown of the chromium-rich scale on stainless steels at high temperature"
Submitted to Oxidation of Metals

Paper VI
Paz, M. D., Zhao, D., Karlsson, S., Liske, J., Jonsson, T.
"Investigating Corrosion Memory – The influence of historic boiler operation on current corrosion rate"
Impacts of Fuel Quality on Power Production (2014)*,* Utah, USA, Conference paper

Paper VII
Karlsson, S., Jonsson, T., Svensson, J.-E., Liske, J.
"A laboratory study of the in-situ sulphation of alkali chloride-rich deposits – A corrosion perspective"
Manuscript

Statement of contribution

Paper I: I performed all of the experimental and analytical work. Jan Froitzheim and Nicklas Folkeson assisted me during the FIB milling. I authored the paper with support from my supervisors.

Paper II: I performed all of the experimental and analytical work and authored the paper with support from my supervisors.

Paper III: I performed most of the IC, XRD and SEM/EDX analysis and authored the most of the paper (expect the parts concerning the boiler which was authored by Lars-Erik Åmand) with support from Lars-Erik Åmand and my supervisors.

Paper IV: I performed all of the experimental and analytical work except the AES analysis which was performed by Josefin Hall. I authored the paper with support from my supervisors.

Paper V: I performed the exposures on 304L in the SO_2-enviroment, XRD analysis, plan-view SEM/EDX analysis and assisted in the interpretation of the results.

Paper VI: I participated in the planning of the exposures and assisted in the interpretation of the results.

Paper VII: I performed all of the experimental and analytical work and authored the paper with support from my supervisors.

Related work

The following papers and reports have also been published, but are not included in this thesis.

Herstad Svärd, S., Steenari, B.-M., Åmand, L.-E., Bowalli, J., Öhlin, J., Pettersson, J., Karlsson, S., Larsson, E., Svensson, J.-E., Johansson, L.-G., Davidsson, K., Bäfver, L., Almark, M.
"Measures for simultaneous minimization of alkali related operating problems, Phase 3"
Värmeforsk report, Report number: A08-817, (2010).

Pettersson, J., Svensson, J.-E., Skog, E., Johansson, L.-G., Folkeson, N., Froitzheim, J., Karlsson, S., Larsson, E., Israelsson, N., Enestam, S., Tuiremo, J., Jonasson, A., Arnesson, B., Andersson B.-Å., Heikne, B.
"KME-411 Evaluation of different fuel additives ability to master corrosion and deposition on steam superheaters in a waste fired CFB-boiler"
KME report, Project KME-411 (2010).

Karlsson, S., Pettersson, J., Åmand, L.-E.
"Reducing high temperature corrosion when burning waste by adding digested sewage sludge"
Proceedings of *The Swedish-Finnish Flame Days*, International Flame Research Foundation, January 26–27, (2011), Piteå, Sweden

Karlsson, S., Jonsson, T., Engkvist, J., Svensson, J.-E., Liske, J.
"The effect of SO2 (g) on the initial stages of KCl induced high temperature corrosion of 304L at 600° C"
8th International Symposium on High-Temperature Corrosion and Protection of Materials, LezEmbiez, 2012, France

Paz, M. D., Jonsson, J., Liske, J., Karlsson, S., Davis, C., Jonasson, A,. Sandberg, T.
"KME 608 Study of corrosion memory in boiler heat surfaces by field tests with biomass fuel mixes including sulphur and refuse fractions"
KME Report, Project KME-608 (2015)

Preface

This thesis summarizes research carried out within the Swedish Competence Centre for High Temperature Corrosion (HTC), from 2009 to 2015. The work was performed at Environmental Inorganic Chemistry at the Department of Chemistry and Chemical Engineering, Chalmers University of Technology, Göteborg, Sweden, under the supervision of Professor Jan-Erik Svensson. The work was founded by the High Temperature Corrosion Centre (HTC), Konsortiet för Materialteknik för termiska energiprocesser (KME), Värmefors (VF) ant the Swedish Energy Agency (SEA).

List of acronyms

AES	Auger Electron Spectroscopy
BF	Bright Field
BIB	Broad Ion Beam
BSE	Backscattered Electron
EDX	Energy Dispersive X-ray
FEG	Field Emission Gun
FIB	Focused Ion Beam
FTIR	Fourier Transform Infrared Spectroscopy
HAADF	High Angle Annular Dark Field
IACM	In-situ Alkali Chloride Monitor
IC	Ion Chromatography
SE	Secondary Electron
SEM	Scanning Electron Microscope
SRF	Solid Recovered Fuel
STEM	Scanning Transmission Electron Microscope
TEM	Transmission Electron Microscope
XRD	X-ray Diffraction

Table of Contents

1. Introduction

During the last 50 years the global temperature has increased dramatically (Figure 1). As a result, glaciers and polar ices are melting, the sea level is rising and extreme weather is becoming more common. Global warming may also result in the extinction of species that are unable to adapt to these new climate conditions. Some claim that global warming is merely a natural fluctuation. However, there is strong evidence that most of the global warming observed is due to increased levels of so-called "greenhouse gases" in the atmosphere caused by human activity [1].
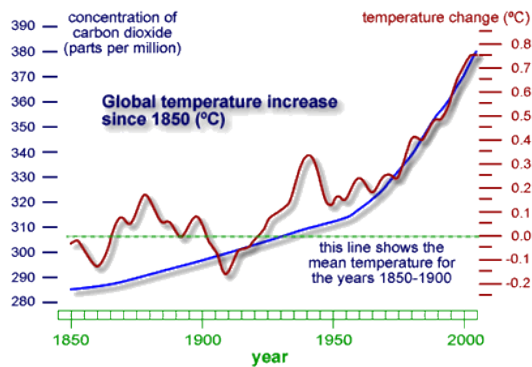
Figure 1: Changes in global temperature [2] and the fate of a polar bear due to global warming [3]

Carbon dioxide (CO_2), one of the greenhouse gases making the largest contribution from human activities, is released into the atmosphere by the combustion of fossil fuels. Furthermore, the extraction of fossil fuels leads to further environmental disasters, such as major oil spills. Ironically, as the polar ice melts, the opportunities to exploit the large gas and oil deposits in the Arctic increase [4]. Besides the great environmental impact, fossil fuels are also non-renewable. They are limited in supply and will one day be depleted. Thus, the use of fossil fuels must be reduced significantly and be replaced by sustainable and environmentally friendly energy sources.

An alternative to fossil fuels are renewable fuels such as biomass and certain types of waste residues. In contrast to fossil fuels, these fuels do not increase the CO_2 content in the atmosphere being combusted. Instead, they release what would otherwise be released naturally as the organic matter they are made of decomposes. Hence, the use of biomass and waste is an important issue for the future. However, these fuels usually contain large

amounts of alkali chlorides which result in a highly corrosive flue gas [5-11]. Hence, the deposits formed on e.g. the superheater tubes are often rich in alkali chlorides which have been shown to greatly increase the corrosion rate of stainless steels [12-23]. High-temperature corrosion leads to fast degradation of the material and constitutes a significant problem from an economical point of view. To counteract these corrosion problems, the maximum steam temperature in the boiler is kept lower than in fossil fuel power plants. This reduces the corrosion rate but also decreases the electrical efficiency. Hence, in order to reach acceptable corrosion rates with high efficiency in the production of power in waste and biomass-fired boilers, corrosion mitigating techniques are needed. One way to decrease the corrosion rate is to change the corrosive atmosphere in the boiler, e.g. by using fuel additives. For instance, the corrosion rate can be reduced by adding sulphur to the fuel in order to sulphate the alkali chlorides to less corrosive alkali sulphates [6, 11, 24-38]. However, the sulphation reaction releases the corrosive gas hydrogen chloride (HCl) and high concentrations of sulphur are often connected to increased corrosion rate due to sulphide formation [39]. Furthermore, the presence of metal sulphides decreases the scale adhesion which may induce spallation of the oxide layer [40].

1.1. Aim of this work

The aim of this work is to obtain greater understanding of the corrosivity of alkali chlorides and the impact of addition of sulphur to the fuel on the corrosion rate. The study includes field exposure in order to investigate the effect of different fuel compositions. It also includes well-controlled laboratory exposures, designed to simulate a simplified version of the environment in a boiler and to study the corrosion mechanism in detail. The study mainly focuses on investigating the initial corrosive effect of potassium chloride (KCl) on the austenitic stainless steel 304L (Fe18Cr10Ni) at 600°C and the corrosion-inhibiting effect of sulphur. This is done by adding sulphur dioxide (SO_2) to the gas flow (in the laboratory exposures) and by means of co-combustion of digested sewage sludge (in the field exposures). This work also investigates how the corrosion attack is affected by the corrosion history, i.e. previous deposit build-up and oxide scale formation. Special attention to the reaction kinetics pervades the entire work.

2. Oxidation of metals

2.1. Thermodynamics

Most metals are thermodynamically unstable and therefore react spontaneously with the surrounding environment forming various oxides depending on the specific atmosphere [39]. The chemical reaction of a metal M and oxygen gas (O_2) to form the oxide M_xO_y may be written as:

$$xM(s) + \frac{y}{2} O_2(g) \rightleftarrows M_xO_y(s) \tag{2.1}$$

where the driving force for the reaction is given by the change in Gibb's free energy, ΔG (see reaction 2.2). A reaction is spontaneous if the change in free-energy is negative ($\Delta G<0$). If however the value is positive ($\Delta G>0$), the reverse reaction is favoured and no change in free energy ($\Delta G=0$) implies equilibrium.

$$\Delta G = \Sigma\Delta G(\text{products}) - \Sigma\Delta G(\text{reactants}) \tag{2.2}$$

The oxide stability at constant temperature can be estimated by using the relation between ΔG and the activities of the species involved. For reaction (2.1) ΔG is expressed as:

$$\Delta G = \Delta G^o + RT \ln K_{eq} = \Delta G^o + RT \ln \frac{a(MxOy)(s)}{a^x_{M(s)} a_{O_{2(g)}}^{y/2}} \tag{2.3}$$

where ΔG^o is the standard Gibb's free energy, R is the gas constant, K_{eq} is the equilibrium constant for the reaction and a is the activities for the products and reactants. For pure solids, the activity is equal to 1 and the activity of a gas can be assumed to be equal to its partial pressure, p. At equilibrium ($\Delta G = 0$), equation (2.4) can be arranged as:

$$p_{O_2} = e^{\frac{\Delta G^{o2}/y}{RT}} \tag{2.4}$$

where p_{O_2} is the dissociation pressure of the oxide, which can be interpreted as the lowest pressure of the oxygen needed for the oxide to be stable at a given temperature.

A convenient way to summarize the affinity of metals for oxygen is by means of an Ellingham diagram (Figure 2) in which the standard free energy of the formation of an oxide is plotted against temperature. An Ellingham diagram does not predict the oxidation rates, only whether a reaction is thermodynamically possible or not.
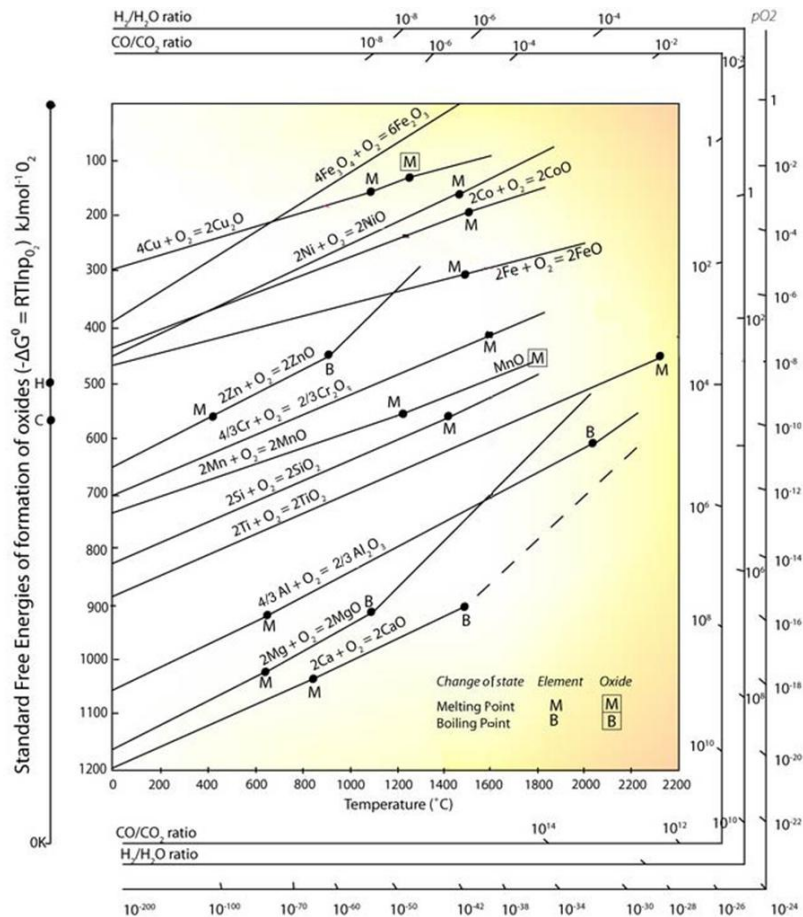
Figure 2: Ellingham diagram for some metals and their metal oxide [41]

2.2. The initial oxidation process and oxide growth

The initial oxidation process can be divided into three steps which are illustrated in Figure 3. In the first step (a), oxygen is absorbed and then dissociated on a clean metal surface, followed by a charge transfer and the formation of O^{2-}. In the second step (b), individual oxide nuclei form and grow laterally on the surface to form a continuous oxide film. In the third step (c), the surface oxide separates the metal from the gas and the reaction can only proceed by solid state diffusion of one or both reactants (oxygen and metal ions) through the oxide. These initial oxidation stages are very rapid, even at room temperature.

a O₂(g)

$O_2(g)+4e^- \rightarrow 2O^{2-}(ads)$

Metal

b O₂(g)

Metal

c O₂(g)

O^{2-} e^- Me^{n+}

Metal

Figure 3: The initial formation of an oxide scale by adsorption of oxygen, oxide nucleation and growth to form a continuous oxide scale (stages a–c)
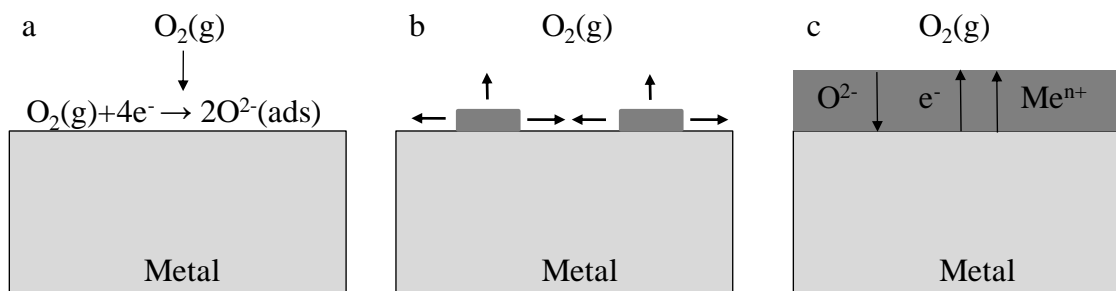
When a continuous oxide layer covers the surface, the process generally stops as the diffusion at room temperature is too slow. However, with increasing temperature, diffusion rates increase rapidly [39]. The diffusion rate at a given temperature varies between different materials.

2.2.1. Oxide growth by lattice diffusion

The transport of reactants through a solid oxide (lattice diffusion) can take place in several different ways [39], e.g. by diffusion through vacancies and interstitial ions. For ions to be transported across the oxide defects must be present. In a perfect crystalline solid, all the lattice positions are occupied by the respective atoms, cations or ions. However, perfect solids only exist at absolute zero temperature, above which defects are present [40]. These defects can be divided into two groups: stoichiometric defects, where the number of cations is balanced by the number of anions, and non-stoichiometric defects, which are a consequence of a change in composition [42].

In stoichiometric crystals, which have a low concentration of defects, the most common defect types found are Frenkel and Schottky defects. Frenkel defects can be described as pair of ion vacancies and interstitial ions of the same type that maintain charge neutrality. In Schottky defects, the number of cation vacancies and anion vacancies is identical which maintains charge electro-neutrality [39]. Both types of defects increase the ion mobility but provide no mechanism by which electrons may be transferred. Thus they are of limited relevance to the oxidation process where electron transport is involved [43].

Most of the oxides are, however, non-stoichiometric and has a higher concentration of defects. Non-stoichiometric compounds can be classified as semiconductors with either p-

5

type or n-type behaviour [43]. Positive semiconductors (p-type) are oxides with metal excess (e.g. $M_{1+x}O$) where interstitial ions predominate in the defective structure. Metal excess can also be achieved by removing oxygen ions (e.g. MO_{1-x}) whereby oxygen vacancies in the lattice are produced. In both cases, the defects have positive charge and are compensated for by an excess of electrons. Positive semiconductors (n-type) are a metal deficit, either by removal of metal ions (e.g. $M_{1-x}O$) or by addition of oxygen, (e.g. MO_{1+x}). The defects have negative charge, which is compensated for through the formation of positive electron holes [39].

The presence of varying types of defects gives rise to different forms of lattice diffusion. Three important mechanisms are illustrated in Figure 4: the vacancy diffusion mechanism, the interstitial diffusion mechanism and the interstitialcy diffusion mechanism. In vacancy diffusion, an ion moves from its regular lattice site to an adjacent unoccupied lattice. Thus a new vacancy is found at its previous site. In this mode of diffusion, the ions move in the opposite direction to the vacancies. Interstitial diffusion takes place when an ion in interstitial position moves into an adjacent internal site. This mechanism is probable only when the interstitial ion or atom is smaller than the atoms on the normal lattice positions [39]. Interstitialcy mechanisms take place when the interstitial ion moves to a regular lattice site, forcing the ion at the regular site into another interstitial position. This happens when the distortion during the movement becomes too large to make the interstitial mechanism probable.
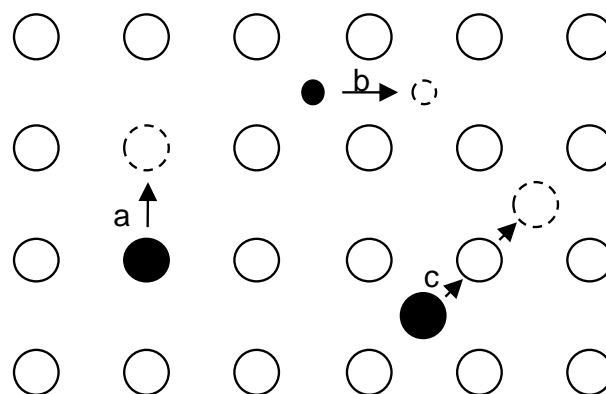

Figure 4: Illustrations of a) vacancy diffusion, b) interstitial diffusion and c) interstitialcy diffusion [40]

6

2.2.2. Oxide growth by short-circuit diffusion

Diffusion can also occur through non-lattice defects. Since most materials and alloys are polycrystalline they consist of a large number of single crystal or grains where the crystal orientation differs from one grain to the next. The intersections between grains are called grain boundaries and have a much higher defect density than the grains. Diffusion through grain boundaries is called short-circuit diffusion and also includes diffusion through dislocations and diffusivity at the surface. In metals, diffusion coefficients in grains boundaries have been shown to be considerably higher than those of lattice diffusion. [39]. Although the situation in oxide is more complex, with both anions and cations being able to diffuse and in opposite directions, grain boundary diffusion has been shown to be significantly faster than lattice diffusion in many oxides. The diffusivity in polycrystalline materials can generally be ordered according to [44]:

$$D < D_d \leq D_{gb} < D_s \tag{2.5}$$

where D is lattice diffusivity, D_d is the dislocation diffusivity, D_{gb} is the grain-boundary diffusivity and D_s is the diffusivity at the surface. Although grain-boundary diffusion is faster than lattice diffusion, the volume in which the diffusion takes place is often very small compared to the volume in which lattice diffusion occurs. Therefore lattice diffusion is included in the diffusion mechanism through the oxide scale. Furthermore, as the temperature increases, the coefficient for lattice diffusion increases more than the coefficient for grain-boundary diffusion [39]. A general principle is that the grain-boundary diffusion is the dominant diffusion path at temperatures below 0.6 of the melting temperature of the oxide [45]. At higher temperatures, lattice diffusion is considered to be the dominant one. In the present study, the temperatures were sufficiently low for grain-boundary diffusion to be expected to dominate the transport of ions across the scale.

2.3. Oxidation kinetics

Thermodynamics establishes the possibility of oxide formation under certain conditions of temperature and partial pressure of oxygen. However, thermodynamics does not reveal the rate of oxidation and the reaction kinetics of oxides thus needs to be considered. The kinetics of the oxidation processes are used to classify oxidation behaviours. If we assume a relatively uniform oxide layer, it is possible to represent its growth by kinetics behaviours or laws. The most common ways to visualize these behaviours is by using mass gain curves (see Figure 5) where mass change or oxide scale thickness is plotted against the exposure time. The two most common behaviours observed, and of interest in this work, are linear and parabolic [39, 43], see Figure 5a.

Linear behaviour is commonly observed under conditions where a surface or a phase-boundary process is the rate-determining step and is often observed if the oxide scale is porous and non-protective [43]. In such a case, diffusion through the oxide scale is not the rate-limiting step and the oxidation rate is constant with increasing exposure time. Cracking and spallation of the scale may induce linear behaviour since new metal is continuously exposed to the atmosphere. Linear behaviour can also be observed during the initial stages of the oxidation process before the oxide layer is sufficiently thick to separate the reactants [43].

Parabolic behaviour is most common for metals during high-temperature oxidation. With this type of kinetics the transport of ions or electrons across the oxide scale is the rate-limiting step. Consequently, the oxidation rate decreases as the scale grows thicker. Parabolic kinetics is often connected to Wagner [46] who made a detailed analysis of diffusion processes and established a model for parabolic growth. His model was based on several assumptions such as stoichiometric, compact and adherent oxide scales with only lattice diffusion as rate determining. However, these assumptions are seldom valid. For instance, oxides are generally not stoichiometric and Wagner does not take into account diffusion at grain boundaries.

The oxidation process usually reveals different behaviours at different stages of oxidation, thus often requiring combined rate laws to explain the kinetics. This may occur when an initially protective oxide suddenly fails, a phenomenon known as breakaway oxidation

(see Figure 5b). Reasons for such behaviour are a change in the chemical composition of the oxide and mechanical failure of the scale. This behaviour represented as mass gain curves can be seen in Paper, I, II, IV and V.
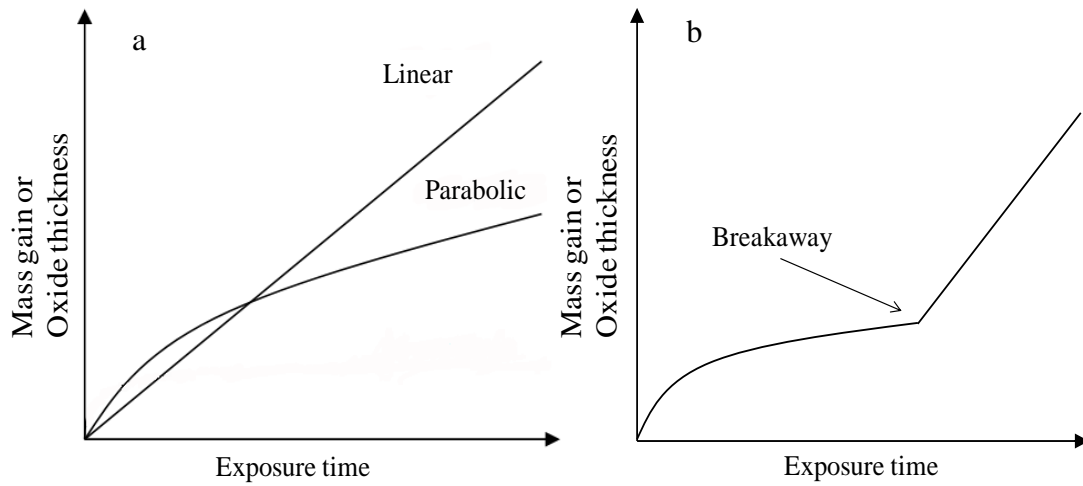

Figure 5: a) Mass gain versus exposure time for linear and parabolic growth and b) typical mass gain curve for high-temperature alloys suffering from breakaway oxidation

3. High-temperature corrosion of stainless steels

3.1. Stainless Steels

Steel is a generic name covering many different alloys. However, in its most basic form, a steel is an interstitial solid solution of carbon (normally between 0.01-1.00 wt.%) in an iron matrix containing carbide precipitations in arrangements that depend on the thermal history of the material. This addition of carbon gives the material increased toughness and strength [47].

By adding chromium to the carbon steel, the corrosion resistance can be greatly improved and with a chromium concentration of at least 11 wt.% [48], a stainless steel is formed. Stainless steels are generally classified by their microstructure and are identified as ferritic, martensitic, austenitic or in duplex form containing grains with different phases. Austenitic steels, which are investigated in this thesis, are the most common types of stainless steel. Although they are typically not particularly strong materials, they pose good ductility. The high chromium content, and to some extent, the addition of nickel, results in an elevated corrosion resistance [48]. The corrosion resistance of stainless steels comes from their ability to form a chromium-rich oxide film that grows slowly and protects the material from further oxidation.

3.1.1. Materials investigated

This thesis involves the austenitic stainless steel 304L (laboratory exposure and field exposure) and the high-alloyed austenitic stainless steel Sanicro 28 (field exposure). The material composition is presented in Table 1. The 304L is a low carbon version of the more common 304 steel. The low carbon content prevents the formation of chromium carbides in the grain boundaries, which can deplete the steel in chromium. Sanicro 28 has high chromium content and is commonly used in highly corrosive environments, e.g. superheater regions of boilers.

Table 1: Chemical composition of alloys 304L and Sanicro 28, concentrations in weight percent and Fe in balance

	Cr	Ni	Mn	Si	Mo	C
304L	18.5	10.2	1.4	0.55	0.49	0.02
Sanicro 28	27.0	31.0	1.77	0.6	3.5	0.02

3.2. Solid oxides important in high-temperature corrosion

The corrosion resistance of a material is highly dependent on the type of oxide formed at high temperatures. In the high-temperature oxidation of alloys, the scale generally consists of several oxide components. Oxides differ in crystal structures, ion diffusivities and also capacity to resist corrosion attacks. The properties of the most important corrosion products are summarized in the follow sections:

Hematite, Fe_2O_3

Hematite exists in two forms: α-Fe_2O_3 and β- Fe_2O_3. However, above 400°C Fe_2O_3 oxidizes to form α-Fe_2O_3 and therefore only this structure is considered here. The α-Fe_2O_3 has the corundum-type structure in which the oxygen ions form a hexagonal close packed lattice with the cations located in two thirds of the octahedral sites. The oxide behaves as an n-type semiconductor in the temperature range 650–800°C and as p-type semiconductor at higher temperatures [39].

Magnetite, Fe_3O_4

Magnetite has the inverse spinel structure and contains both divalent and trivalent irons (Fe^{2+} and Fe^{3+}) [43]. The structure consists of a face-centred cubic array of oxygen anions. Half of the trivalent ions occupy one eighth of the tetrahedral holes, the rest of the ions occupying the octahedral holes. Defects occur on both the sites over iron ions may diffuse. The oxide has a low degree of non-stoichiometry. It behaves, however, as a p-type semiconductor [40].

Wüstite, $Fe_{1-x}O$

Wüstite is stable above 570°C (and reduces oxygen activities) and has the rock salt structure with both the oxygen and iron ion sub-lattice of a cubic close-packed type. The oxide is a p-type of semiconductor with metal vacancies and is highly non-stoichiometric; its composition varying from $Fe_{0.85}O$ to $Fe_{0.95}O$. Due to the high concentrations of defects, the mobility of cations and electrons via metal vacancies and electron holes is extremely high [40].

Eskolaite, Cr$_2$O$_3$

Eskolaite, or chromia, is the only solid chromium oxide which is stable at high temperatures. The structure is the corundum-type and is considered to be a p-type semiconductor [39]. Solid-state diffusion is much slower than that of the iron oxides. Thus, Cr$_2$O$_3$ is one of the best protective oxides at high temperatures and the most protective oxide formed on stainless steels.

Corundum-type solid solution, (Fe,Cr)$_2$O$_3$

Eskolaite, Cr$_2$O$_3$, is completely soluble in Fe$_2$O$_3$ and the oxide formed on stainless steels is usually a solid solution of both, i.e. (Fe$_{1-x}$Cr$_x$)$_2$O$_3$. The protectiveness of this type of oxide depends on its chromium content.

Spinel-type solid solution, (Fe,Cr,Ni)$_3$O$_4$

Oxides based on Fe, Cr and Ni may form solid solutions with a spinel-type structure, e.g. (Fe,Cr,Ni)$_3$O$_4$. Compared to magnetite, some of the Fe(III) ions may be replaced by Cr(III) ions, whereas some of the Fe(II) ions may be replaced by Ni(II) ions. The actual composition depends on the abundance of Fe, Cr and Ni, as well as the oxygen activity in the oxide/metal interface. Spinel-type oxides with other compositions may also form, e.g. (Fe,Cr)$_3$O$_4$ and (Cr,Mn)$_3$O$_4$. I addition, the microstructure of the spinel scale formed on 304L at 600°C in a corrosive environment, has been shown to be more complex forming both fully oxidized regions of spinel oxide and regions of mixed oxide and metal. This is discussed in more detail in paper V.

3.3. The influence of H_2O on the oxidation of 304L

As mentioned, austenitic stainless steels rely on the formation of a chromium-rich oxide for corrosion resistant. When exposing 304L in a dry atmosphere, consisting of 5% O_2 at 600°C, a smooth protective scale forms (Figure 6a). The oxide is a chromium-rich corundum-type oxide which reaches a thickness of about 40nm after 24 hours of exposure (Figure 6b) and less than 200nm after 168 hours of exposure [49-51].
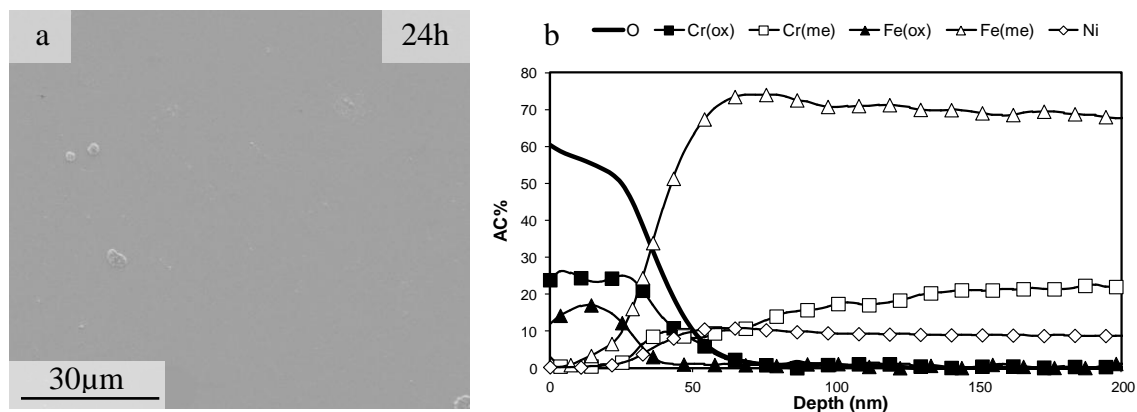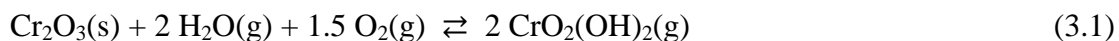

Figure 6: a) SEM images of a 304L sample exposed in 5% O_2 for 24h at 600°C b) AES depth profiling for a 304L sample exposed at 600°C in 5% O_2 for 24h [16]

By introducing water vapour (H_2O) to the atmosphere the protective oxide that forms in dry O_2 is affected by the volatilization of chromic acid $CrO_2(OH)_2$ (reaction 3.1).

$$Cr_2O_3(s) + 2\,H_2O(g) + 1.5\,O_2(g) \rightleftarrows 2\,CrO_2(OH)_2(g) \tag{3.1}$$

Chromium volatilization results in Cr depletion of the protective oxide. Furthermore, if the rate of chromium volatilization is high in comparison to the rate of supply of chromium to the oxide from the alloy, the protective oxide is depleted in chromium. This can cause the oxide to be converted from a chromium-rich slow-growing oxide to an iron-rich rapidly-growing scale. The transition between the two oxidation modes tends to be abrupt and is often termed breakaway oxidation.

Since chromium diffusion in the alloy is dominated by grain-boundary transport at 600°C, the scale that forms in the vicinity of the grain boundaries is able to sustain more chromium volatilization than the scale forming on the centre of the alloy grains, without going into breakaway. This explains the island-like morphology observed in O_2+H_2O environment in the present case, see Figure 7a. The thick scale corresponding to the

14

"islands" consists of an outer hematite (Fe_2O_3) and inner (inward-growing) spinel-type (($FeCrNi)_3O_4$) layer [52], see cross-section of an oxide island in Figure 7b.
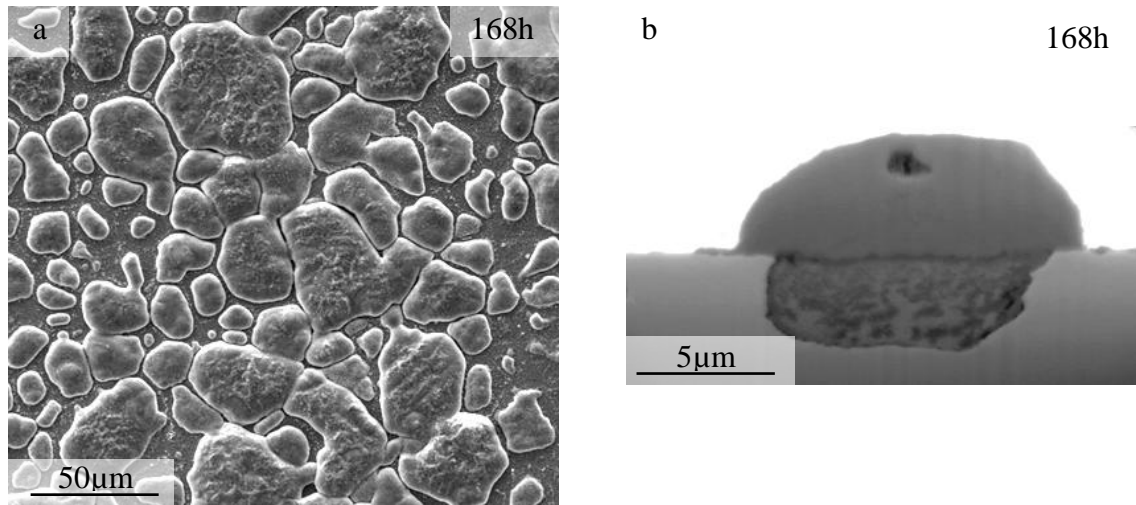

Figure 7: a) SE images of 304L samples exposed in 5% O_2 and 40% H_2O for 168h at 600°C and b) BSE images of FIB cross-sections of an oxide island

3.4. The influence of small amounts of SO_2 on the oxidation of 304L

The reactions of metals/alloys with sulphur are governed by the same principles as for metal oxygen reactions. However, for many metals sulphur is a much more aggressive oxidant than oxygen. One of the reasons for the higher reaction rates in sulphur is that the diffusion in sulphides is generally much faster than that in the corresponding oxides. This is due to higher deviations from stoichiometry in the sulphides and to their higher concentrations of lattice defects which result in a faster outward diffusion of cations through the sulphides for most metals [39]. In addition, the presence of metal sulphides degrades the scale adhesion which induces spallation of the oxide layer [40].

The presence of SO_2 in combustion gases is also known to cause an increased rate of high-temperature corrosion of several metals [39]. However, in some cases the rate of oxidation can actually be suppressed by the presence of SO_2. The addition of small amounts of SO_2 strongly affects the oxidation of iron and FeCr alloys exposed in environments containing oxygen below 600°C. The inhibitive effect of SO_2 is attributed to adsorbed sulphate that forms on the oxide surface (see Figure 8). It is suggested that

15

the absorbed sulphate interferes with the reduction of oxygen molecules by blocking the "active sites" on the surface which slow down the formation of oxygen ions [53].
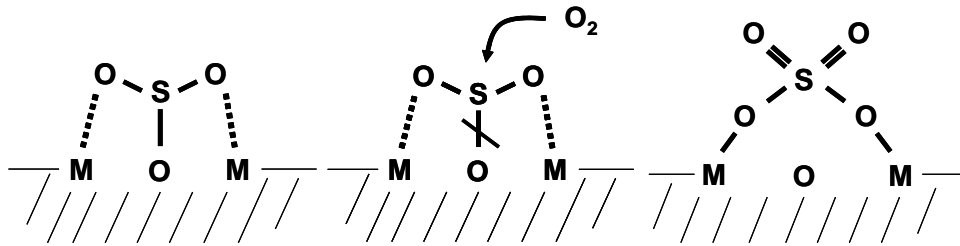

Figure 8: Schematic illustration of the mechanism by which adsorbed SO$_2$ reacts with oxygen to form surface sulphate [54]

The presence of SO$_2$ also inhibits the oxidation of 304L in an environment containing oxygen and water vapour. Again, sulphate is believed to be adsorbed at the scale/gas interface and therefore the rate of oxygen reduction on the oxide surface decreases. In this case, the adsorbed sulphate is also believed to slow down the chromium volatilization that occurs on 304L in a wet environment, resulting in much thinner oxide islands compared to the samples exposed in the absence of water vapour (compare Figure 9 and Figure 7).
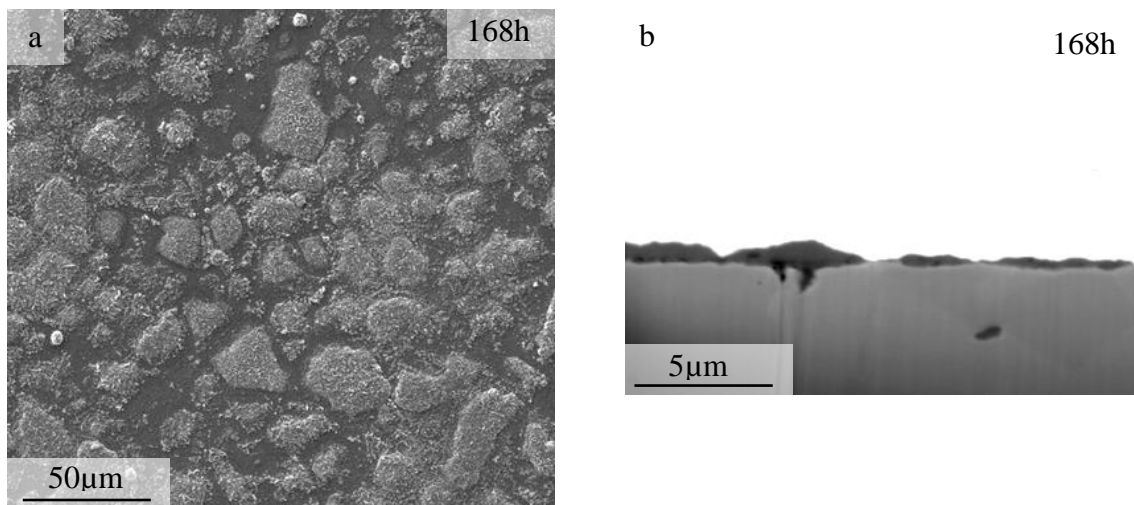

Figure 9: a) SE images of 304L samples exposed in 5% O$_2$, 40% H$_2$O and 300 ppm SO$_2$ for 168h at 600°C and b) BSE images of FIB cross-sections of oxide islands

4. Combustion of biomass and waste for power generation

The worldwide energy supply is based on fossil fuels such as coal, oil and natural gas. However, rising energy prices, unstable markets and the release of CO_2 have led to a growing interest in the use of renewable fuels, e.g. biomass and certain types of waste. Sweden has made a radical change from fossil fuel to renewable fuels and the trend shows that the energy derived from biomass and waste is likely to continue to increase. An example of this rapid change is the Händelö plant (owned by E.ON Värme AB) in Norrköping, Sweden, where the percentage of fossil fuels has decreased from 100% in 1992 to just a few percent in 2014. The change in fuel selection is shown in Figure 10.
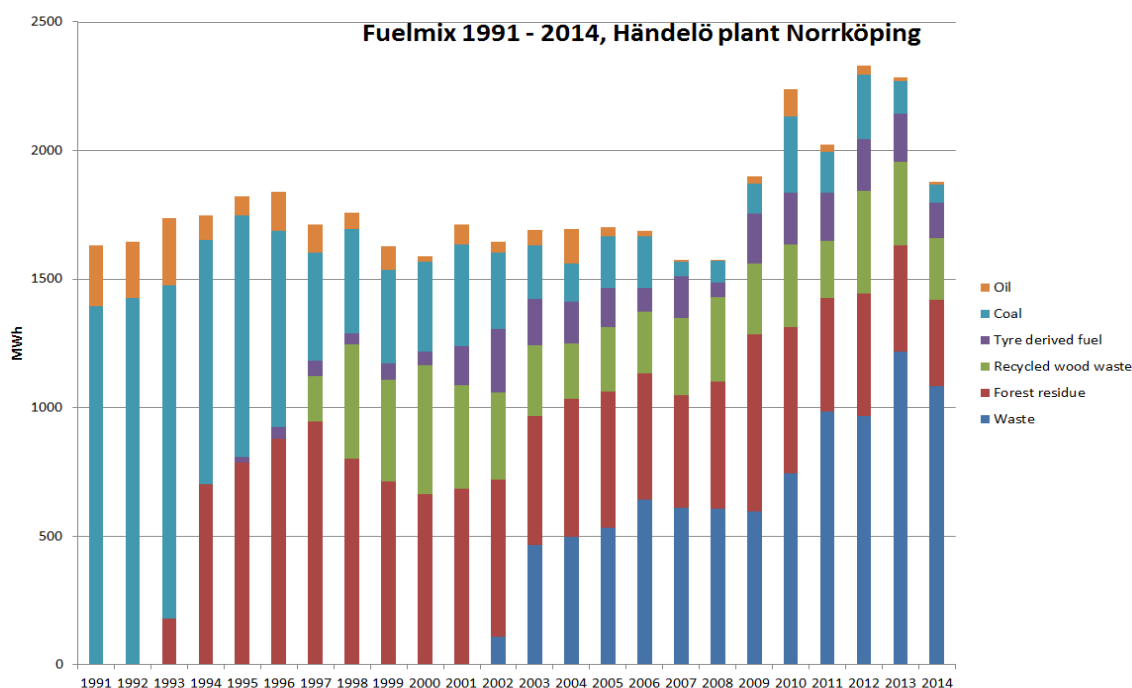

Figure 10: Power generation by fuel type at the Händelö plant (owned by E.ON Värme AB) in Norrköping, Sweden, from 1991 to 2014 [55]

The power production from waste and biomass is done through direct combustion in a boiler. These boilers can vary in size and design but work on the same principle. During combustion a hot flue gas is produced which is used for heating water and subsequently steam by means of various heat exchangers, e.g. water walls, superheaters and economizers. The superheated steam enters the steam turbine, producing electric power. In addition, hot water from the plant is used for district heating.

The two most common types of boilers for biomass and waste combustion are Grate Firing (GT) boilers and Fluidised Bed (FB) boilers. Both types have good fuel flexibility and can be fuelled entirely by biomass or co-fired with coal [56].

In grate-firing systems, the fuel is combusted on a grate area. The fuel is added continuously on top of the grate and then moves down by e.g. vibrations. Air is injected from under the grate in order to supply the combustion process with oxygen but also to cool the metal grates. The advantages with this technique are that it is fairly simple and does not require much fuel preparations [57].

In fluidised bed boilers, the fuel is burned within a hot bed of inert particles, usually sand. The fuel-particle mix is suspended by an upward flow of combustion air within the bed. As velocities increase the gas/solid mix exhibits fluid-like properties which provide more effective heat transfer. Fluidised bed boilers are more efficient than grate-fired boilers. By contrast they usually require the fuel to be processed before combustion since the fuel particles need to be fairly small in order to enable fluidization [57].

Fluidised bed combustion is usually divided into two sub-groups: bubbling fluidised bed (BFB) and circulation fluidised bed (CFB). A BFB operation range is between the minimum fluidisation velocity and the entrainment velocity on which the bed particles remain in the bed. In CFB boilers, the fluidizing velocity is higher than in a BFB which results in both solid fuel and bed material being carried away from the bed. Therefore CFB configurations include solid separators that remove particles that have entrained from the flue gas steam and recycle them to the lower furnaces. In this process, the particles enter a separator, normally a cyclone, which collects the particles and returns them to the bed. The addition of the solid separators allows the CFB technology to reach greater efficiency compared to a BFB [57].

This thesis includes field exposures in three CFB boilers which are described in section 5.1.

4.1. Superheater corrosion

Biomass and waste fuels are numerous, e.g. forestry crops and residues, agricultural crops and residues, industrial waste and municipal solid waste and sewage sludge. The flue gas produced when burning biomass and waste is often very complex and results in a highly corrosive gas compared to the flue gas produced when burning coal and oil (see Table 2). For instance, the amount of alkali is much higher in waste and biofuels. In addition, these fuels are usually high in chlorine and low in sulphur which promotes the formation of the corrosive species HCl(g), sodium chloride (NaCl(g)) and KCl(g). This results in higher corrosion rates in biomass and waste-fired boilers.

Table 2: Approximate flue gas composition in coal, biomass and waste-fired boilers [58, 59]

Fuel	$O_2\%$	$H_2O\%$	SO_2 ppm	HCl ppm	KCl+NaCl ppm
Coal	~4-5	~4-16	~400-1200	~10-50	-
Biomass	~5-10	~10-20	~0-70	~25-1000	~5-50
Waste	~5-11	~10-20	~0-150	~250-1300	<120

Since the heat exchanger tubes in a boiler are cooler than the surrounding atmosphere, condensation of gaseous species in Table 2 occurs on the tube surfaces. The composition of the deposit (that builds up continuously) depends on the fuel composition, but common components are sulphates, carbonates and alkali chlorides. It also contains fly ashes and other particles that are commonly distributed in the flue gas. The metal parts are thus exposed to a very complex chemical environment since all the phases and compounds, i.e. the steel tube, the corrosion product layer formed on the steel tube, the deposit and the flue gas may interact with each other (see Figure 11).

Flue gas O_2, H_2O, CO_2, SO_2, HCl, KCl, NO_x and particles

KCl, NaCl, K_2SO_4, K_2CO_3, $CaSO_4$ SiO_2

Deposit

Fe_2O_3, $(Fe,Cr)_2O_3$, K_2CrO_4, $FeCl_2$

Oxide/corrosion products

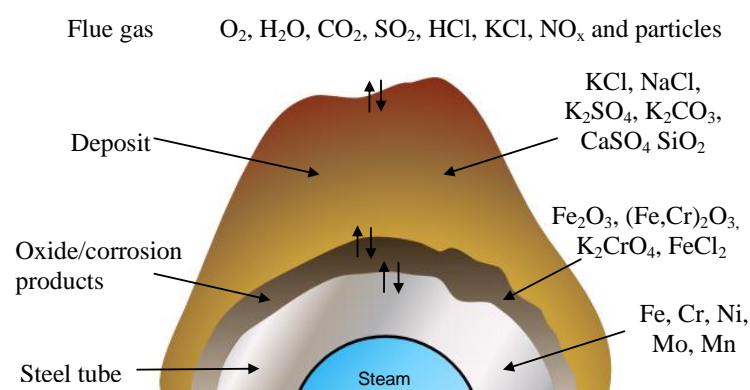Fe, Cr, Ni, Mo, Mn

Steel tube

Steam

Figure 11: Schematic illustration of the complex environment close to the superheater in a biomass or waste-fired boiler

At higher temperatures, stainless steels are often used as a superheater material. As described in section 3.1, the ability of these steels to withstand high temperatures depends on the formation of a protective, chromium-rich oxide. Hence, processes that lead to a breakdown of the protective oxide are critical for the performance of the superheater.

4.1.1. Gaseous corrosion attack

Chlorine-containing compounds are generally considered to be the most corrosive components of the fireside environment. A mechanism commonly used to explain the corrosive effect of these compounds is active oxidation, also known as the chlorine cycle [12]. Here chlorine (Cl_2) is either present initially or forms from HCl by means of the Decon process (reaction 4.1) and is believed to be transported through the oxide scale.

$$2\ HCl(g) + {}^1\!/_2\ O_2(g) \rightarrow Cl_2(g) + H_2O(g) \tag{4.1}$$

When the chlorine reaches the metal surface, the oxygen partial pressure is sufficiently low to thermodynamically favour the formation of transition metal chlorides (see reaction 4.2). The transition metal chlorides are volatile at high temperatures and are therefore believed to diffuse outwardly through the scale as gas molecules (reaction 4.3).

$$Me(s) + {}^x\!/_2\ Cl_2(g) \rightarrow MeCl_x(s) \tag{4.2}$$

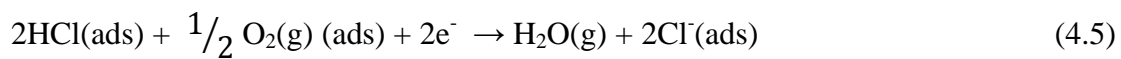$$MeCl_x(s) \rightarrow MeCl_x(g) \tag{4.3}$$

As the gaseous transition metal chlorides diffuse through the oxide scale, the oxygen partial pressure increases, resulting in decomposition due to their thermodynamic instability compared to their corresponding oxides. This results in a porous metal oxide and chloride (Cl_2) is released according to reaction 4.4.

$$yMeCl_x(g) + {}^z\!/_2\ O_2(g) \rightarrow Me_yO_z(s) + {}^{xy}\!/_2\ Cl_2(g) \tag{4.4}$$
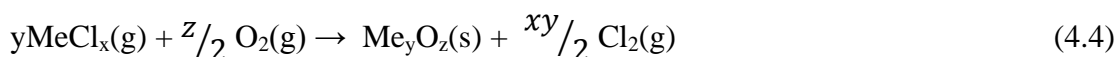
It is then suggested that the $Cl_2(g)$ released penetrates the oxide and reacts once more with the metal, completing the cycle.

Another explanation for chlorine-induced corrosion is proposed by Folkeson et al [60]. Here it is proposed that the chlorination of the alloy is preceded by an electrochemical mechanism whereby the formation of chlorine ions on the scale surface is coupled to metal oxidation at the scale/metal interface by electronic current and by the grain-boundary migration of chloride ions and cations.
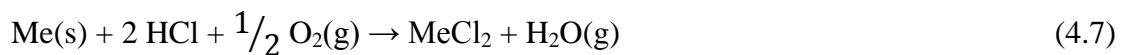
The formation of chlorine ions is expected at the oxide surface by means dissociation of adsorbed HCl molecules. Simultaneously, absorbed oxygen is reduced by the corroded metal beneath. This enables the reaction with the oxide ions and the released proton to form water vapour, metal ions and adsorbed chlorine ions according to reaction 4.5 and 4.6, which results in the sum reaction 4.7.

$$2HCl(ads) + \tfrac{1}{2} O_2(g)\ (ads) + 2e^- \rightarrow H_2O(g) + 2Cl^-(ads) \tag{4.5}$$
(at scale/gas interface)

$$Me(s) \rightarrow Me^{n+} + ne^- \tag{4.6}$$
(at scale/metal interface)

$$Me(s) + 2\ HCl + \tfrac{1}{2} O_2(g) \rightarrow MeCl_2 + H_2O(g) \tag{4.7}$$

4.1.2. Deposit-induced corrosion

Deposits rich in alkali chlorides are also connected to high corrosion rates. One explanation for this is the active oxidation mechanism described previously. Chlorine is then released through a reaction between the alkali chloride and the metal oxide scale, see reaction 4.8.

$$\tfrac{1}{2} Cr_2O_3(s) + 2\ KCl(s) + H_2O(g) + \tfrac{3}{4} O_2(g) \rightarrow K_2CrO_4(s) + 2HCl(g) \tag{4.8}$$
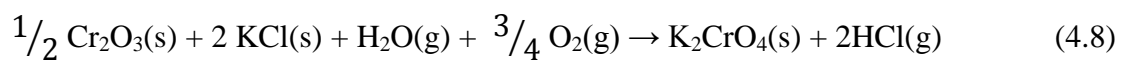
In contrast to the theory underlying the chlorine-induced corrosion mechanism, it has been shown that the potassium ion plays an important role in the initiation of KCl-induced corrosion of stainless steels [13-16, 61, 62]. Thus, potassium carbonate (K_2CO_3) is as corrosive as KCl towards stainless steel 304L at 600°C [63]. The corrosivity of the potassium ion was attributed to the formation of potassium chromate (K_2CrO_4) by

reaction with the oxide scale, see reaction 4.8 and 4.9. Analogous to the reaction with water vapour (section 3.3, reaction 3.1), these reactions deplete the oxide in chromium, leaving it iron-rich and less protective.

$$\tfrac{1}{2}\,Cr_2O_3(s) + K_2CO_3(s) + \tfrac{3}{4}\,O_2(g) \rightarrow K_2CrO_4(s) + CO_2(g) \qquad (4.9)$$
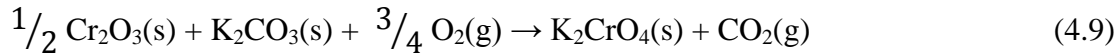
Another type of oxide degradation is corrosion attack due to the presence of molten species. Referred to as hot corrosion, it is divided into type I and type II [39]. Hot corrosion type I usually occurs at higher temperatures when the salt deposit on the alloy is in a liquid state. Hot corrosion type II takes place at lower temperatures in the presence of solid or gaseous salts, i.e. temperatures lower than the melting point of the salt. Two or more salts may then form a eutectic mixture with a melting point far below that of the constituent pure compounds. The oxide or the metal, or both, may also be dissolved in the molten phase. The increased corrosion rate in the presence of a melt is suggested to be due to the faster transport of ions through the liquid compared to diffusion through a solid [39]. For most compounds, the melting points are above the superheater temperature. However, in combination with other salts and/or corrosion products a low-melting eutectic may form. The melting temperature of some compounds often found in biomass and waste is listed in Table 3. This list also includes the melting point for some eutectic mixes.

Table 3: Melting point for some pure compounds and mixtures [19, 64, 65]

Pure compounds (Deposit)	m.P (C°)	Pure compounds (Corrosion products)	m.P (C°)	Eutectic	m.P (C°)
KCl	771	$FeCl_2$	677	KCl-NaCl	657
NaCl	801	$CrCl_2$	820	$KCl-FeCl_2$	355
$CaCl_2$	782	$NiCl_2$	1030	$KCl-NaCl-FeCl_2$	380
$ZnCl_2$	318	K_2CrO_4	973	$KCl-K_2CrO_4$	650
$PbCl_2$	498	K_2CrO_7	398	$KCl-K_2CrO_7$	367
K_2SO_4	1069	Na_2CrO_4	792	$KCl-ZnCl_2$	230
Na_2SO_4	880	Na_2CrO_7	357	$ZnCl_2-PbCl_2$	300
$CaSO_4$	1460	$CaCrO_4$	1020	$K_2SO_4-NaSO_4-CaSO_4$	776
K_2CO_3	901			$K_2SO_4-Na_2SO_4-Fe2O_3$	575
Na_2CO_3	851				
$CaCO_3$	825				

4.2. Sulphur additives

The fuel chosen has a great impact on the total budget of a boiler; less expensive fuels decrease the operation costs. However, cheaper fuels are also usually more corrosive and the decrease in direct operation costs is counteracted by an increase in maintenance costs due to corrosion. To deal with the corrosion problems, the maximum steam temperature in the boiler is kept lower than in fossil fuel power plants.

A decreased temperature reduces the corrosion rate, but also decreases the electrical efficiency. Hence, in order to reach acceptable corrosion rates with maintained or higher efficiency in the production of power in waste and biomass-fired boilers, corrosion mitigating techniques are needed. One possibility is to use materials with higher corrosion resistance. Another possibility is to make the corrosive environment less corrosive, e.g. by using fuel additives or by co-combustion. In biomass and waste-fired boilers the use of additives or the co-combustion has mainly focused on increasing the availability of sulphur (in the form of SO_2 and/or sulphur trioxide (SO_3)) in the boiler. This includes sulphur-based additives such as elemental sulphur and ammonium sulphate ((NH_4)SO_4), sulphur recirculation or by co-combustion of waste and biomass with coal, peat and municipal sewage sludge [6, 11, 24-38]. The main aim of these methods is to sulphate alkali chlorides into their corresponding less corrosive alkali sulphates. The non-corrosive nature of potassium sulphate (K_2SO_4) at this temperature is explained by its reluctance to react with the protective, chromium-rich oxide to form K_2CrO_4 [63]. Thus, the corrosion properties of the stainless steel remain intact. However, the sulphation reaction simultaneously releases the corrosive gas HCl. In addition, high concentrations of sulphur are often connected to increased corrosion rate and decreased oxide scale adhesion due to sulphide formation [39, 40].

5. Experimental and analytical techniques

The aim of this work is to create greater understanding of the corrosive effect of alkali chlorides and how the addition of sulphur in the fuel can affect the corrosion rate. The study includes field exposure to investigate the effect of different fuel compositions. It also includes well-controlled laboratory exposure, designed to simulate a simplified version of the environment in a boiler in order to provide detailed information about the corrosion mechanisms. All samples have been analysed by detailed and advanced analytical methods.

5.1. Field exposures

Three CFB boilers were used in the field studies: a boiler located at Chalmers University of Technology with a thermal capacity of 12 MW (Figure 12), a biomass-fired boiler in Händelö with a thermal capacity of 131 MW (Figure 13) and a waste-fired boiler in Händelö with a thermal capacity of 75 MW (Figure 14).
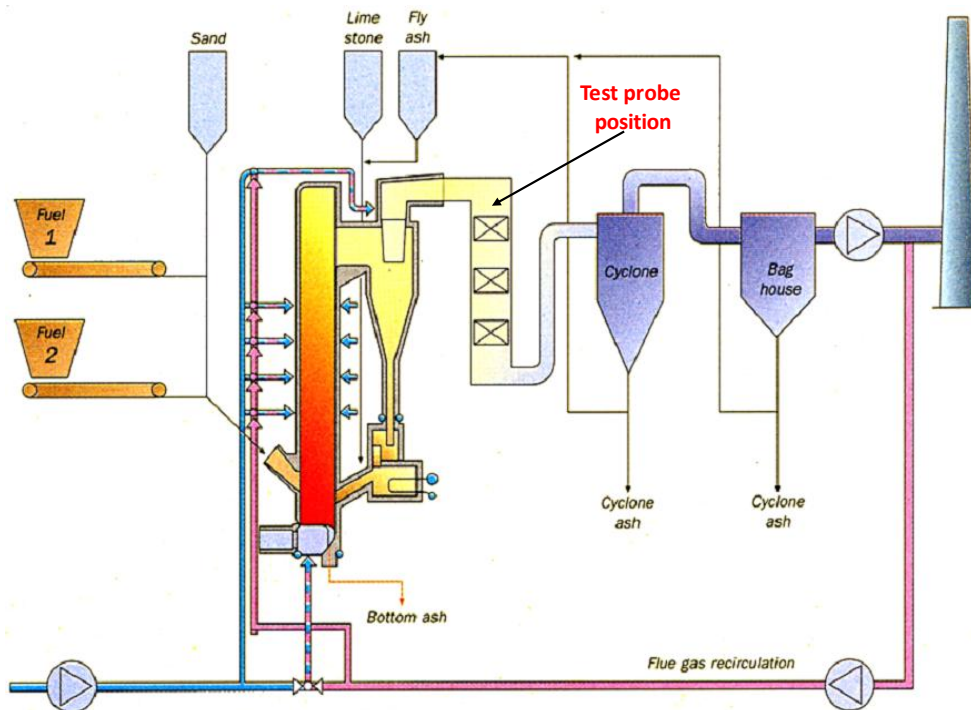

Figure 12: Schematic image of the 12 MW boiler located at Chalmers University of Technology
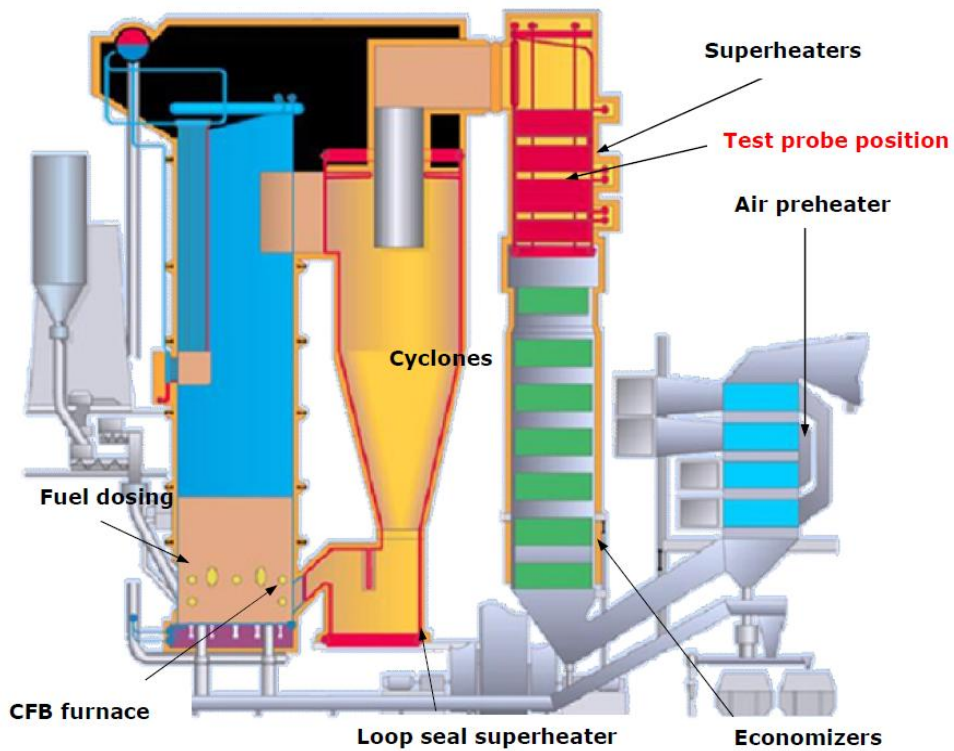
Figure 13: Schematic image of the 131 MW boiler located at Händelö, Norrköping, owned by E.ON Värme AB [67]
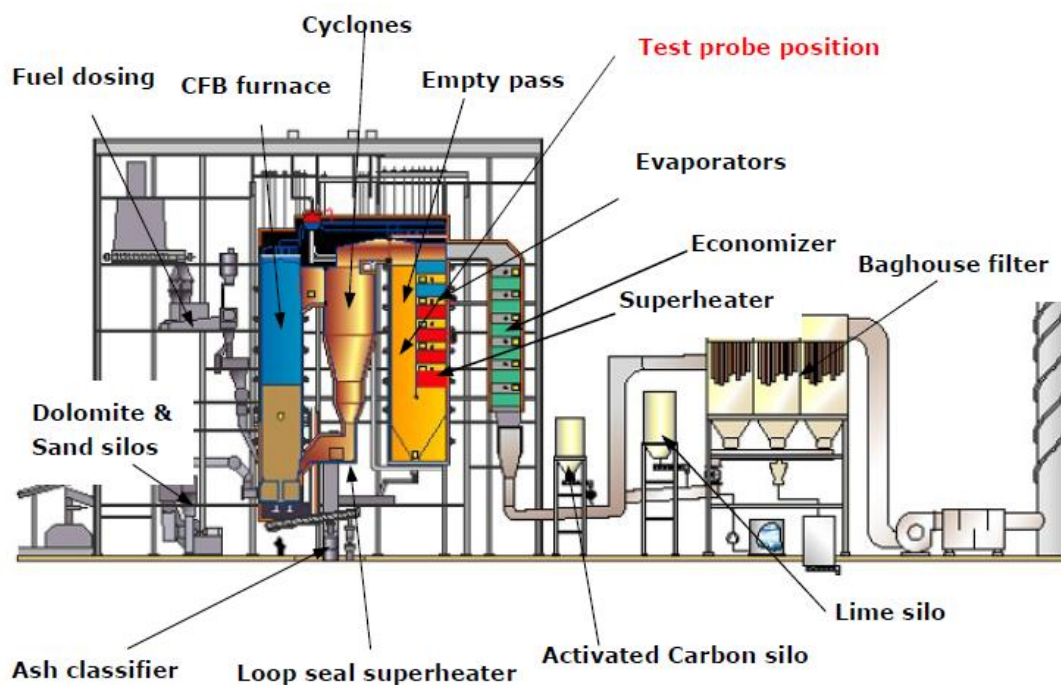

Figure 14: Schematic image of the 75 MW boiler located at Händelö, Norrköping, owned by E.ON Värme AB[67]

Three combustion cases were investigated in the Chalmers boiler. The first case was *SRF* in which bark pellets were co-fired with waste (Solid Recovered Fuel (SRF)). Here the share of waste was 22% based on the total amount of dry fuel supplied to the boiler. The second case was *MSS1-low* with additional combustion to the case *SRF* of municipal sewage sludge from a waste water treatment plant with a mixture of 7.3% (calculated on dry weight). Finally the third case was *MSS2-high* with additional combustion to the case *SRF* of municipal sewage sludge from a waste water treatment plant with a mixture of 13% (calculated on dry weight). The element compositions of the separate fuels are given in Table 4. A complete table of the composition can be found in paper III.

Table 4: Fuel properties

	SRF	*MSS1-low*	*MSS2-high*
Moisture, %	5.2	78	73
Ultimate analysis (% on dry fuel)			
C	53.6	53.0	54.4
O	37.3	29.5	29.0
S	0.24	3.0	2.4
Cl	0.62	0.18	0.10
Ash elements g/ kg dry ash			
K	11	12	11
Na	22	7.1	5
Al	48	50	48
Si	138	124	105
Ca	192	93	59
P	5.1	74	78

The flue gas composition was obtained by conventional instrumentation, Fourier Transform Infrared Spectroscopy (FTIR) instrument, Bomen MB100 and an in-situ alkali chloride monitor (IACM). By using a gas extraction probe at the same position as the IACM, it was possible to control the chlorine in the gas phase in the form of HCl. The exposures were made using an air-cooled probe equipped with deposit rings (Figure 15).

The probe was maintained at constant temperatures of 600, 650 and 700°C during a period of 24h of exposure with a gas temperature at 746-775°C. This thesis includes results from the deposit rings exposed at 600°C only.
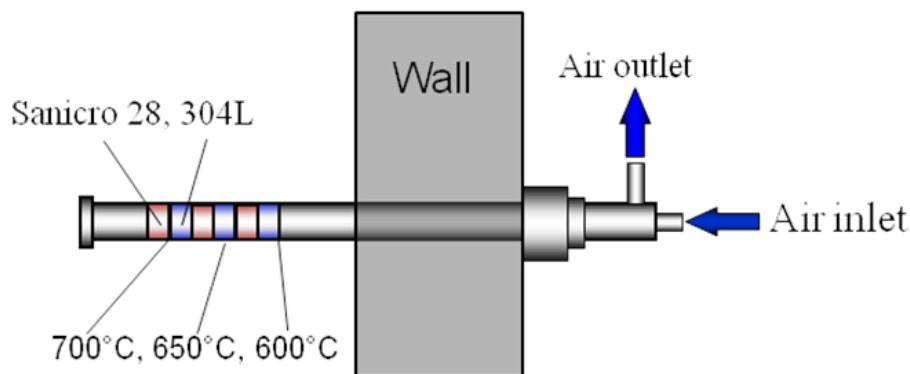

Figure 15: Schematic image of the air-cooled corrosion probe equipped with sample rings at surface temperatures of 600, 650 and 700°C

The materials used in this study were the austenitic stainless steels 304L and Sanicro 28. For chemical compositions see Table 1, section 3.1.1. All sample rings had an outer diameter of 38mm and a width of 15mm. Prior to exposure the samples were cleaned in acetone and ethanol using ultrasonic agitation and then dried with air and stored in plastic bottles. Two rings, 304L and Sanicro 28, were used in all exposure cases lasting for 24 hours. The temperature was kept at 600 °C (material temperature) and the samples were stored in a desiccator prior to and after exposure.

After exposure the samples were analysed by means of three analytical methods: Scanning Electron Microscope (SEM) together with energy dispersive X-ray (EDX), X-ray diffraction (XRD) and Ion Chromatography (IC). The 304L sample rings were mounted in epoxy. Afterwards they were cut and polished. The cross-section, which included deposit, oxide layer and metal, was then analysed by means of SEM/EDX. For the Sanicro 28 sample rings, the deposit was mechanically removed and crystalline compounds were analysed with XRD. After the XRD analysis, the deposit was leached in Milli-Q water for quantification of chlorine ions and sulphate (SO_4^{2-}) ions.

The biomass-fired boiler in Händelö has a mildly corrosive environment due to fuel mix containing the sulphur-rich tyre-derived fuel. In the waste-fired boiler in Händelö, a fuel mix of household and industrial waste was used making the environment in the flue gas very corrosive with high amounts of chlorides and alkali. Figure 16 shows the distribution of fuel mix in both boilers.
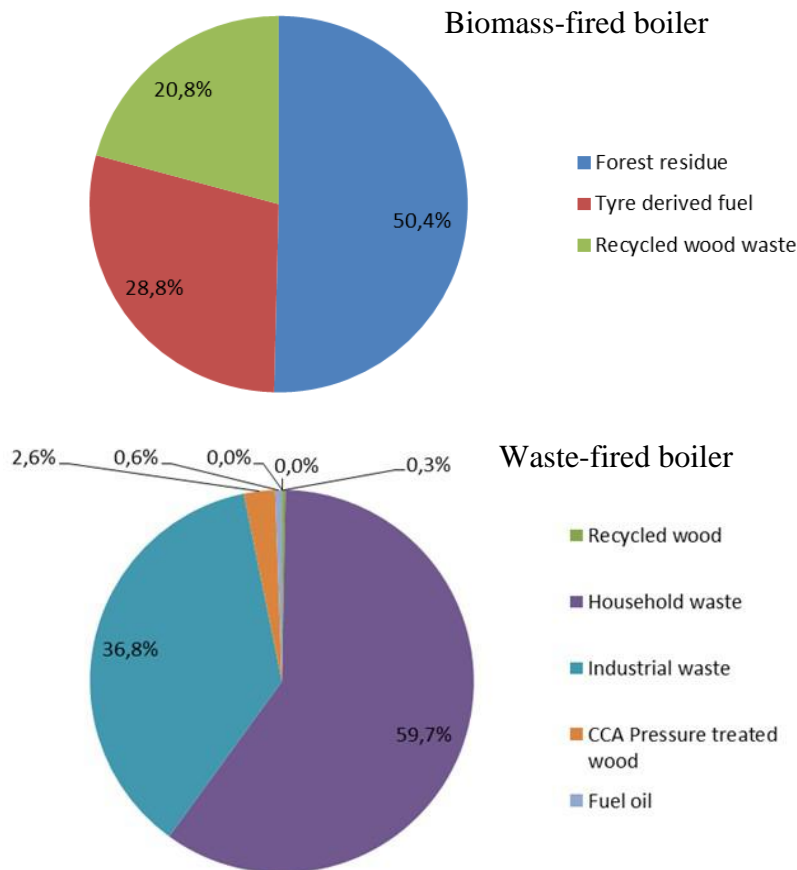

Figure 16: Distribution of fuel mix in the biomass-fired boiler and the waste-fired boiler in Händelö [67]

The exposures were performed by air-cooled probes. The sample rings had an outer diameter of 48mm and a wall thickness of 2.7mm. Prior to exposure the samples were first cleaned in acetone and ethanol using ultrasonic agitation and then dried with air and stored in plastic bottles. Each probe had three different temperature zones with three samples within each zone. This work focuses on the 304L samples exposed at 600 °C (see composition in Table 1) and the samples were investigated by means of SEM/EDX.

5.2. Laboratory exposures

The laboratory study explores the effect of small amounts of three chloride salts and large amounts of KCl on the high-temperature corrosion of 304L. The study also includes an investigation into the effects of adding SO_2 to the gas flow.

The material investigated was the austenitic stainless steel, 304L, the chemical composition of which is given in Table 1. The geometrical area of the samples was 5.56 cm^2, ($15 \times 15 \times 2mm$). For handling, a hole ($\varphi = 1.5mm$) was drilled, centred along one side of each sample. Before exposure the samples were ground with 320 grit SiC and deionized water. The samples were then polished with 9 μm, 3 μm and 1μm diamond solution and lubricating liquid on a polishing cloth until a mirror-like surface was obtained. After polishing, the samples were degreased and cleaned in acetone and ethanol using an ultrasonic bath. The samples were coated with the preferred chloride salt (NaCl, KCl or calcium chloride ($CaCl_2$)) to a cation equivalent of 1.35μmol/cm^2 (small amounts) or 13.5μmol/cm^2 (large amounts). The salts were applied by spraying the samples with a saturated solution of the preferred salt in water/ethanol. Figure 17 shows BSE images of unexposed samples sprayed with a) 1.35μmol/cm^2 KCl and b) 1.35μmol/cm^2 KCl. The mass change of the samples was measured prior to and after exposure using a six decimal Sartorius ^{TM} balance.

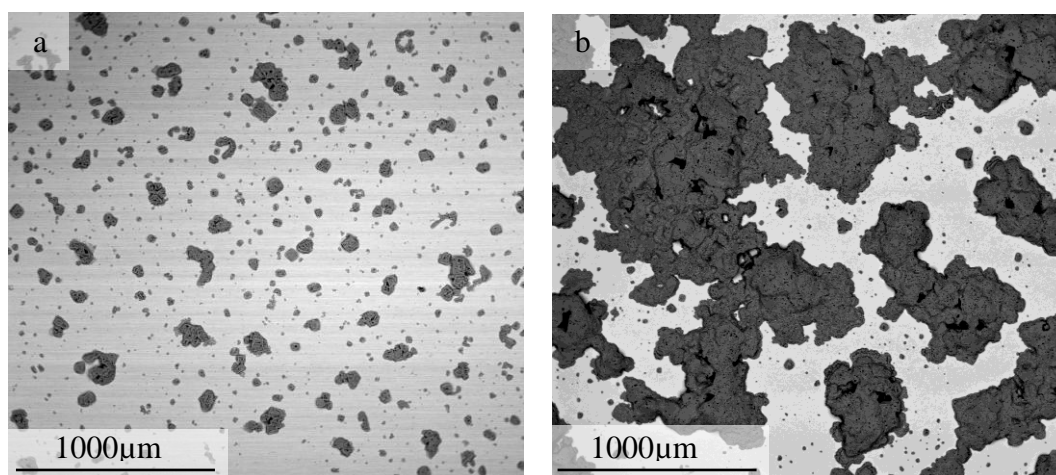**Figure 17: BSE images of unexposed samples sprayed with a) 1.35μmol/cm^2 KCl and b) 13.5μmol/cm^2 KCl**

Laboratory exposures were carried out in furnaces with horizontal silica tube with an inner diameter of 35.5mm. Two set-ups were used for the gas inlet, see Figure 18. Exposures in the absence of SO_2 were made in set-up (a) whereas exposures in the presence of SO_2 were performed in set-up (b). The atmosphere consisted of nitrogen gas (N_2) with 5% O_2 in all exposures. The flow rate was 1000 mL/min and was controlled by a Bios DC2 Flow Calibrator. The dry gas was led through a humidifier and a temperature-controlled condenser to obtain the correct water concentration (40%). In the SO_2 exposures, 300 ppm SO_2 was added directly to the furnace. The flow of SO_2 was controlled by a digital mass flow regulator. All exposures were isothermal and the temperature was kept at 600°C ($\pm$ 1°C). The samples were mounted three at a time using an alumina sample holder and positioned parallel to the gas flow direction. Samples were weighed before and after exposure and all gravimetric measurements were made on a six decimal Sartorius ^{TM} balance. The exposure times ranged from 15 minutes to 168 hours. After exposure, the samples were stored in desiccators over phosphorus pentoxide (P_2O_5).
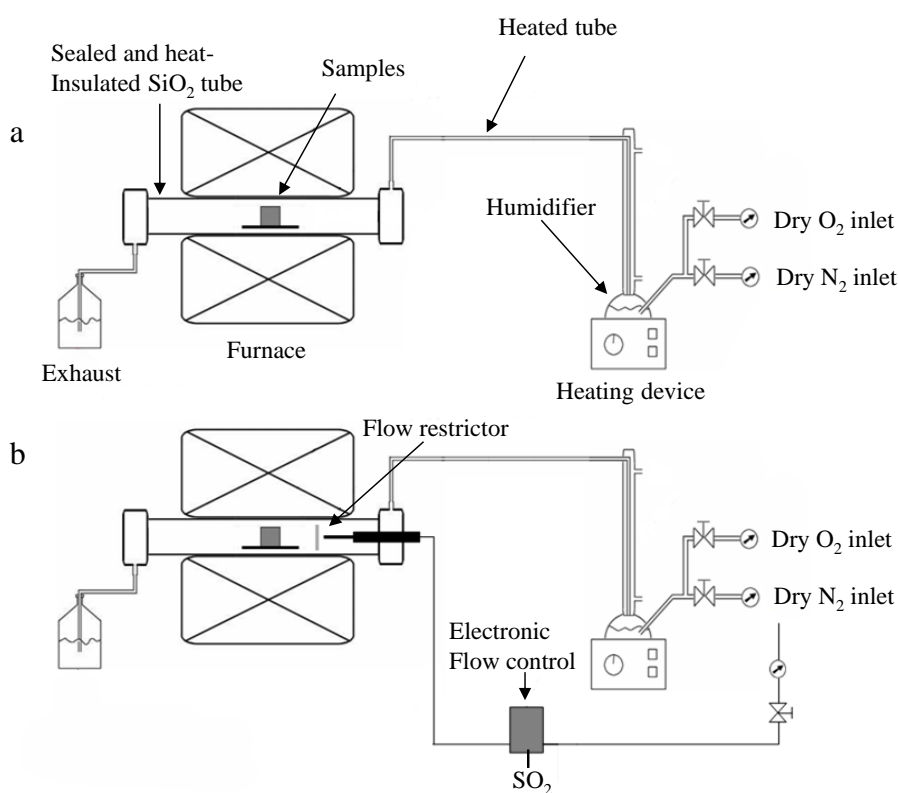

Figure 18: Horizontal tube furnace set-ups with gas inlet system for: a) dry and wet reference exposure and exposure in the presence of salt and b) dry and wet reference SO_2 exposure and SO_2 exposure in the presence of salt

5.3. Analytical techniques

Numerous analytical techniques can be used to evaluate the exposed samples. All techniques have their advantages and drawbacks. To get a comprehensive view of the corrosion attack, it is important to use complementary techniques. This section presents the different analytical techniques used in this work.

5.3.1. X-Ray Diffraction (XRD)

Crystalline phases and corrosion products formed on the sample were analysed by means of X-Ray Diffraction (XRD). The theory underlying the technique is that crystals are built up of planes each of which act as a mirror. When an X-ray beam strikes a sample, some of the X-rays are reflected by the first plane at an angle of reflection equal to the angle of incidence. Some of the light penetrates the first plane and is reflected by the second plane (see Figure 19). Another part is then reflected by the third plan and so on.
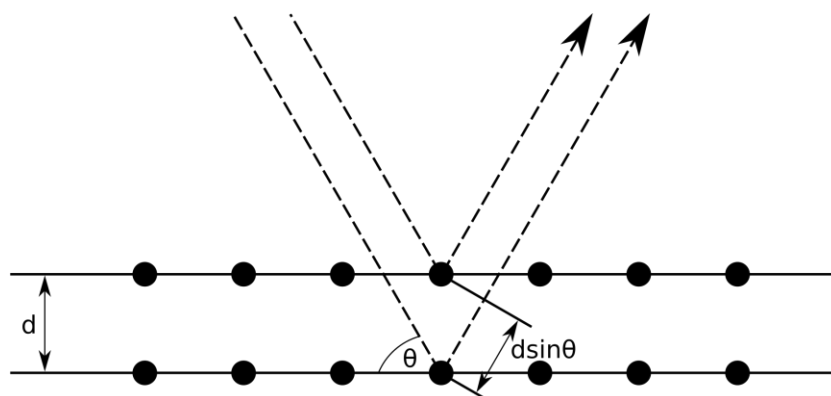

Figure 19: Illustration of diffraction by a series of crystal planes according to Bragg's law [68]

The light reflected from the different planes interferes and cancels each other out unless the difference in distance between the plane *n* and the plane n + 1 is exactly a multiple of the wavelength. This is called Bragg's Law by William Henry Bragg, see reaction 5.1.

$$n\lambda = 2d \sin \theta \tag{5.1}$$

where d is the distance between the planes in the crystal lattice, θ is the incidence/diffracted angle, n is an integer number, and λ the wavelength of the X-rays.

Each crystalline phase gives rise to a unique pattern of reflection at a specific angle. The data can be presented in a diagram with intensity as a function of the angle, 2θ. Identification is made by comparing the x-ray diffraction pattern obtained with a database. The intensity of the diffraction pattern is related to the concentration.

The most common set-up for the analysis of bulk materials is Bragg-Brentano geometry in which the source and the detector move symmetrically around the sample. In this work, grazing incidence X-ray diffraction (GIXRD) technique was used. This set-up facilitates the analysis of thin layers, e.g. oxide scales, since it has a narrow angle of incidence for incoming X-rays. This narrow angle limits the penetration depth of the X-rays in the oxide scale and bulk material and allows the characterization of the usually thin oxide scales. Since the detector moves with the X-ray source at a fixed angle, the penetration depth of the X-ray can be changed from a few nm up to the µm range, see Figure 20.
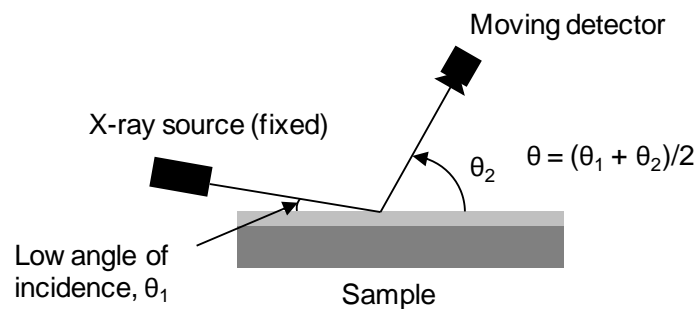

Figure 20: Set-up for grazing incidence X-ray diffraction [69]

The instrument used in this study was a Siemens D5000 power diffractometer (Cu K_α radiation) equipped with a Göbel mirror and a grazing incidence attachment. Here, CuK$_\alpha$ radiation was used and the angle of incidence was 1°–5°. The detector measured between $20° < 2\theta < 70°$.

5.3.2. Ion Chromatography (IC)

The amount of water soluble ions in the corrosion product layer was determined by ion chromatography. In chromatographic separations, the sample ions are transported in a mobile phase. This phase is then forced through an immiscible stationary phase, which is fixed in a column. These ions, strongly retained by the stationary phases, move very slowly with the flow of the mobile phase, while the ions that are weakly held by the stationary phase move more rapidly. As a consequence of these varying degrees of mobility, the ions become separated into discrete "zones" (see Figure 21a). Small ions such as chloride elute first from the column, while larger divalent ions such as sulphates and chromates (CrO_4^{2-}) elute later. By placing a detector at the end of the column, the signals from the separated anions can be measured and plotted as a function of time (see Figure 21b). A high concentration of a certain ion results in a high peak. The concentration of ions is then determined by comparing the detected signals with a standard solution of known concentration performance standards.
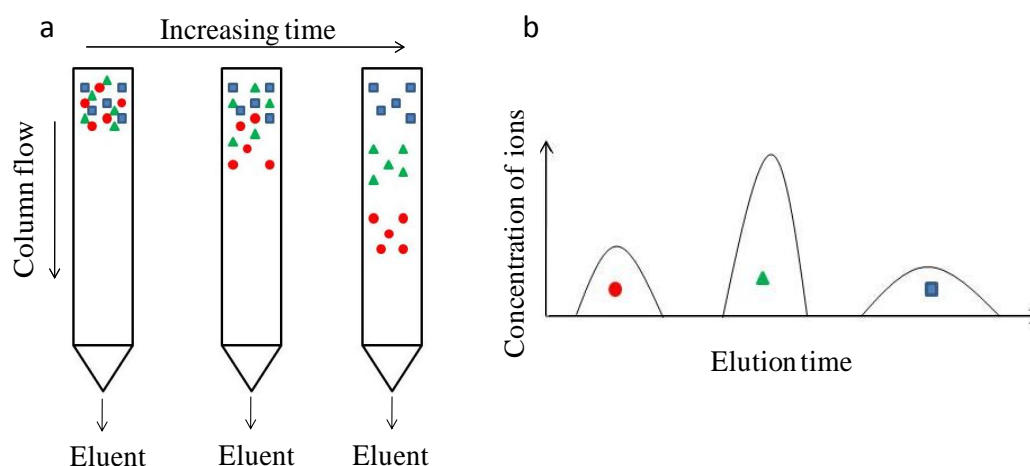

Figure 21: Schematic image of a) the ion separation in the column and b) signal of the detected ions

To quantify the amount of water-soluble anions, a Dionex ICS-90 Ion Chromatography (IC) system was used equipped with an IonPac AS4A-SC analytic column. The eluent was 1.8 mM sodium carbonate/1.7mM sodium bicarbonate. To determine the amount of water-soluble cations, a Dionex ICS-900 IC system equipped an IonPac CS12A analytic column was used. The eluent was 20 mM sulfonic acid. The flow rate was 2mL/min for both anion and cation analyses and the relative standard deviation of the analysis corresponds to about ± 5%

In terms of preparation, the samples were leached in 10mL Milli-Q water using an ultrasonic bath. The leaching procedure was performed twice for each sample and the time was set to 10 minutes. The two leaching solutions were combined into one before analysis with Ion Chromatography. For each single data point, at least three individual IC analyses have been performed. The relative standard deviation of the analysis corresponds to about ± 5%. In Figure 27, Figure 31, Figure 36, Figure 41 and Figure 44 each data point correspond to a single sample and not an average value.

5.3.3. Scanning Electron Microscope (SEM) & Energy Dispersive X-ray (EDX)

The Scanning Electron Microscope (SEM) was used for imaging and chemical analysis of the samples. The combination of high resolution and a large depth of focus enable a detailed study of the rough surface of the samples exposed. By connecting an energy dispersive X-ray (EDX) spectroscopy analysis system to the SEM, both qualitative and quantitative chemical analyses can be carried out.

The microscope operates by scanning a focused electron beam across the surface. When the high energy electrons strike the atoms in the sample, a variety of signals is generated, including secondary electrons, back-scattered electrons, Auger electrons and characteristic X-rays (Figure 22). All these signals are generated in the entire interaction volume but are released from different depths according to their specific energy as illustrated in Figure 23. The size and shape of the interaction volume depends on the atomic number/numbers of the specimen analysed and the acceleration voltage.
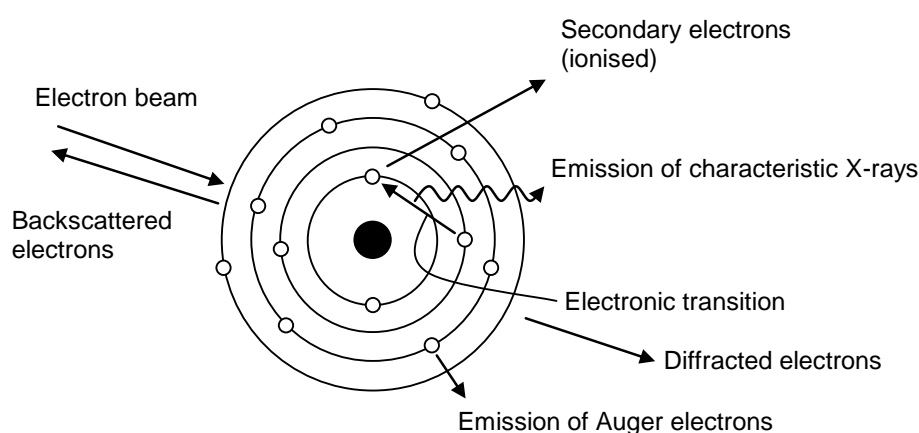

Figure 22: Some of the processes occurring in atoms when struck by high energy electrons [42]
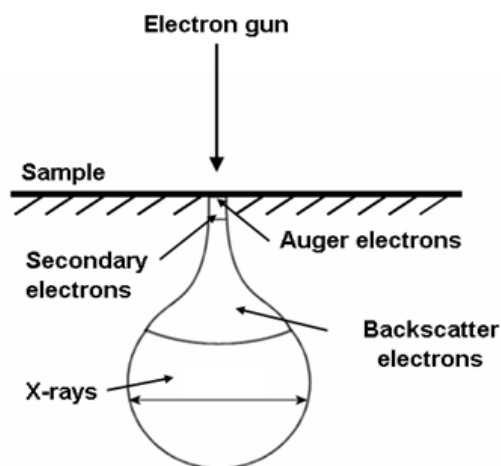
Figure 23: Illustration of the interaction volume in a material, showing the relative depth from which specific signals may escape [69]

In this work secondary electrons (SE) and back-scattered electrons (BSE) are used for imaging and X-rays for chemical analysis. Secondary electrons are generated when incident beam electrons lose energy by inelastic collisions in the sample. Secondary electrons have low energy (<50 eV) and are generated close to the sample surface (<10nm). Therefore, a high resolution image can be obtained and the contrast in the image is determined by the topography of the sample.

Back-scattered electrons are those from the primary electron beam that are scattered by the atomic nuclei in the sample. They have higher energies (>50 eV) than SEs and can therefore escape from a larger volume (0.1–0.5 μm deep), leading to a reduced resolution. The scattering of electrons by the nuclei implies a higher yield from heavier elements. The image therefore shows the distribution of the chemical compositions in the sample, where elements with a high atomic number appear brighter than elements with a lower atomic number [70]. Hence, porous regions and void appears darker in the image. Figure 24 shows SEM images of a sample made by using (a) secondary electrons (SE image) and (b) back-scattered electrons (BSE image).
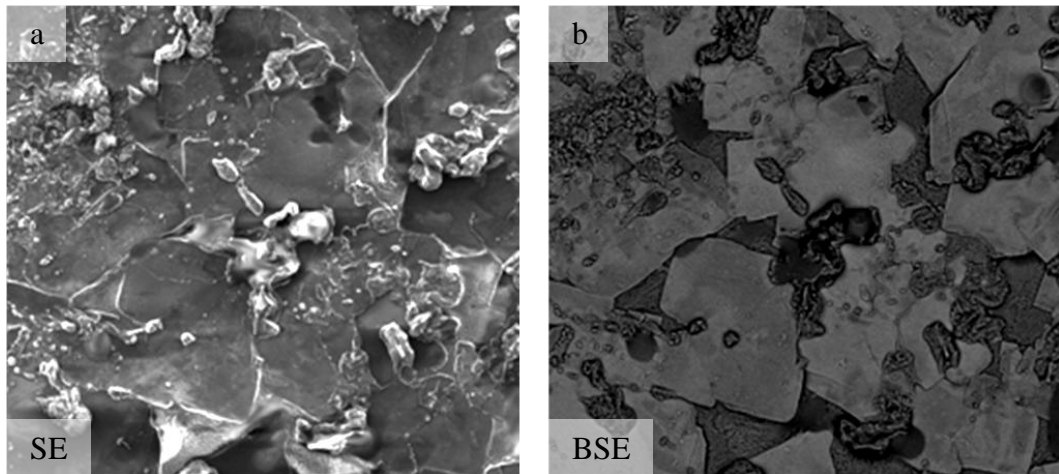
Figure 24: SEM images of a sample with (a) secondary electrons (SE image) and (b) back-scattered electrons (BSE image)

The X-ray-generated signals have an energy characteristic of the parent element and allow identification of the element. When the incident beam causes ionization by knocking out an electron from the sample atom, an empty low energy position is formed. As an outer electron relaxes into this position, X-rays are emitted. In the SEM, X-rays are used for chemical analysis through an energy dispersive X-ray (EDX) detector. This provides rapid qualitative or (by adequate standards) quantitative analysis of elemental composition with a sampling depth of 1–2 microns. These X-rays may also be used to form maps, showing the elemental distribution in a sample surface. Figure 25a is an example of EDX mapping where Figure 25b and Figure 25c show the distribution of sodium and iron on the sample surface shown as a BSE image in Figure 25a.
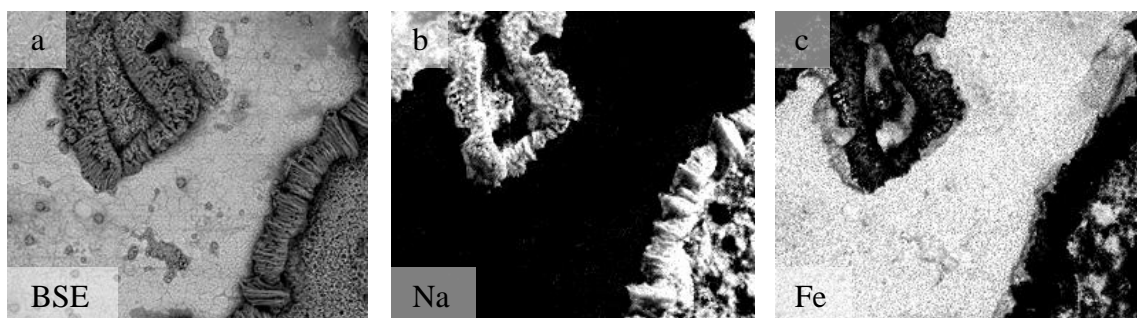

Figure 25: (a) BSE image of a sample surface together with EDX map of (b) sodium and (c) iron

In this work an FEI Quanta 200 SEM equipped with a field emission gun (FEG) was used for analytical scanning electron microscopy. The SEM was operated in a high vacuum at accelerating voltage of 5-20kV and 10mm working distance. Chemical analysis was carried out using an $80mm^2$ X-Max^N Oxford Instruments silicon drift detector (SDD) and Oxford Instruments INCA Energy Dispersive X-ray (EDX) software.

5.3.4. Broad Ion Beam (BIB)

In order to investigate the microstructure of the corrosion scales ion etched cross-sections are prepared. With broad ion beam (BIB) milling, a cross-section in the millimetre range can be produced. In this work a Triple Ion Beam Cutter, Leica TIC 3X Gatan Illion system was used. The instruments were equipped with argon ion guns for sputtering which were operated at 6kV for 6 hours. A protective mask was positioned on the top surface of the samples in order to shield them from ion beam damage as well as producing a smooth cross-section. Furthermore, to enhance the surface finish and to avoid projecting the surface topography onto the final cross-section, a thin silica plate was applied to the top surface of the samples using superglue adhesive. To protect the corrosion products from the glue, the sample was first sputtered with gold. After the glue was cured, samples were dry cut using a low speed diamond saw before being mounted in the BIB instrument. The cross-section was analysed with SEM/EDX.

5.3.5. Focused Ion Beam (FIB)

In order to investigate the microstructure of the corrosion scales in a certain area, cross-sections are prepared by Focused Ion Beam (FIB) milling. The FIB instruments operate similarly to SEM instruments, although using gallium ions instead of electrons. The ions mill away layers of the material from the sample surface. This results in a cross-section, typically 10–40 μm across, of the oxide scale and the underlying metal.

The FIB cross-sections were prepared using an FEI Strata 235 dual beam in a combined FIB/SEM system. The system was equipped with a liquid gallium ion source with a 30 kV accelerating voltage. A strip of platinum was deposited on the sample surface in order to protect it from damage during milling.

5.3.6. Auger Electron Spectroscopy (AES)

The Auger electrons are released near the surface (~4–10 Å), see Figure 23. The kinetic energy of the Auger electrons is specific to the atom from which they were ejected. Hence chemical identification is possible. In Paper IV an instrument equipped with an argon ion gun was used to obtaining depth profiles of selected elements. This was done by quantifying the elements in the surface layers, after which they were sputtered away and the layers beneath were analysed. This process was repeated through the oxide and into the metal substrate.

The AES analyses were performed by Ph.D Josefin Hall, former employee at the Department of Chemistry and Chemical Engineering, Chalmers University of Technology. The instrument used is described in Paper IV.

5.3.6. Transmission Electron Microscopy (TEM)

Transmission Electron Microscopy enables the investigation of microstructure features through high resolution imaging and provides information regarding the sample chemistry and crystallography. Similar to a SEM, an electron beam probes the sample. However, instead of being scattered back by the sample, most of the electrons pass through it. This requires the sample to be very thin, typically 20-200nm, and the accelerating voltage to be high, typically 200-300 kV.

In Paper V, two TEM instruments, operating in Scanning Transmission Electron Microscope (STEM) mode, were used for High Annular Dark Field (HAADF) and Bright Field (BF) imaging. The HAADF mode has the advantage that it can show variation in the atomic number in the sample (Z-contras), i.e. heavier elements appear brighter in the HAADF image and lighter elements obtain a darker contrast. In the BF mode the weakening of the directed beam (by its interaction with the sample) is imaged. In this manner, the sample thickness and diffraction contrast contribute to the image. Thick areas and areas enriched in heavy elements appear with darker contrast. On the contrary, voids appear as white areas since the direct beam passes through the sample without interaction. Chemical analyses were performed by STEM/EDX. The difference from SEM/EDX is that the thin TEM sample gives a lateral resolution of about 5nm compared to 0.5μm in

the SEM (at 10kV) [71]. The crystal structure of the oxides were identified by Convergent Beam Electron Diffraction (CBED)

The TEM analyses were performed by Ph.D. Torbjörn Jonsson and Ph.D. Mohammad Sattari, both at the Department of Chemistry and Chemical Engineering, Chalmers University of Technology. The TEM instruments and sample preparation technique are described in Paper V.

5.3.7. Thermodynamic calculations

The thermodynamic calculations were made by using the software HSC Chemistry 6. In Paper V thermodynamic calculations were performed by Ph.D. Torbjörn Jonsson, using the software THERMO-CALC with the database TCFE7.

6. Results and discussion

6.1. Investigating superheater corrosion in a waste-fired boiler

As described in section 4.2, the corrosive environment in which the superheater tubes are situated is very complex. It is therefore very difficult to trace the sequence of events leading to corrosion by studying a failed superheated tube. To gain more knowledge about the corrosion attack on stainless steel in a corrosive superheater environment, short time exposures (24 hours) of 304L at 600°C (material temperature) were performed in the 12MW$_{th}$ CFB boiler located at Chalmers University of Technology. This was followed by well-controlled laboratory studies in order to evaluate and understand the initial corrosion mechanisms. For more information about the experimental set-ups, see section 5.1.

To achieve a corrosive environment in the boiler bark pellets were co-fired with waste (Solid Recovered Fuel). This combustion case is referred to as *SRF*. The fuel mix in the *SRF* case resulted in a flue gas with high levels of gaseous alkali chlorides (96 ppm), relatively low levels of HCl (12 ppm) and low levels of SO$_2$ (3 ppm).

After 24 hours of exposure the 304L sample was covered by a thick deposit (see cross-section in Figure 26) rich in NaCl and KCl [11]. The corrosive environment resulted in two types of corrosion morphologies: general corrosion, i.e. a thick covering oxide layer, and oxidation along the steel grain boundaries. The oxide layer consists of an outer iron-rich oxide and an inner iron-chromium-nickel-rich oxide [11]. The oxidation along the steel grain boundaries is severe and penetrates deep down into the steel sample, indicating a highly rapid corrosion process.
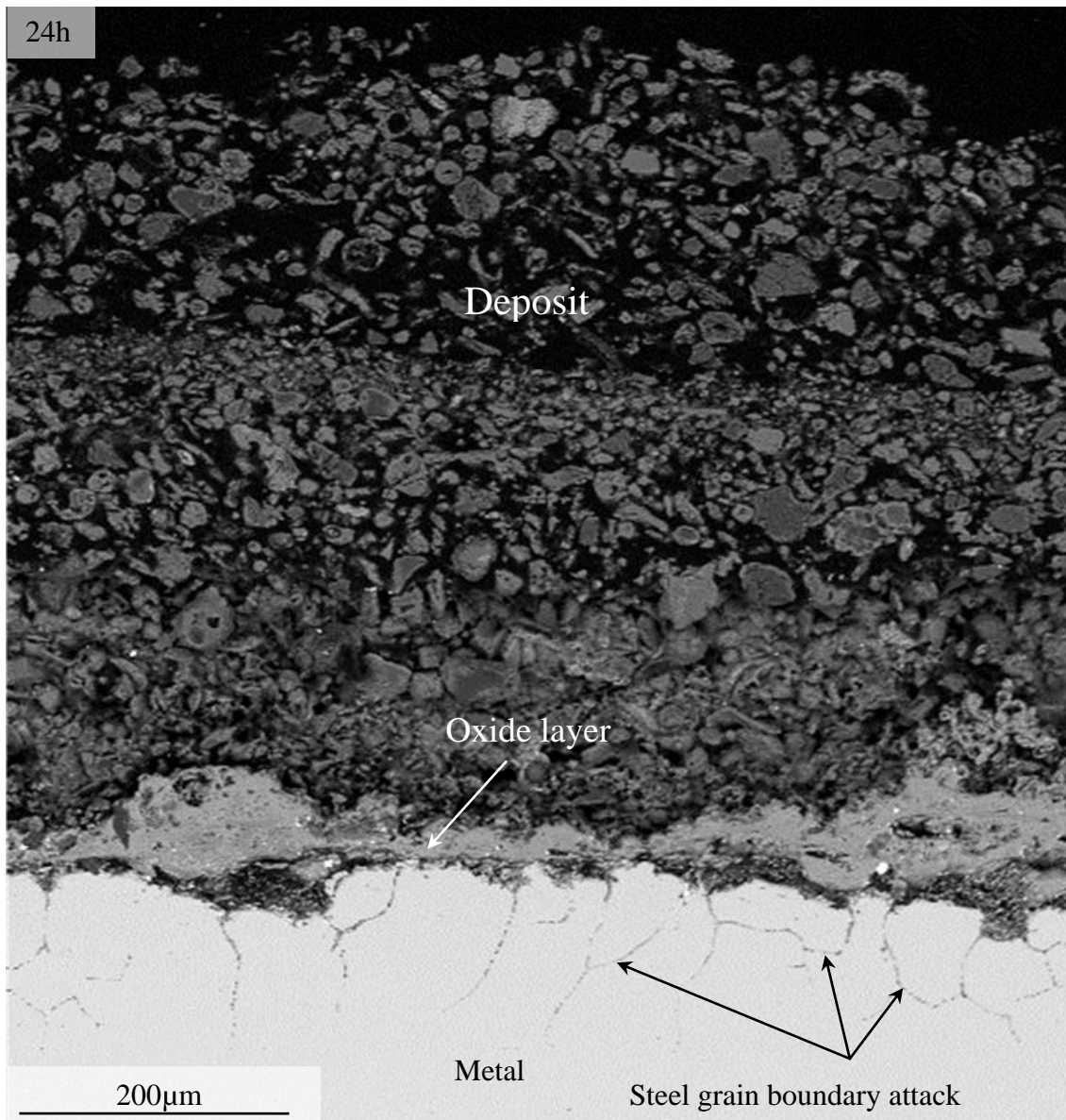
Figure 26: BSE image of a cross-section of the 304L sample exposed in the *SRF* case for 24h at 600°C

The results from the *SRF* case show that burning waste results in a flue gas giving rise to a rather severe corrosion attack after only 24 hours of exposure. The high corrosion rate of superheaters in waste and biomass-fired plants is often linked to the presence of alkali chlorides [12-22]. Previous studies on stainless steel, sprayed with 1.35μmol/cm^2 KCl (referred to as small amounts of KCl), explains that the corrosion attack is initiated by the formation of K_2CrO_4 [16].

Analysis of the corrosion products formed on 304L-samples exposed with small amounts of KCl in a laboratory environment (5% O_2 + 40% H_2O at 600°C) shows that most of the chromate formation occurs during the first hour of exposure (see Figure 27). After 1 hour

of exposure, 18% of the original amount of KCl had formed K_2CrO_4. Over the next 24 hours the amount increases only slightly. Simultaneously to the chromate (CrO_4^{2-}) formation, KCl evaporates as KCl(g). The evaporation rate is fast: after the first hour of exposure, 20% of the applied salt was gone while it is more or less consumed after 24 hours of exposure. Due to the high rate of evaporation and chromate formation during the first hour it is assumed that most of salt was consumed during the first hours of exposure.
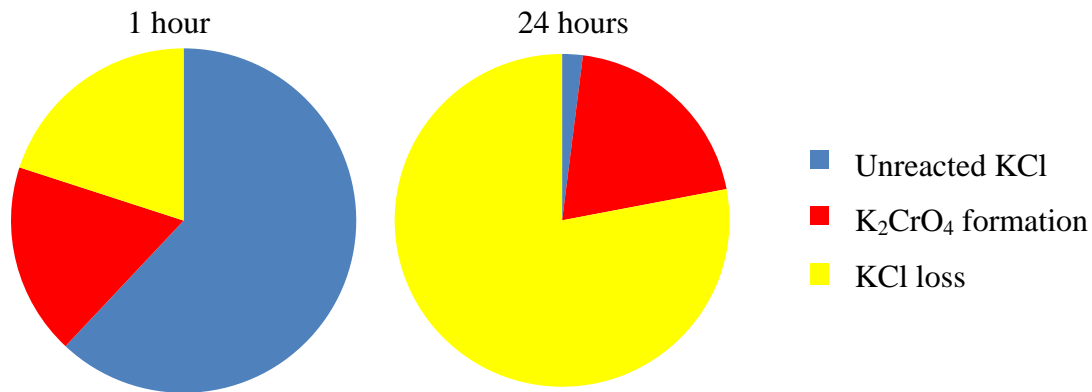

Figure 27: Suggested mass balance based on the IC results, where the amount of water soluble ions detected was measured on samples exposed for 1h and 24h of exposure in 5% O_2 + 40% H_2O + 1.35µmol/cm^2 KCl

The chromate formation occurs over the whole steel sample surface. After 1 hour of exposure K_2CrO_4 particles are clearly visible as scattered dark nodules, especially at the parts of the surface still covered by a thin chromium-rich oxide (see Figure 28a and close-up image in Figure 28c). Therefore, it is proposed that KCl diffuses out from the salt particle, over the surface and then reacts with the chromium-rich oxide according to reaction 6.1. The reaction is also possible with KCl(g) [72].

$Cr_2O_3(s) + 4KCl(s) + 2H_2O(g) + ^3/_2\ O_2(g) \rightleftarrows 2\ K_2CrO_4(s) + 4HCl(g)$ (6.1)
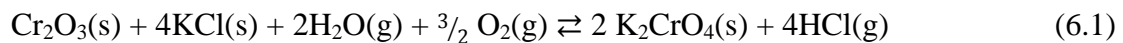
$\Delta G = 147$ kJ/mol, P_{eq}(HCl) = 1300×10^{-6} bar at 600°C, 5% O_2, 40% H_2O

The chromate formation leads to chromium depletion, which results in a breakdown of the protective oxide, i.e. breakaway oxidation. This triggers the formation of a rapidly growing iron-rich oxide and after 24 hours of exposure, the whole surface is covered by a thick oxide, see Figure 28b. Extending the exposure time to 168 hours does not affect the surface morphology considerably [16].
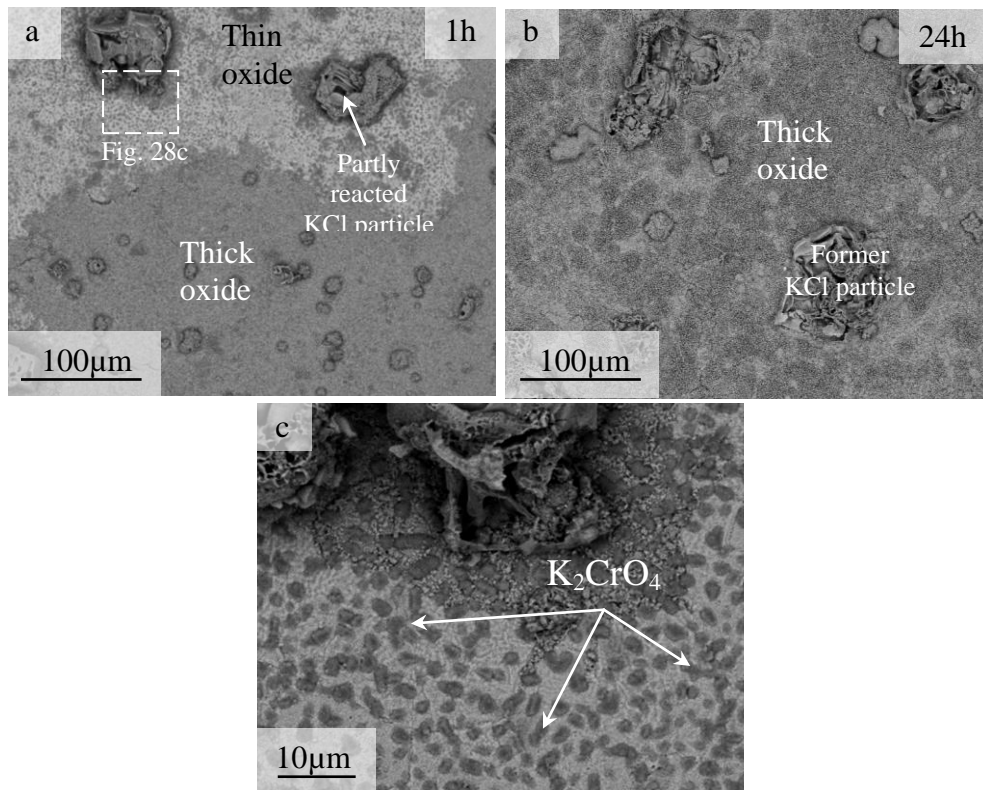
Figure 28: BSE plan view images of samples exposed in 5% O_2 + 40% H_2O + 1.35µmol/cm^2 KCl at 600°C for (a) 1h and (b) 24h (c) Close-up image of the marked area in (a)

The oxide layer formed after 24 hours of exposure is up to 10µm in the thickest part (see Figure 29) and its morphology is similar to the oxide layer formed in the *SRF* exposure (see Figure 26). The oxide scale is duplex and described simply, it consists of an outward-growing iron-rich oxide and inward-growing iron-chromium-nickel-rich spinel oxide. The outward-growing oxide consists of almost pure hematite due to the relatively slow diffusion of chromium ions through the spinel [74, 75]. However, the microstructure of the inward growing oxide has been shown to be more complex. The outer part of this oxide is fully oxidized and consists of an Fe,Cr,Ni-spinel oxide where the cation composition is similar to that for the steel material (minus the iron which has diffused out due to the formation of the outward growing oxide). This part forms very fast and the reaction of its formation is therefore not in equilibrium. However, as the inward growing oxide increases in thickness the diffusion rate through the oxide is slower and equilibrium is reached giving the predicted equilibrium compositions, see Paper V. When this happens nickel is not be able to oxidize due to the low oxygen partial pressure [73]. Instead, iron and chromium form spinel oxide-inclusions in a Fe-Ni-matrix. This is discussed in more detail in paper V. In addition, no chlorine could be detected in the cross-section.
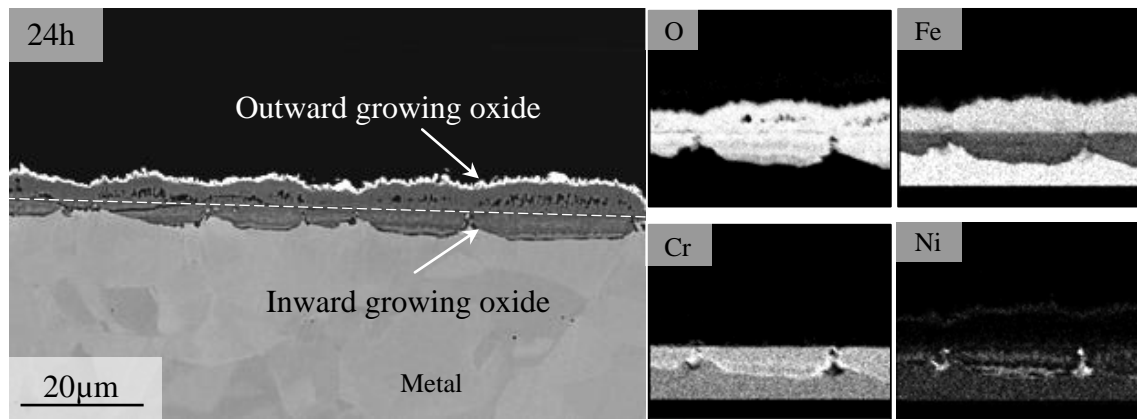
44

Figure 29: BSE image of a BIB cross-section together with EDX maps of a sample exposed at 600°C in 5% O_2 + 40% H_2O + 1.35μmol/cm^2 KCl for 24h.

The deposit formed on the steel sample in the *SRF* case was rich in both KCl and NaCl [11]. In addition, chlorine containing compounds such as $CaCl_2$ may also be found in the fly ash from these kinds of fuels. Therefore, it was investigated whether NaCl and $CaCl_2$ were equal corrosive as KCl. The laboratory exposures show that KCl and NaCl are equally corrosive and strongly increases the corrosion rate. By contrast, exposure in the presence of $CaCl_2$ does not result in a significantly increased mass gain (see Figure 30).
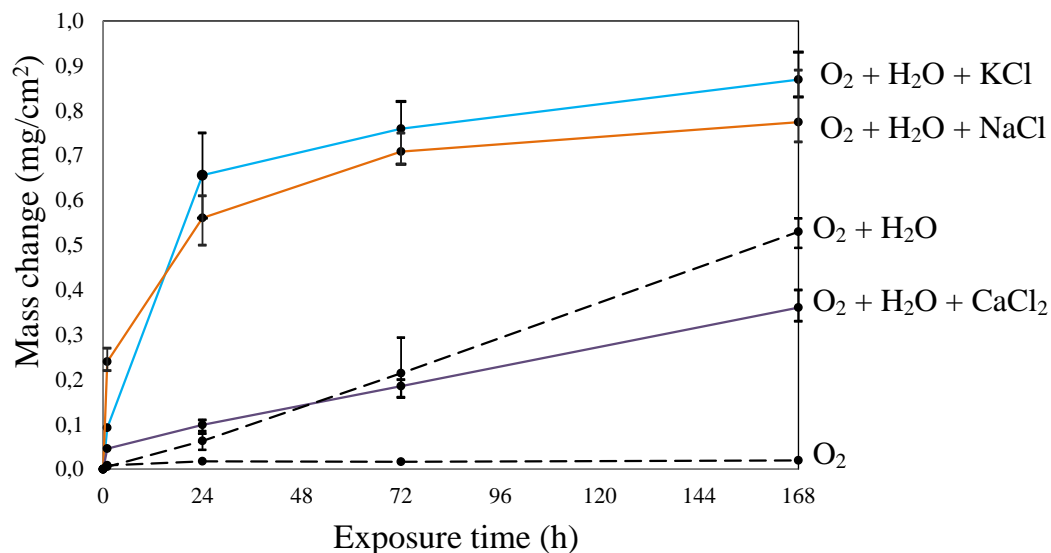

Figure 30: Mass gain versus exposure time for samples exposed with NaCl, KCl or $CaCl_2$ in 5% O_2 + 40% H_2O at 600°C. Reference samples in 5% O_2 and 5% O_2 + 40% H_2O at 600°C are also included (dotted lines) [49].

Samples exposed with small amounts of NaCl showed that the corrosion attack was initiated by sodium chromate (Na_2CrO_4) formation. As for KCl-treated samples, NaCl diffuses out over the surface and then reacts with the chromium-rich oxide according to reaction 6.2. The formation of Na_2CrO_4 results in chromium depletion of the protective oxide which triggers the formation of a rapidly growing iron-rich oxide.

$Cr_2O_3(s) + 4NaCl(s) + 2H_2O(g) + ^3/_2\ O_2(g) \rightleftarrows 2\ Na_2CrO_4(s) + 4HCl(g)$ $\qquad$ (6.2)
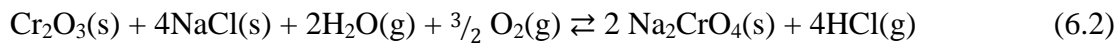
$\Delta G = 163$ kJ/mol, $P_{eq}(HCl) = 740 \times 10^{-6}$ bar at 600°C, 5% O_2, 40% H_2O

The presence of $CaCl_2$ may also deplete the protective oxide in chromium by calcium chromate ($CaCrO_4$) formation according to reaction (6.3). However, under the laboratory conditions chosen, $CaCl_2$ is rapidly converted to calcium oxide (CaO). Calcium chromate can also form by reaction with CaO (reaction 6.4). However, due to the poor mobility of CaO, calcium does not spread over the surface and the reaction between calcium and the protective oxide is limited. The results from all three exposure cases are discussed further in Paper 1.

$Cr_2O_3(s) + 2CaCl_2(s) + 2H_2O(g) + ^3/_2\ O_2(g) \rightleftarrows 2\ CaCrO_4(s) + 4HCl(g)$ $\qquad$ (6.3)
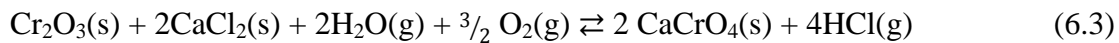
$\Delta G = 127$ kJ/mol, $P_{eq}(HCl) = 2600 \times 10^{-6}$ bar at 600°C, 5% O_2, 40% H_2O

$Cr_2O_3(s) + CaO(s) + 3/2\ O_2(g)\ \rightleftarrows 2\ CaCrO_4(s)$ $\qquad$ (6.4)
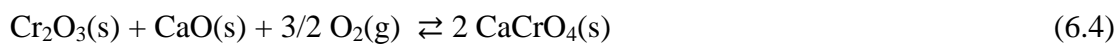
$\Delta G = -112$ kJ/mol at 600°C, 5% O_2

As in the presence of KCl, NaCl results in the formation of a thick oxide scale after 24 hours of exposure [14]. In both cases the oxide is very similar to the oxide layer formed in the *SRF* case. By contrast, there were no signs of oxidation along the steel grain boundaries on the samples exposed in the laboratory while this type of corrosion attack was much more severe on the sample exposed in the *SRF* case. Thus, the laboratory exposure cannot explain the reason for this type of corrosion attack.

A major difference between the laboratory exposures and the field exposure is the amount of alkali chloride covering the samples. In the laboratory exposures the added salt was consumed during the first hours of exposure (see Figure 27). By contrast, after 24 hours of exposure in the *SRF* case, high amounts of KCl and NaCl were detected in the deposit. Therefore it is of great interest to investigate the effects of larger amounts of alkali chlorides in the laboratory to simulate the conditions in the *SRF* case. In order to do so the amount of KCl was increased tenfold to $13.5\mu mol/cm^2$ KCl (referred to as large amount of salt).

Larger amounts of salt resulted in a lower percentage formation of K_2CrO_4. After 1 hour only 2% of the original amount of K^+ had formed K_2CrO_4 (see Figure 31). However, the amount of chromate detected on the sample ($0.16\mu mol/cm^2$) was almost the same as for the samples exposed with small amounts of salt ($0.12\mu mol/cm^2$) [76]. Thus the rate of initial chromate formation is not dependent on the amount of salt. Instead, it depends on the reaction rate of chromate formation. This rate is, in turn, dependent on the steel, e.g. for exposures with Sanicro28, under the same experimental conditions, 100% of the applied KCl formed K_2CrO_4 [77].

After 24 hours of exposure large amounts of unreacted KCl were still present on the surface and the formation of K_2CrO_4 had increased to about 5%, i.e. the amount of chromate formed on the sample was $0.35\mu mol/cm^2$. This is more than double compared to samples exposed for 24 hours with small amounts of KCl ($0.14\mu mol/cm^2$) [76].
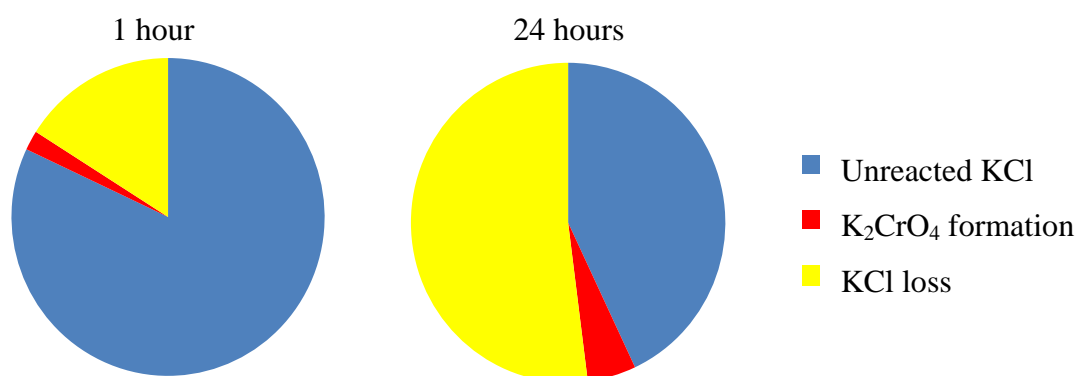

Figure 31: Suggested mass balance based on the IC results, where the amount of water soluble ions detected was measured on samples exposed for 1h and 24h of exposure in 5% O_2 + 40% H_2O + $13.5\mu mol/cm^2$ KCl

The surface morphology on samples exposed with large amounts of salt was very similar to those exposed with small amounts of salt (compare Figure 28a and Figure 28b with Figure 32a and Figure 32b). In contrast to exposures with small amounts of salt, but similar to the *SRF* case, unreacted salt can still be detected on the surface after 24 hours of exposure. The size of the salt particles has not changed considerably during the exposure. Instead they have become more hollow due to KCl-evaporation and the salt being spread out over the surface (see Figure 32c).
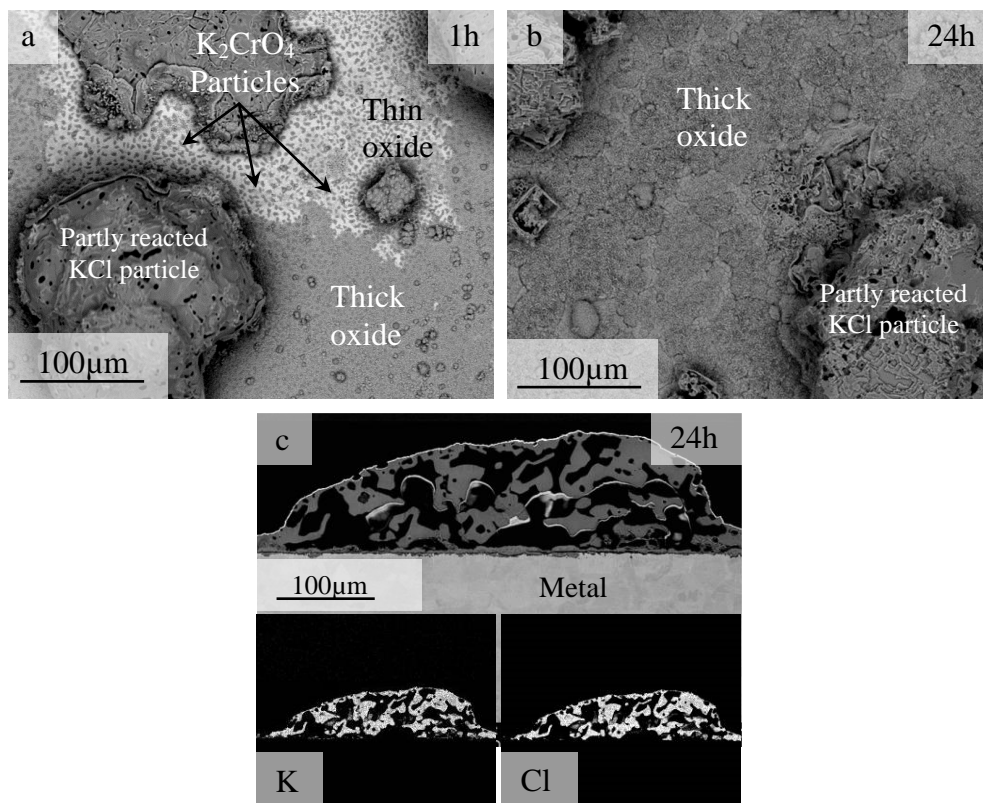
Figure 32: BSE plan view images of samples exposed in 5% O_2 + 40% H_2O + 13.5μmol/cm^2 KCl at 600°C for (a) 1h and (b) 24h (c) BIB cross-section of a KCl particle exposed for 24h and EDX maps for K and Cl

After 24 hours of exposure, two types of corrosion morphologies were found on the sample: the one below a KCl particle and the one between the KCl particles. Between the KCl particles the corrosion attack is very similar to that seen in the *SRF* case (compare Figure 28 and Figure 33), i.e. two types of corrosion morphologies are present: a covering oxide layer and oxidation along the steel grain boundaries. The covering oxide layer has morphology similar to that on samples exposed with small amounts of KCl (Figure 29). By contrast, the layer is thicker, up to 15μm in the thickest part, which demonstrates a

faster corrosion process in the presence of larger amounts of KCl. In addition, the oxidation along the steel grain boundaries also reveals that larger amounts of KCl also induce this type of attack. The change in corrosion morphology may be the result of an increased chromate formation due to the presence of a larger amount of salt. However, it can also be an effect of chlorine induced corrosion since the amount of chlorine in the atmosphere has increased as HCl due to the chromate formation (see reaction 6.1). However, no chlorine was detected in the cross-section.
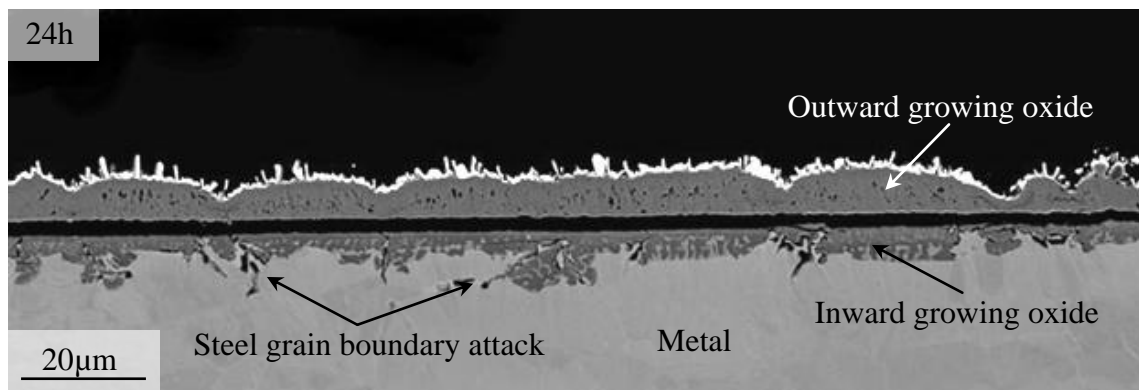

Figure 33: BSE image of a BIB cross-section of a sample exposed at 600°C in 5% O_2 + 40% H_2O + 13.5µmol/cm^2 KCl for 24h

The other type of corrosion morphology (see Figure 34) found on the sample, i.e. in the area below the salt particle is also very similar to the attack on the 304L sample in the *SRF* case (see Figure 26). In contrast to the cross-section performed between the salt particles, the corrosion attack along the steel grain boundaries seems to be more severe under the salt particle. In addition, small amounts of chlorine were detected in the oxide/metal interface. As previous describe, the attacks can be results of the increased chromate formation and the released HCl. However, in this area the gas flow is probably reduced due to the covering salt particle. Therefore it is suggested that HCl has a greater impact beneath a KCl particle since it will be more concentrated here (due to the reduced gas flow) and may be the reason for the increased steel grain boundary attack.

Furthermore, the oxide formed under the KCl particle is in some areas thinner compared to that in Figure 33. This can, however, be explained by reduced access to oxygen due to the covering salt particle.
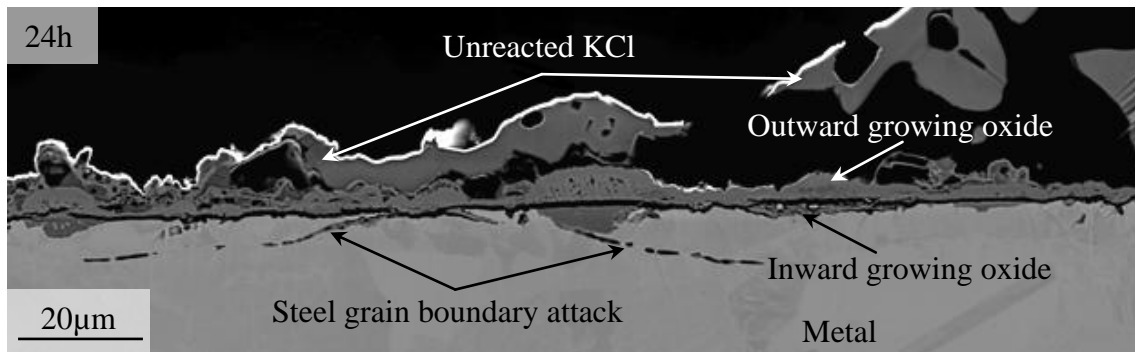
Figure 34: BSE image of a BIB cross-section of a sample exposed at 600°C in 5% O_2 + 40% H_2O 13.5µmol/cm^2 KCl for 24h

6.1.1. Summary of the correlation between field and laboratory exposures

The distinct similarities in corrosion attacks in field and laboratory exposures suggest that the same initial corrosion mechanism occurs in both cases. According to the laboratory exposures, the presence of KCl results in two types of corrosion attacks; the covering oxide layer and the oxidation along the grain boundaries. The formation of the oxide layer is due to chromate formation while the attack along the steel grain boundaries is suggested to be accelerated by an increased presence of chlorine, released from the chromate formation reaction.

In contrast, the oxide formed on 304L in the *SRF* case is much thicker compared to that formed in the laboratory exposure. This can be explained by the deposit that covers the sample. During the exposure, particles from the flue gas stick on the sample surface and with time a thick, covering deposit forms. At the same time the oxide on the steel grows which may result in a mix of oxide and deposit. This mix becomes more porous compared to the oxide formed in the laboratory (i.e. without a deposit) and therefore the diffusion of oxygen through this layer is higher, resulting in a faster oxide growth rate.

6.2. Mitigating superheater corrosion by adding sulphur

One way of mitigating the corrosion rate in biomass and waste-fired boilers is by increasing the amount of sulphur in the fuel, e.g. by means of fuel additives or by co-combustion of sulphur-rich fuels (see section 6.5). The main aim is to increase the amount of SO_2 in the flue gas in order to sulphate corrosive alkali chlorides to less corrosive alkali sulphates according to reaction 6.5 and 6.6.

$$2KCl(s) + SO_2(g) + H_2O(g) + \tfrac{1}{2} O_2(g) \rightleftarrows K_2SO_4(s) + 2HCl(g) \tag{6.5}$$
$$\Delta G = -78kJ/mol \text{ at } 600°C$$
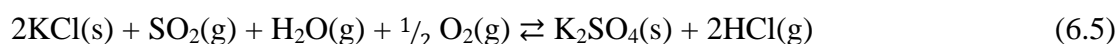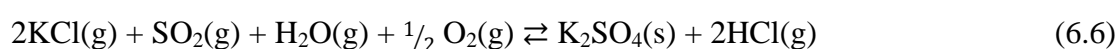
$$2KCl(g) + SO_2(g) + H_2O(g) + \tfrac{1}{2} O_2(g) \rightleftarrows K_2SO_4(s) + 2HCl(g) \tag{6.6}$$
$$\Delta G = -262kJ/mol \text{ at } 600°C$$

The reaction can also occur through a reaction with SO_3 (see reaction 6.7 and 6.8) which may be present in the flue gas due to oxidation of SO_2 to SO_3. However, this study focuses on reactions with SO_2.

$$2KCl(s) + SO_3(g) + H_2O(g) \rightleftarrows K_2SO_4(s) + 2HCl(g) \tag{6.7}$$
$$\Delta G = -62kJ/mol \text{ at } 600°C$$
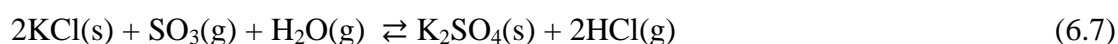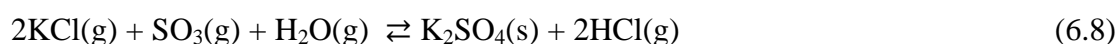
$$2KCl(g) + SO_3(g) + H_2O(g) \rightleftarrows K_2SO_4(s) + 2HCl(g) \tag{6.8}$$
$$\Delta G = -245kJ/mol \text{ at } 600°C$$

Several studies have shown that the use of sulphur-rich fuel additives or co-combustion with a sulphur-rich fuel results in a decreased corrosion attack [6, 11, 24-36]. However, the link between the reaction kinetics and the corrosion attack has not been fully studied. This is, however, of great interest since the sulphation reaction simultaneously releases the corrosive species HCl. In addition, high amounts of sulphur in the flue gas are known to cause the increased rate of high-temperature corrosion of several metals due to sulphide formation [39]. In addition, the presence of metal-sulphides is suggested to decrease the scale adhesion which induces spallation of the oxide layer [40].

To investigate the initial effect of co-firing with a sulphur-rich fuel, short time exposures (24 hours) of 304L at 600°C (material temperature) were performed in the CFB boiler located at Chalmers University of Technology. Two fuel-mixes were investigated: SRF with municipal sewage sludge, low dosage (referred to as the *MSS1-low* case) and SRF with municipal sewage sludge, high dosage (referred to as the *MSS2-high* case). Again, well-controlled laboratory exposures were included in order to investigate the sulphation mechanisms.

The co-combustion changed the flue gas chemistry in the boiler (see Figure 36). By adding sewage sludge the alkali content in the flue gas decreased from 96 ppm to 28 ppm in the *MSS1-low* case, while the SO_2 content remained the same. In the *MSS2-high* case, the alkali content decreased to only 3 ppm and the concentration of SO_2 increased to almost 70ppm. As the alkali concentration decreased due to sulphation, chlorine in the form of HCl was released and increased from 12 ppm (*SRF* case) to 316 ppm (*MSS2-high*).
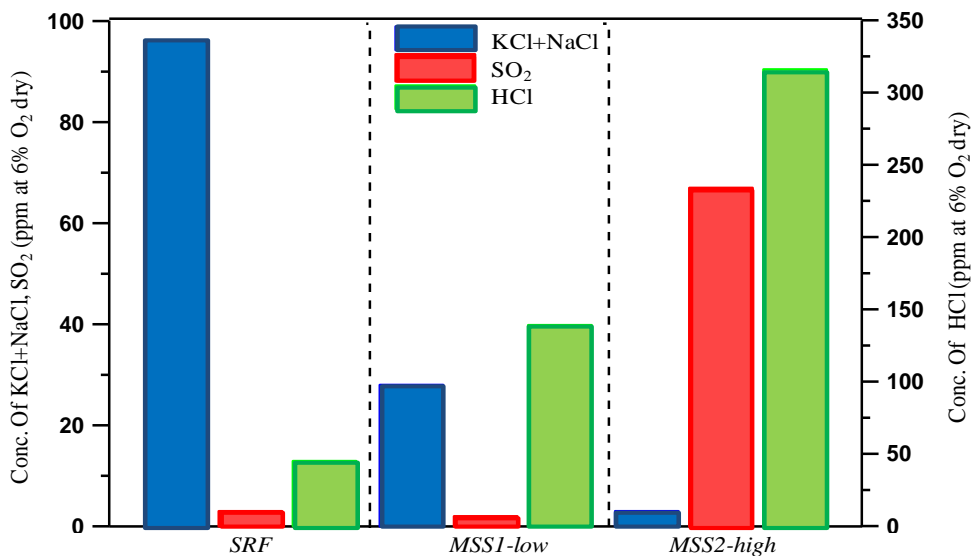
Figure 35: Concentration of alkali chlorides (KCl + NaCl), HCl and SO_2 before the convection pass recalculated on dry gas at 6% O_2

The change in flue gas chemistry was clearly reflected on the composition of the deposit formed on the sample rings (see results from the IC-analysis in Figure 36). After 24 hours of exposure without co-combustion (case *SRF*), the deposit was dominated by Cl^-. For the *MSS1-low* case the distribution of Cl^- and SO_2^{4-} in the deposit was almost equal while it was dominated by SO_4^{2-} in the *MSS2-high* case.

52
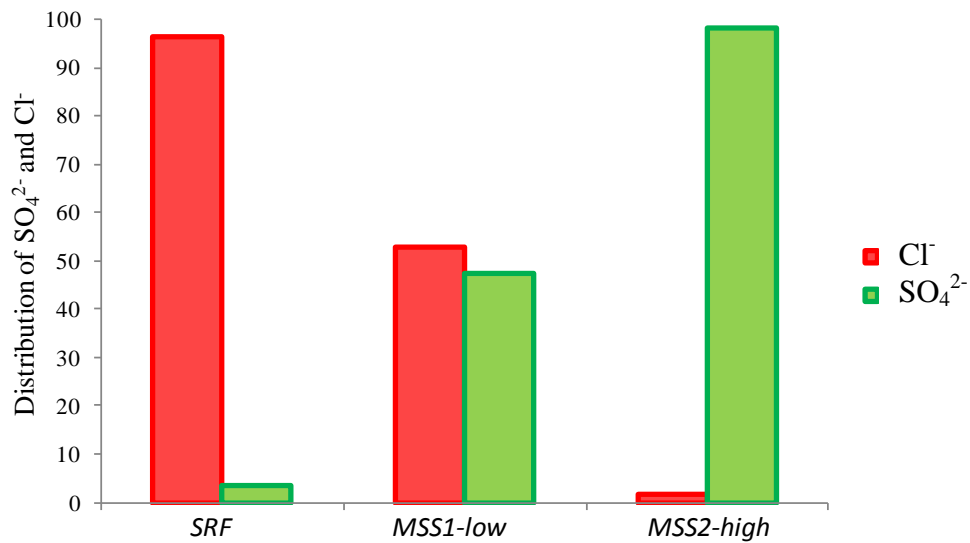
Figure 36: Percent distribution between sulphate ions and chloride ions in the deposit formed in the exposure cases.

The covering deposit layer formed in the *MSS2-high* case (see Figure 37) consists mainly of alkali sulphates, alkali phosphates and alkali aluminum silicates [11]. This is because the municipal sewage sludge used contains high levels of sulphur, phosphorus and aluminum silicates, all with the ability to react with alkali chlorides to form the less corrosive, previously mentioned, compounds. For more information about the reaction with alkali chlorides and phosphorus or aluminum silicates, see paper III.

In contrast to the *SRF* case (see Figure 26), no alkali chlorides can be detected in the deposit. Furthermore, no corrosion product layer can be seen between the steel sample ring and the deposit layer and there are no signs of corrosion attacks along the steel grain boundaries.
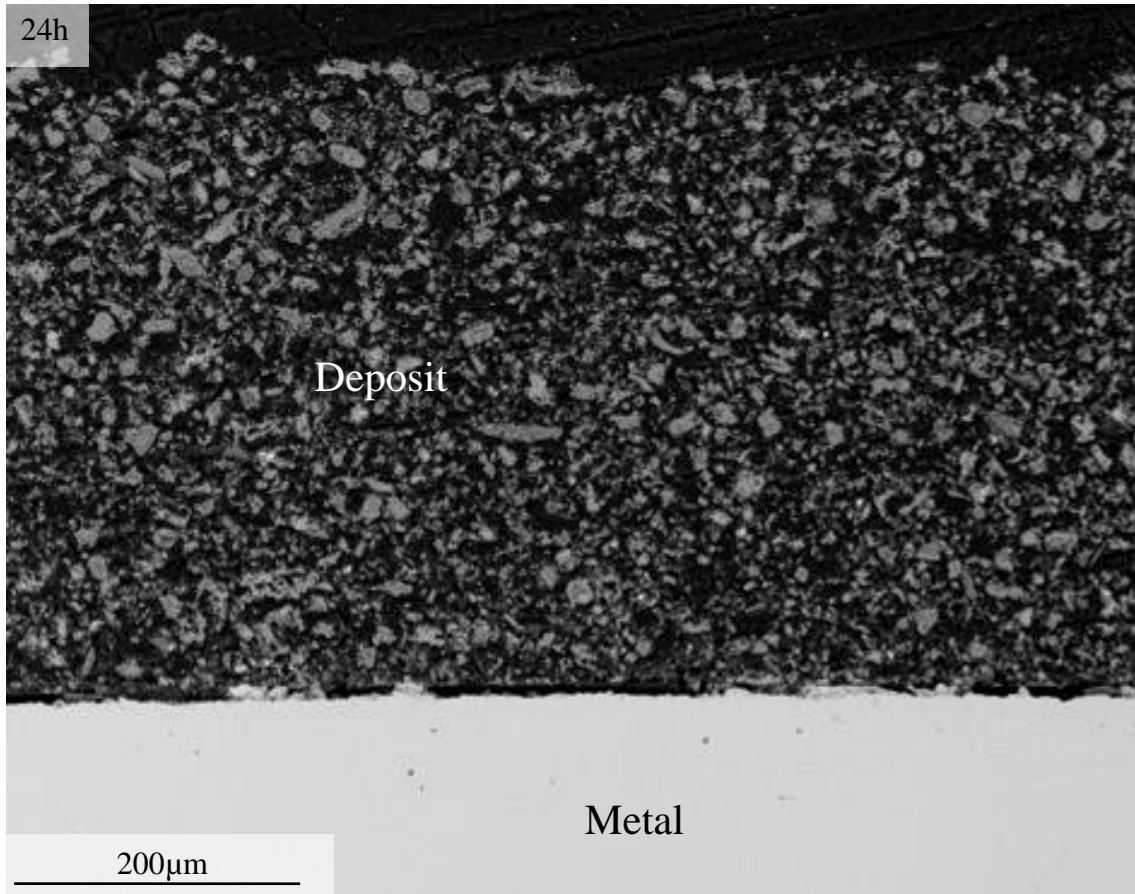
Figure 37: BSE image of a cross-section of the 304L sample exposed in the *MSS2-high* case for 24h at 600°C.

As shown in the flue gas analysis (see Figure 35), the addition of the high dosage of sludge to the *SRF* case results in a reduction of gaseous alkali chlorides from 96 ppm to 3 ppm. Meanwhile the SO_2 content increased from a few ppm to almost 70ppm. Hence the sulphation reaction probably takes place mostly in the flue gas according to reaction 6.6. Therefore, the deposit formed on the samples mostly consists of less corrosive alkali sulphates (and alkali phosphates and alkali aluminum silicates). In contrast to potassium chloride, K_2SO_4 does not induce an accelerated corrosion attack on 304L steel at 600°C [63]. The non-corrosive nature of K_2SO_4 is explained by its thermodynamic stability (see reaction 6.9 and 6.10). Hence, the reaction of K_2SO_4 with the protective oxide to form K_2CrO_4 is not thermodynamically favoured under the present experimental conditions:

$$Cr_2O_3(s) + 2K_2SO_4(s) + \tfrac{1}{2} O_2(g) \rightleftarrows 2 K_2CrO_4(s) + 2SO_2(g) \tag{6.9}$$

$\Delta G = 304$ kJ/mol, $P_{eq}(SO_2) = 7.7 \times 10^{-20}$ bar at 600°C, 5% O_2

and/or

$$Cr_2O_3(s) + 2K_2SO_4(s) + \tfrac{3}{2} O_2(g) \rightleftarrows 2 K_2CrO_4(s) + 2SO_3(g) \qquad (6.10)$$
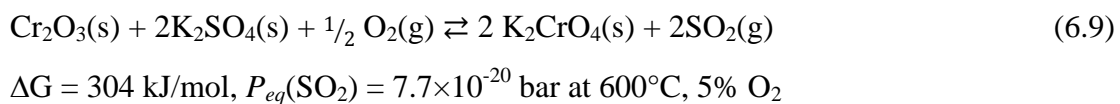
$\Delta G = 270kJ/mol$, $P_{eq}(SO_3) = 8.9 \times 10^{-10}$ bar at 600°C, 5% O_2

If most of the conversion from alkali chlorides to alkali sulphates occurs in the flue gas, the steel never comes into contact with the alkali chlorides and chromate depletion is not possible in these conditions. Instead, the steel is covered by a non-corrosive deposit. In addition, the sulphation reaction releases high amounts of HCl (315 ppm), which might be disadvantageous from a corrosion point of view. However, since there were no signs of chlorine in the deposit or in the steel grain boundaries [11], the high release of HCl do not affect the corrosion in this case. However, in the *MSS1-low* case, where a lower dosage of sludge was used, the situation was different.

In the *MSS1-low* case, the gaseous alkali chloride content was reduced from 96 ppm (*SRF* case) to 28 ppm while the HCl content increased from 45 ppm to 150 ppm (see Figure 35). The SO_2 content remained the same, i.e. 3ppm. Thus the amount of sludge in this case was insufficient to sulphate the whole amount of alkali chlorides in the fuel.

The composition of the deposit seen in the cross-section in Figure 38 resembles that of the deposit formed in the *MSS2-high* case (Figure 37), i.e. it consists of alkali sulphates, alkali phosphates and small amounts of alkali aluminium silicates. In contrast, there were no signs of corrosion attacks in the *MSS2-high* case while a distinct corrosion attack is seen in the *MSS1-low* case.

As in the *SRF* case (Figure 26), the environment in the *MSS1-low* case resulted in two types of corrosion morphologies: the covering oxide layer and the oxidation along the steel grain boundaries (see Figure 38). The covering oxide layer has the same composition as in the *SRF* case. In contrast, the oxide is significantly thinner. Most of the steel grain boundaries are attack but the attacked does not penetrate as deeply as in the *SRF* case.
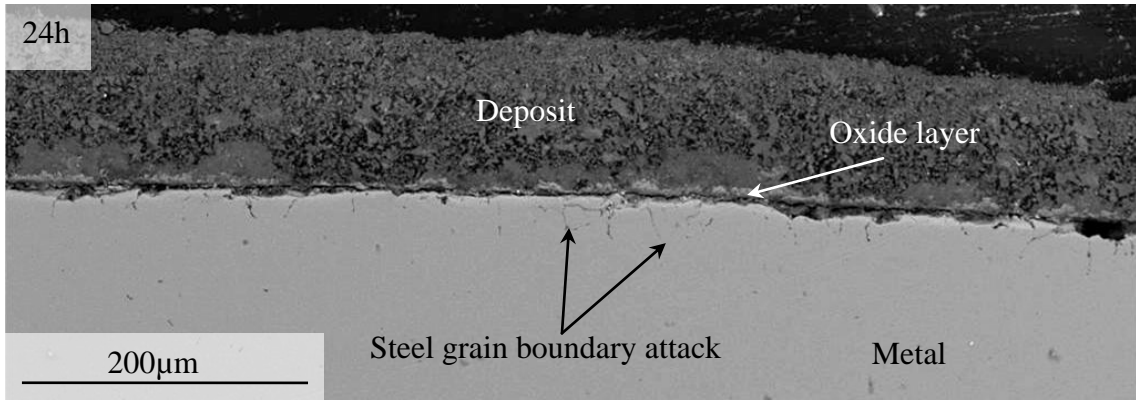
Figure 38: BSE image of a cross-section of the 304L sample exposed in the *MSS1-high* case for 24h at 600°C

In addition, chlorine and sulphur could be detected in the steel grain boundaries in some areas in the *MSS1-low* case (see close-up image and EDX maps of the steel sample ring in Figure 39).
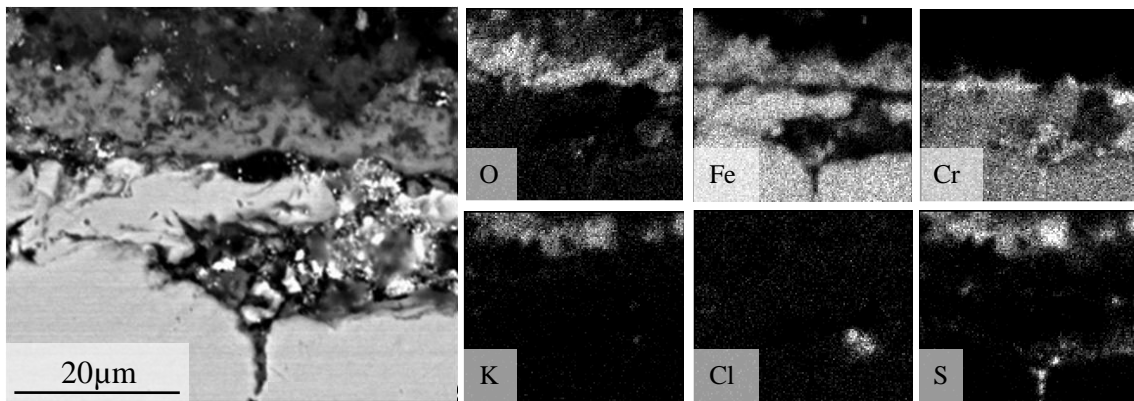
Figure 39: Close-up BSE image of the oxide formed on the 304L sample exposed in the *MSS1-low* case for 24 hours at 600°C and EDX maps

Even if the covering deposit in the cross-section area for case *MSS1-low* and case *MSS2-high* has a similar composition, the corrosion attack is totally different. In contrast, the flue gas chemistry was very different for both cases (see Figure 35) which resulted in a very different composition of the whole deposit formed on the sample ring (see Figure 36). In *MSS1-low* case, the deposit contains both alkali chlorides and alkali sulphates while the amount of alkali chlorides in the *MSS2-high* case is very low. The reason for the increased corrosion rate in the *MSS1-low* case, compared to the *MSS2-high* case, could therefore be the high amount of alkali chlorides in the deposit that initiate the corrosion attack in a similar way as was shown in the laboratory exposures with KCl (section 6.1).

56

However, as previously mentioned, no alkali chlorides can be detected in the area in Figure 36 and Figure 37. Instead the steel sample is covered by a deposit mostly rich in alkali sulphate which did not result in an increased corrosion in the *MSS2-high* or in the laboratory exposures with K_2SO_4 [63, 78]. Can this mean that the sulphation of the alkali chlorides has occurred on the steel surface and therefore initiated the corrosion? And if so, can sulphation of alkali chlorides on the steel surface result in sulphidation and chlorination of the alloy grain boundaries as shown in Figure 39?

In order to simulate this in the laboratory, 304L samples were sprayed with small amounts of salts (1.35µmol KCl/cm^2) and then exposed in 5% O_2 + 40% H_2O + 300ppm SO_2 at 600°C. The introduction of SO_2 to the atmosphere decreases the mass gain of the KCl-coated samples considerably (see Figure 40). However, compared to the samples exposed with K_2SO_4 (which does not induce any accelerated corrosion), it is clear that the simultaneous presence of KCl, SO_2 and H_2O induces an increased corrosion rate.
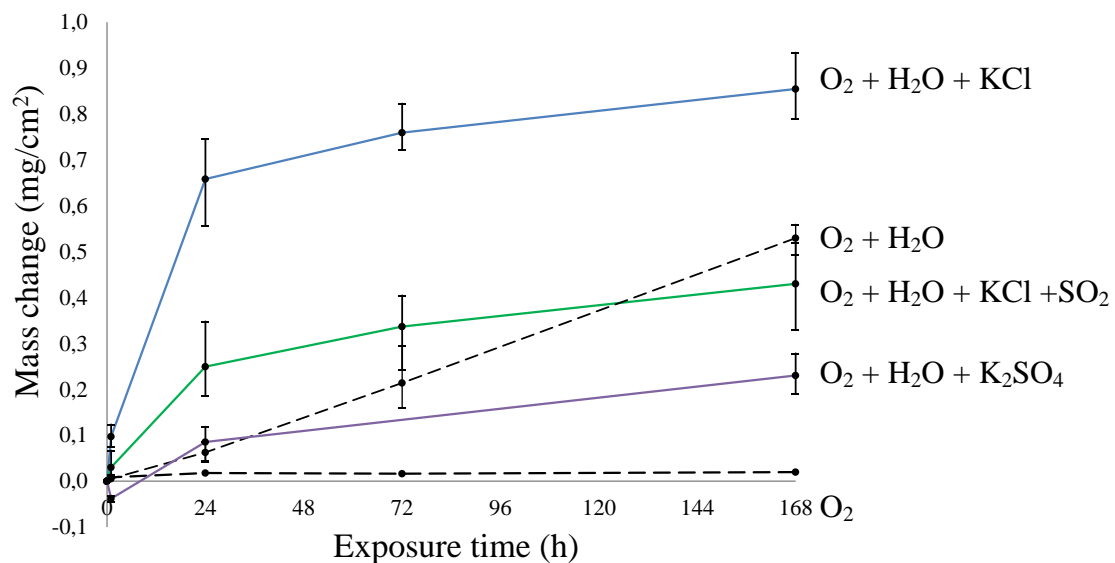
Figure 40: Mass gain versus exposure time for samples exposed with KCl, KCl + 300ppm SO_2 and K_2SO_4 at 600°C. Reference samples in 5% O_2 and O_2 + 40% H_2O at 600°C are also included (dotted lines) [49]

The sulphation of KCl (according to reaction 6.5) was shown to be very fast. After only 15 minutes more than 50% of the KCl applied has reacted with SO_2 to form K_2SO_4 [78]. After 1 hour of exposure only 6% unreacted KCl is detected while after 24 hours of the salt is more or less consumed (see Figure 41). The very fast sulphation rate results in a

very low KCl evaporation. After 24 hours of exposure the KCl loss, mostly by evaporation, is less than 10%. For exposures without SO_2 and small amounts of KCl, almost 80% of the applied salt had evaporated after this period of exposure (Figure 27). The large difference in KCl evaporation in both cases depends on the difference in rate of reaction in which KCl takes part. In the absence of SO_2 potassium chloride reacts with the steel and K_2CrO_4 is formed. This reaction was shown to be quite slow on 304L compared to the evaporation rate of KCl, less than 20% of the applied salt formed K_2CrO_4. The sulphation reaction of KCl that occurs in the presence of SO_2 was shown to be much faster than the chromate formation reaction and as a result a lower amount of KCl was evaporated. Therefore it is a higher release of HCl in the SO_2 atmosphere, since this is a product for both the sulphation reaction and the chromate reaction.
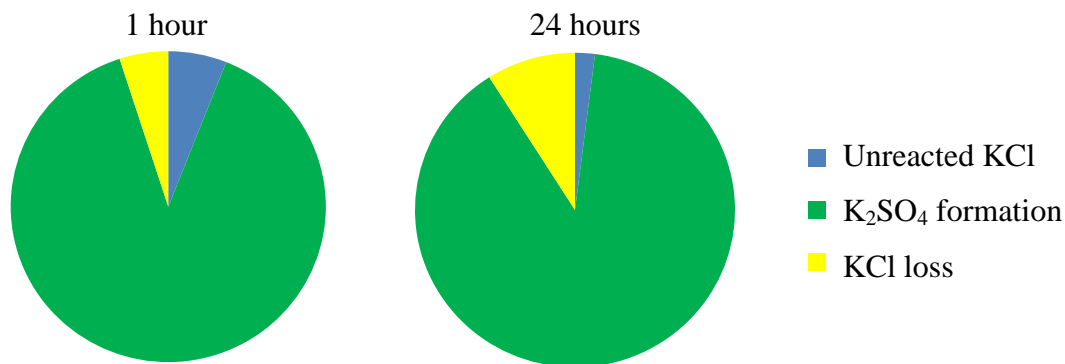
Figure 41: Suggested mass balance based on the IC results, where the amount of water soluble ions detected was measured on samples exposed for 1h and 24h of exposure in 5% O_2 + 40% H_2O + 300 ppm SO_2 + 1.35µmol/cm^2 KCl

After 1 hour of exposure in the presence of SO_2 the surface is covered by a thin chromium-rich oxide (see Figure 42a). On top of the oxide a thin layer of K_2SO_4 has formed [78]. Thus the simultaneous presence of KCl, SO_2 and H_2O induces the fast transport of KCl over the surface where it reacts with the atmosphere and forms K_2SO_4. With an increased exposure time an iron-rich oxide starts to grow on the sample surface and after 24 hours of exposure a large part of the surface is covered by a thicker oxide scale (see Figure 42b) covered by K_2SO_4 particles (see close-up image in Figure 42c). However, in contrast to samples exposed in the absence of SO_2 (see Figure 28b), areas with thin and protective oxide are still present. The fact that the surface morphology on samples exposed in the presence of SO_2, for 24 hours, is very similar to that exposed in the absence of SO_2, but for only 1 hour, shows that presence the of SO_2 slows down the

corrosion rate. However, the presence of SO_2 does not inhibit the corrosion enough and after 168 hours of exposure the whole surface is covered by an iron-rich oxide [73].
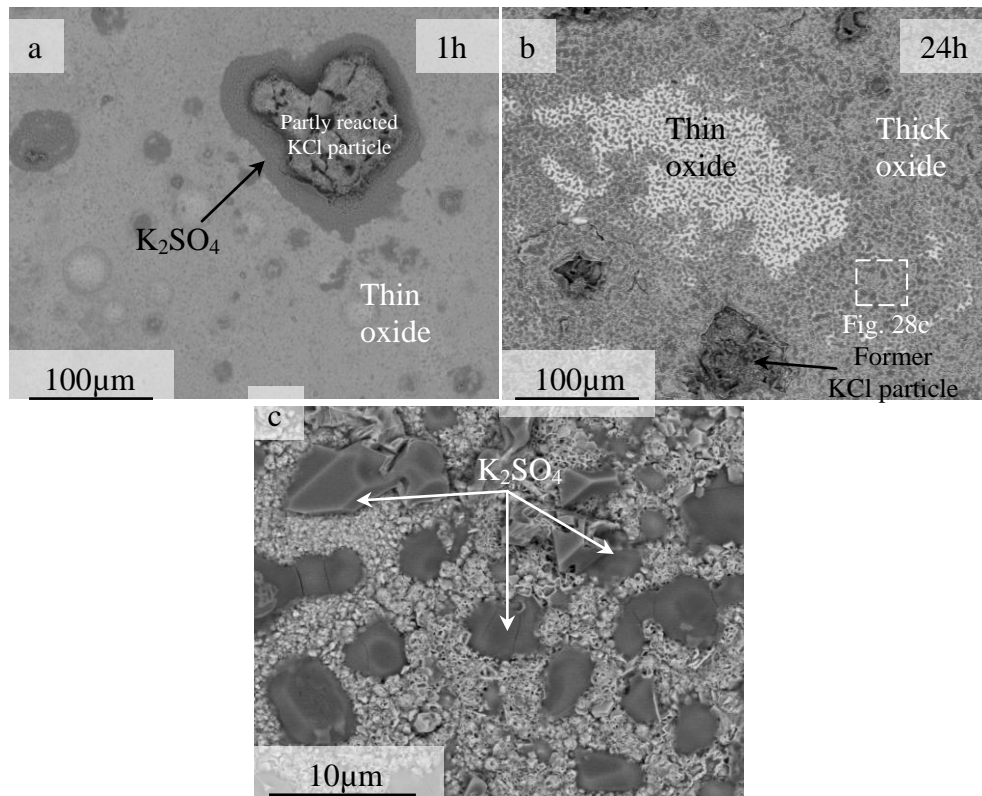
Figure 42: BSE plan view images of samples exposed in 5% O_2 + 40% H_2O + KCl + 300 ppm SO_2 at 600°C for (a) 1h and (b) 24h. Close-up image of the marked area in (b)

The corrosion morphology on samples exposed for 24 hours is similar to that seen on samples exposed in the absence of SO_2 (compare Figure 29 and Figure 43). By contrast the oxide is thinner, up to 2µm compared to 10µm for samples exposed in the absence of SO_2. In addition, in some areas the inward growing oxide is so thin that it is hard to distinguish. Another interesting difference between samples exposed with small amount of salt in the absence of and in the presence of SO_2 is that the latter case induces oxidation along the grain boundaries. This can be seen in many of the grain boundaries and the depth of the penetrations of the oxidation varies between 1-4 µm (in a few areas it is up to 8µm). Sulphur is always detected in the attacked grain boundaries (see EDX maps of the marked area in Figure 43), showing that sulphide formation has also occurred. In addition, the samples were coated with a thin Au layer during sample preparation. Due to an overlap the Au layer appears in the S map. However, the sulphur containing compounds found on the surface was only identified as K_2SO_4 (SEM/EDX and XRD).

Figure 43: BSE image of a BIB cross-section of a sample exposed at 600°C in 5% O_2 + 40% H_2O + 300ppm SO_2 + 1.35μmol/cm^2 KCl for 24h and EDX maps for the marked area

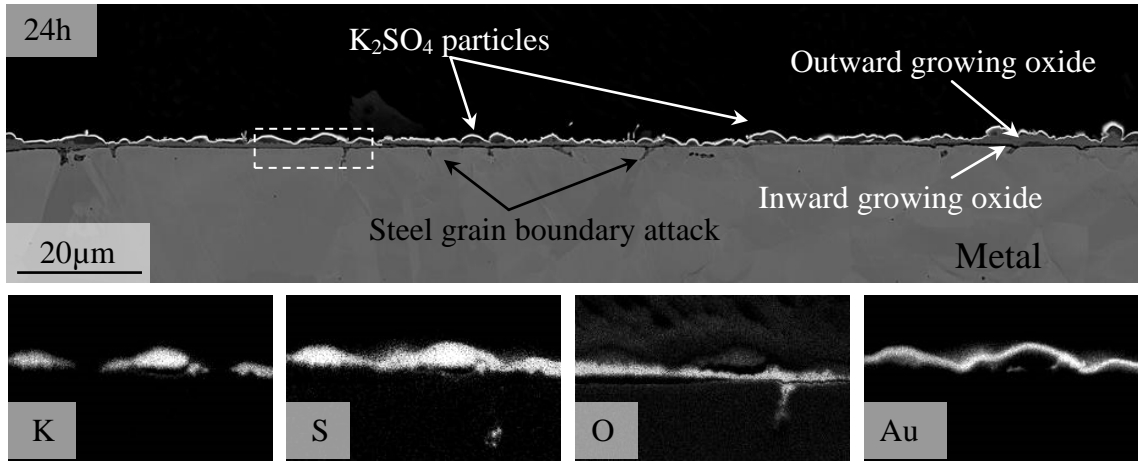The results show that the presence of SO_2 on KCl-treated samples gives a slower oxide growth than for KCl-treated samples exposed in the absence of SO_2. However, the oxide on samples exposed in KCl + SO_2 for 168 hours is about four times thicker than that on the samples exposed in SO_2 for 168 hours (see Figure 9b in section 3.3). Thus KCl has had a corrosive effect despite the presence of SO_2. It is therefore suggested that small amounts of KCl react initially with the protective oxide and, by chromate formation, deplete the oxide in chromium (see reaction 6.1). The depletion leads to the formation of a non-protective iron-rich oxide. However, due to the presence of SO_2, K_2CrO_4 reacts immediately with SO_2 to form K_2SO_4 according to reaction 6.11. This reaction has been shown to be extremely fast which can account for the absence of chromates on the sample [78]. In addition to the corrosion mitigation effect of sulphation of KCl, it has been shown that sulphate is adsorbed at the scale/gas interface. The sulphate adsorbed has been suggested to slow down chromium volatilization and to decrease the rate of oxygen reduction on the oxide surface [53], see section 3.3.

$$2K_2CrO_4(s) + 2SO_2(g) \rightleftarrows 2K_2SO_4(s) + Cr_2O_3(s) + {}^1\!/_2 O_2 (g) \qquad\qquad (6.11)$$
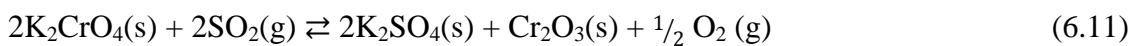
where ΔG = -304kJ/mol.

In contrast to the reduced corrosion rate, the presence of SO_2 induces sulphide formation along the steel alloy grain boundaries and in the metal/oxide interface. This is undesirable from a corrosion point of view since the diffusion rate in sulphides is generally much faster than that in the corresponding oxides [39]. Exactly how the sulphide formation

occurs is not fully understood. One suggestion is that some of the sulphate, which initially absorbs on the surface, gets overgrown by the outward-growing hematite. The incorporation of sulphur leads to a reduction of the sulphate when the activity of oxygen drops. The reduced sulphur then diffuses in the grain boundary and at the metal/scale interface, where the activity of iron is high, the formation of iron sulphide becomes possible [79].

In the *MSS1-low* case, chlorine was also found in the alloy grain boundaries (see Figure 38). This was not seen on the samples in the laboratory exposure. Therefore it is of great interest to investigate the effect of SO_2 with larger amounts of KCl in the laboratory since this result in a higher release of HCl due to the fast sulphation reaction. The amount of KCl was consequently tenfold to 13.5µmol/cm^2.

Even though the rate of sulphation is high, the total sulphation of the larger amount of KCl takes longer compared to small amounts of KCl; after 1 hour of exposure almost 70% of the applied salt remains unreacted (see Figure 41 and compare with Figure 41). However, after 24 hours of exposure almost all KCl had reacted, less the 1 % unreacted salt is detected. Larger amount of salt result therefore in a longer simultaneous presence of KCl and SO_2 on the sample and a greater releases of HCl (according to reaction 6.5) compared to samples exposed with small amounts of KCl in the same environment.
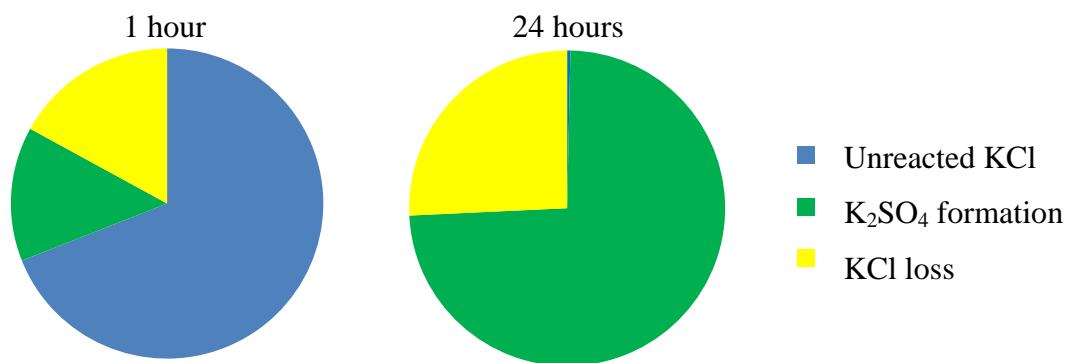

Figure 44: Suggested mass balance based on the IC results, where the amount of water soluble ions detected was measured on samples exposed for 1h and 24h of exposure in 5% O$_2$ + 40% H$_2$O + 300 ppm SO2 + 13.5µmol/cm^2 KCl

The surface morphology of samples exposed with large amounts of KCl in the presence of SO_2 was very similar to the samples exposed in the corresponding atmosphere but with small amounts of salt. After 1 hour of exposure the thin oxide chromium-rich oxide, which covers the sample, is covered by a thin K_2SO_4-layer. In contrast to the exposures with small amounts of salt, a thin layer of chlorine is detected between the sulphate layer and the thin oxide [78]. After 24 hours of exposure most of the surface is covered by a dark layer of K_2SO_4. The former salt particles, which have been completely converted to K_2SO_4, and have become very porous due to a fast transport of KCl from the salt particle and out over the surface (see BIB cross-section in Figure 45c).
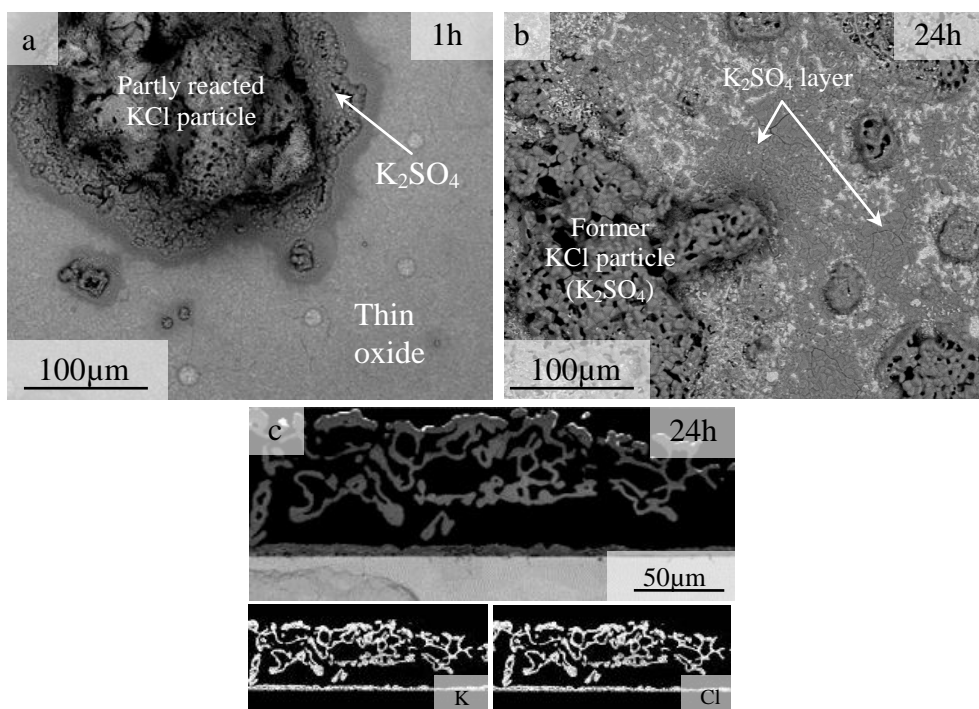
Figure 45: a) BSE plan view images of samples exposed in 5% O_2 + 40% H_2O + 13.5µmol/cm^2 KCl + 300 ppm SO_2 at 600°C for (a) 1h and (b) 24h (c) BIB cross-section of a KCl particle exposed for 24h and EDX maps for K and Cl.

After 24 hours of exposure, two types of corrosion morphologies were found on the sample, one below a former KCl particle and the other between the former KCl particles. Below the former KCl particle the sample is covered by a thin (up to 2µm thick) oxide. The oxide is covered by mixed layer of K_2SO_4 and iron oxide. This is probably due to a simultaneous sulphation of KCl and oxide growth. The oxide is very similar to the oxide form in the same atmosphere but with small amounts of KCl. In contrast, the oxidation along the steel grain boundaries has dramatically increased. Similar to the samples

exposed with small amounts of salt, evidence of sulphide formation can be seen in the steel grain boundaries (see EDX maps of the marked area). In contrast, chlorine can here be detected in the same area. This clearly shows that the presence of large amounts of KCl(s) on 304L in a SO_2 environment accelerates the corrosion attack along the steel grain boundaries by chlorine induced corrosion.

The corrosion attack along the grain boundaries is very similar to that exposed with the same parameters but in the absence of SO_2, see Figure 34. However, in that case there were no signs of chlorine. This might be explained by a higher amount of released HCl present in the SO_2 atmosphere. As previously explained, HCl is released in both atmospheres due to the K_2SO_4 formation (in the presence of SO_2) and the K_2CrO_4 formation (in the absence SO_2). However, more HCl is released in the sulphation reaction due to a faster reaction rate. In addition, more grain boundaries were attacked in the SO_2 environment. This might mean the chlorination of the grain boundaries is facilitated by the presence of sulphides.
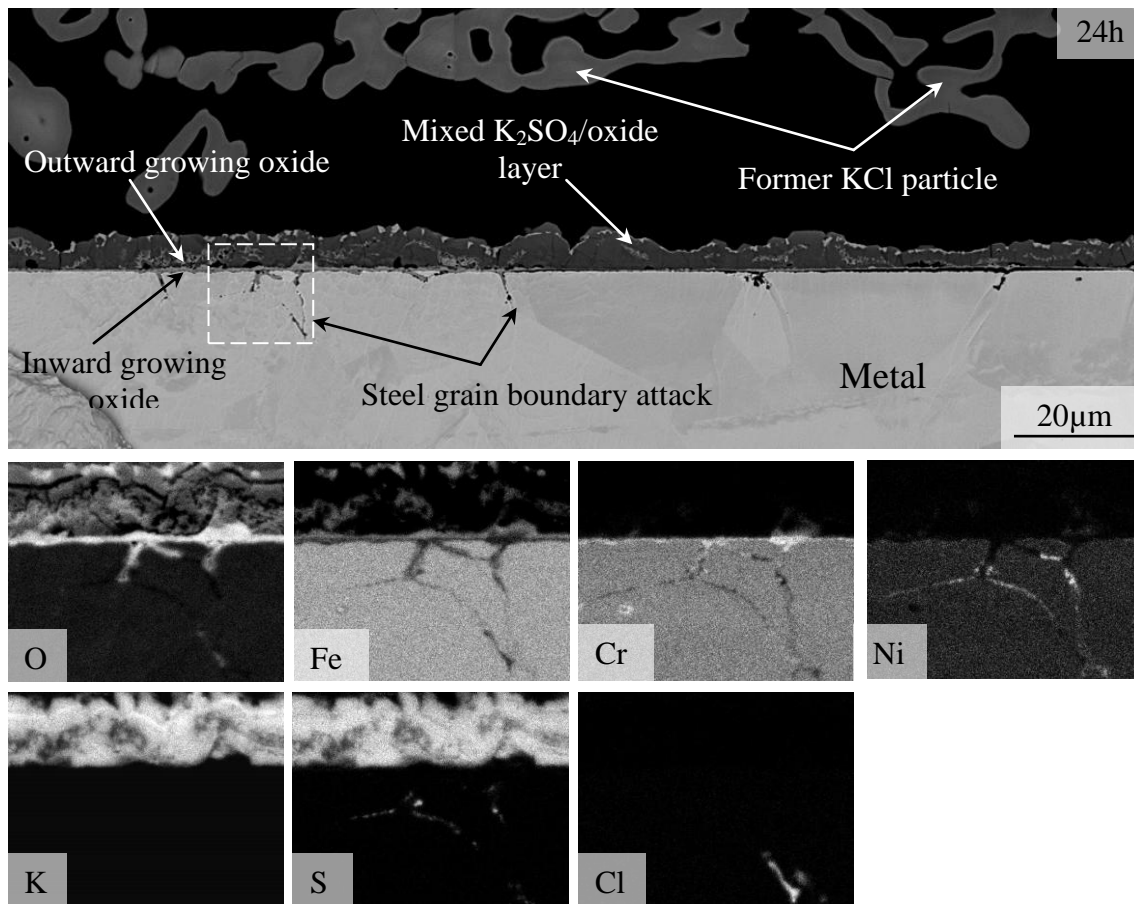

Figure 46: BSE image and EDX maps of a BIB cross-section of a sample exposed at 600°C in 5% O_2 + 40% H_2O + 300ppm SO_2 + 13.5µmol/cm^2 KCl for 24h and EDX maps of the marked area

Under the K_2SO_4 layer between the former KCl-particles (see Figure 47) the situation is completely different. Here there are no signs of oxide formation. Instead the steel surface is covered by a comprehensive K_2SO_4-rich layer. Some iron can also be detected in this layer. Therefore it is suggested that this layer has formed very fast and is most probably acting as a barrier, reducing the oxygen access. However, small amounts of sulphide and/or chlorine formation were found along the steel grain boundaries in the metal/K_2SO_4-layer interface. A suggestion is therefore that chlorine, released by the sulphation reaction 6.5, and sulphur from the SO_2 in the atmosphere have been incorporated during the formation of the layer. Important to emphasize though is that the atmosphere in a boiler is much more complex than in the laboratory, the formation of a protective layer of K_2SO_4 most probably only happen if the sulphating reaction occurs in the flue gas as in the *MSS2*-high case.
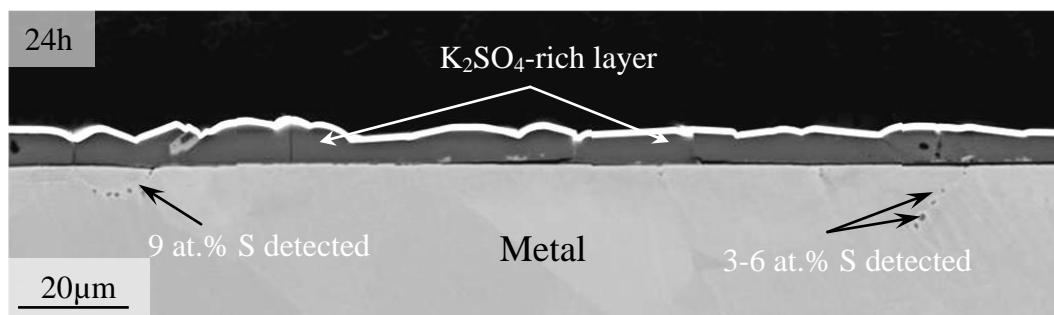
Figure 47: BSE image of a BIB cross-section of a sample exposed at 600°C in 5% O_2 + 40% H_2O + SO_2 + 13.5µmol/cm^2 KCl for 24h

6.2.1. Summary of the correlation between field and laboratory exposures

The corrosion rate of stainless steel in a waste-fired boiler can be greatly reduced by means of co-combustion with sulphur-rich municipal sewage sludge. This is due to the conversion from corrosive alkali chloride to less corrosive alkali compounds, e.g. alkali sulphates. The non-corrosive effect of alkali sulphate is explained by its inability to react with the chromium-rich oxide to form alkali chromates. If the amount of sludge was sufficiently high, most of the gaseous alkali chlorides were converted to alkali sulphates in the flue gas and the steel material was covered by a non-corrosive deposit.

If the amount of sludge was insufficient to sulphate a larger amount of gaseous alkali chlorides in the flue gas, a corrosion attack was introduced on the steel. The laboratory

exposures show that this can be an effect of the fact that alkali chlorides have been sulphated on the steel surface. This scenario generates a simultaneous alkali chromate formation and alkali sulphate formation. The chromate formation results in chromium depletion which increases the growth rate of an iron-rich oxide scale. The presence of SO_2, however, reduces the chromate formation due to sulphating of KCl and the attack is less severe compared to the exposure in the *RDF* case.

In contrast, the presence of SO_2 did not reduce the corrosion attack along the steel grain boundaries. Instead, more steel grain boundaries were attacked compared to exposures in the absence of SO_2 and sulphides and chlorine was detected in this area. This can be explained by a higher release of HCl due to the very fast sulphation reaction. In addition, sulphidation of steel grain boundaries may facilitate the chlorination. However, to understand the mechanism behind the attack more research has to be performed.

Even if the corrosion mechanisms behind the corrosion attacks in section 6.1 and 6.2 are not fully understood the results shows the importance of insuring that the amount of sulphur in the fuel is sufficiently high when adding sulphur-rich additives or by co-combust with a sulphur-rich fuel. By controlling the amount of sulphur in the right way, the majority of alkali chlorides can be sulphated directly in the in the flue gas. In this way the simultaneous presence of alkali chlorides and SO_2 on the steel surface will be limit and oxide formation and the introduction of sulphide/chlorine induced corrosion may be avoid.

6.3. The propagation step

The corrosion studies performed in section 6.1 and 6.2 were based on the initiation of the corrosion. This part of the corrosion describes the mechanism that breaks down the protective scale, i.e. the starting condition is a clean metal surface. When the protective oxide is destroyed a less protective oxide forms. This oxide layer is a barrier layer between the metal and the corrosive deposit/atmosphere and therefore new types of corrosion mechanisms occur. This can be called the propagation step.

The initiation step is very short compared to the propagation step. In the *RDF* case (see Figure 26), the oxide was up to 100μm after only 24 hours, i.e. the propagation step has already started. As shown in Paper V, the oxide layer formed on 304L is very complex [73]. Therefore it is of great interest to see how this type of oxide resists different corrosive environments and how it changes with time. This can be done by exposing the samples for a longer time. Figure 48 shows a 304L sample exposed for 1000 hours in a corrosive atmosphere. Here the corrosion product layer has grown thicker and metal chloride has formed in the oxide/metal interface.
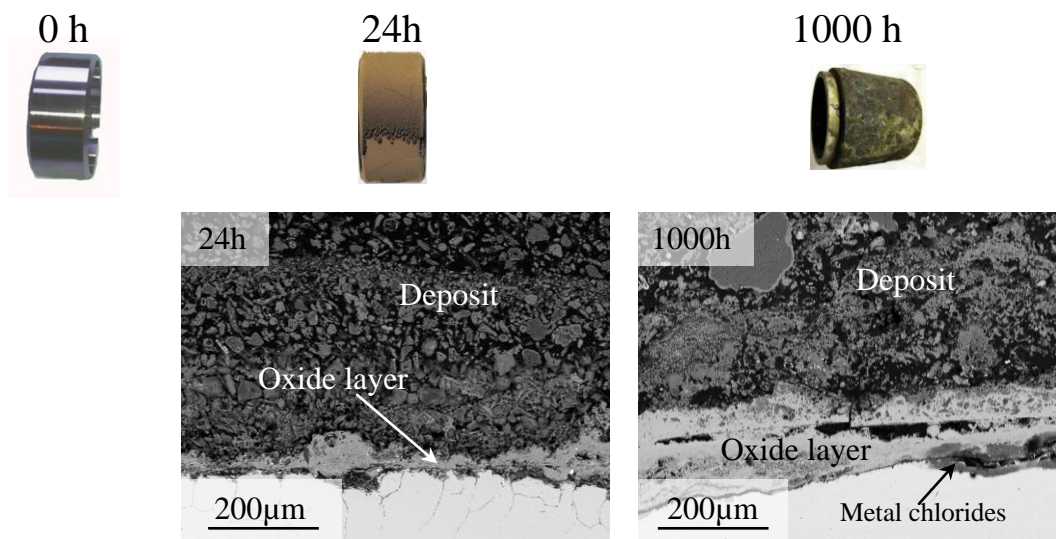

Figure 48: Top row: 304L sample rings exposed for 0, 24 and 1000 in a corrosive environment. Bottom row: Cross-section of 304L sample exposed for 24 and 1000 hours in a corrosive environment [80]

Long-time exposures are very time consuming. It is also very difficult to evaluate the corrosion attack after a long period of exposure in a boiler. One way of solving this

problem is to change the starting conditions and begin the studies when the corrosion attack has already started on the sample, i.e. in the propagation step. This can be done by pre-oxidizing the samples in a specific corrosive environment in order to break the protective oxide to form a less protective oxide. After that the sample is exposed again in a desired atmosphere in order to investigate how the oxide layer resists further oxidation in different environments.

To investigate the propagation step of 304L, samples was pre-oxidized for 24 hours in two different environments: in 5% O_2 + 40% H_2O and in 5% O_2 + 40% H_2O + small amounts of KCl. As described in section 3.3, the presence of H_2O results in the formation of oxide islands, consisting of an outward-growing hematite and an inward-growing spinel oxide. The surface between the islands consists of a thin, chromium-rich oxide. As shown in Section 6.1, the presence of small amounts of KCl results in a thick covering oxide with a composition similar to the oxide-islands. The surface morphology and oxide morphology for the pre-oxidized samples are shown in Figure 47.

Non-pre-oxidized   Pre-oxidized in H_2O Pre-oxidized in H_2O + KCl
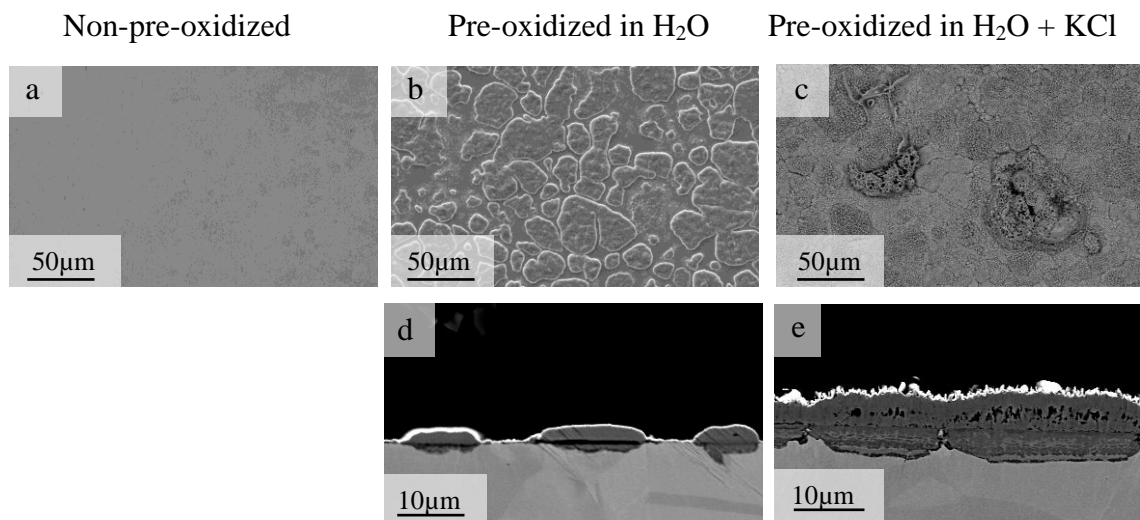
Figure 49: BSE images of 304L samples exposed for a) 0h, b) 24h in 5% O_2 + 40% H_2O, c) 24h in 5% O_2 + 40% H_2O + 1.35 mg/cm^2 KCl. BSE images of BIB cross-section of 304L sample exposed for d) 24h in 5% O_2 + 40% H_2O, e) 24h in 5% O_2 + 40% H_2O + 1.35 mg/cm^2 KCl

After the pre-oxidation step both samples, including an unexposed sample, were sprayed with small amounts of KCl and exposed for 24 hours. This resulted in a similar surface morphology for all samples, i.e. an iron-rich oxide covers the surface (see Figure 50).

67

However, on the sample pre-oxidized in H_2O (Figure 50b), no signs of former salt particles are found on the sample. For samples pre-oxidized with KCl, former salt particles are visible but they were most probably formed during the pre-oxidation step since they have not increased in number (Figure 50c).
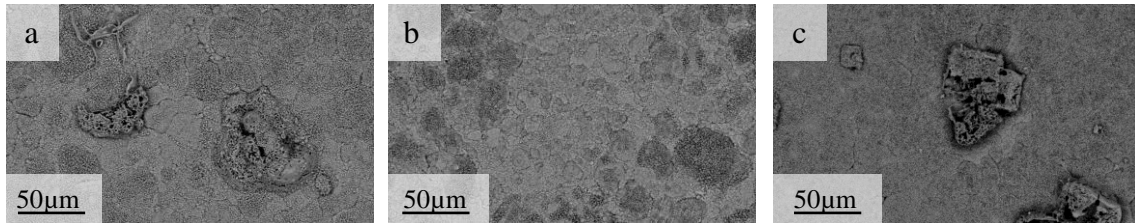
Figure 50: BSE images of 304L samples exposed for 24h with 1.35 mg/cm² KCl where the starting condition was an a) unexposed sample, b) a sample pre-oxidized for 24h in 5% O_2 + 40% H_2O, and c) a sample pre-oxidized for 24h in 5% O_2 + 40% H_2O + 1.35 mg/cm² KCl.

The corrosion morphology is also very similar for all samples (see Figure 50). All three oxides consist of an outward-growing hematite and an inward-growing Fe-Cr-Ni-spinel and the thickness is about 10 µm. Furthermore, there are no signs of unreacted KCl or metal chlorides on any sample.
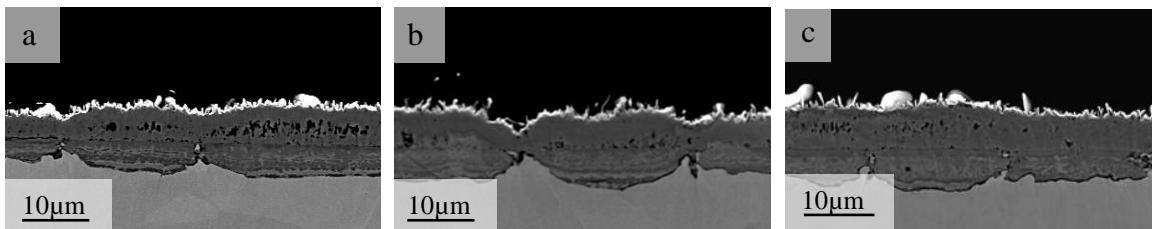
Figure 51: BSE images of cross-section of 304L samples exposed for 24h with 1.35 mg/cm² KCl where the starting condition was a) an unexposed sample, b) a sample pre-oxidized for 24h in 5% O_2 + 40% H_2O, c) a sample pre-oxidized for 24h in 5% O_2 + 40% H_2O + 1.35 mg/cm² KCl

The reason for the breakdown of the protective scale in the presence of KCl in this environment is chromate formation (see section 6.1 and reaction 6.1). For chromate formation to be possible, potassium must come in direct contact with the chromium-rich oxide that initially forms on 304L. According to IC analysis of the non-pre-oxidised sample, about 20% of the original K^+ had formed K_2CrO_4 while most of the remaining K^+ had evaporated as KCl(g). For samples pre-oxidized with water vapour only 6% of the applied salt formed K_2CrO_4 while the remaining part evaporated. The reason for the lower chromate formation on samples pre-oxidized in water vapours is explained by the oxide

islands formed in the pre-oxidation step. Due to those, most of the surface is covered by an iron-rich oxide. Since chromate-formation only is possible when chromium is available, this reaction could only take place in the area between the oxide islands where a thin chromium-rich oxide was still present. Most of the salt was, however, applied on an iron-rich oxide and therefore the chromate formation was limited. For samples pre-oxidized with KCl, the starting condition was a sample totally covered by an iron-rich oxide and no further chromate formation was possible when the new salt was applied.

Since there were no signs of metal-chloride formation it seems the iron-rich oxide, which forms on 304L in this laboratory environment, protects the steel from small amounts of KCl. Thus KCl does not react with the oxide layer formed on 304L at these conditions and therefore evaporates as KCl(g). Hence there are no signs of former salt particles on the samples pre-oxidized in H_2O and only former salt particles from the pre-oxidation step on samples pre-oxidized with KCl.

However, the atmosphere in a waste-fired boiler is much more complex; there are higher amounts of alkali chlorides and HCl and SO_2 in varying amounts. There are also many particles from the flue gas that stick to the sample surface which may result in a mix of oxide and deposit. This mix becomes more porous compared to the oxide formed in the laboratory (i.e. without a deposit) and might therefore result in a faster oxide growth and penetration of chlorine ions. In addition, exposures on Fe-2.25Cr-1Mo, which forms a similar iron-rich oxide as for 304L, at 400-500° C, showed that the presence of small amounts of KCl resulted in corrosion attack induced by chlorine [81]. Therefore it is of great interest to continue to investigate the propagation step in a more complex environment, e.g. with larger amounts of salt or in the presence of SO_2 and/or HCl and with different materials at different temperatures.

6.4. Corrosion memory

The corrosion rate is often considered to be directly linked to the degree of corrosiveness of the current fuel mix being burnt. However, the corrosion attack is also affected by the corrosion history, i.e. previous deposit build-up and oxide scale formation. This can be referred to as corrosion memory. In section 6.3 it was shown that if a small amount of KCl is sprayed on a 304L sample, covered by an iron-rich oxide, the KCl does not react and therefore evaporates. Thus hematite, in this specific case, protects the steel from small amounts of KCl since it separated the material surface and the salt. However, note that this is a very simplified laboratory experiment and a hematite layer does not act as a protective layer in a boiler where the corrosive environment is much more complex. Therefore the layer that separates the steel from the corrosive atmosphere must have a much better composition in order to protect the steel from the corrosive atmosphere in a waste-fired boiler.

As shown in section 6.2, the co-combustion of waste and sulphur-rich municipal sewage sludge resulted in a reduced corrosion rate. In the case *MSS2-high*, where the amount of sulphur was sufficient to sulphate all the alkali chloride, no corrosion product layer was formed after 24 hours of exposure. Instead, the sample was covered by a non-corrosive deposit rich in alkali sulphate. Hence, if the boiler operates with non-corrosive fuel a relatively benign deposit forms on the steel surface and the corrosion attack is therefore expected to be mild. The question is though, can this non-corrosive deposit act as a protective layer if the fuel mix changes and becomes more aggressive (e.g. having a higher content of alkali chlorides)? If so, varying the fuel composition in the right way can be an alternative for reduction in steam temperature in the boiler which is often done in order to decrease the corrosion rate when burning corrosive fuels.

In order to investigate how the corrosion is affected by variations of the fuel mixed and to see if there is a memory effect from the corrosion history, a three-step exposure program was performed in two CFB boilers, owned by E.ON Värme AB, located in Händelö, Norrköping) with different environments. In the first step a test-probe was exposed for 313 hours in a biomass-fired boiler (less corrosive environment). In the second step, the probe was moved to a waste-fired boiler (high corrosive environment) and exposed for further 256 hours. In the third step, the probe was moved back to the moderate corrosive

environment in the biomass-fired boiler and exposed for 162 hours. In addition, after each step, the outermost samples were replaced by new once to be able to analyze each step separately. As a reference, an identical probe was exposed for 711 hours (the total time of step 1-3) in a biomass-fired boiler. For more information about the exposure set-up, the boilers and fuel specifications, see section 5.1 and Paper VI.

Exposures in the less corrosive environment for 213 hours (step 1) resulted in a very thin corrosion product layer. The oxide is covered by an approximately 100 µm thick deposit which consists of alkali sulphates [82]. After 711 hours of exposure (the reference exposure) the deposit had the same composition and the oxide scale thickness had increased slightly (up to 15 µm thick). In addition, there were no signs of metal chlorides or sulphate (Figure 52).
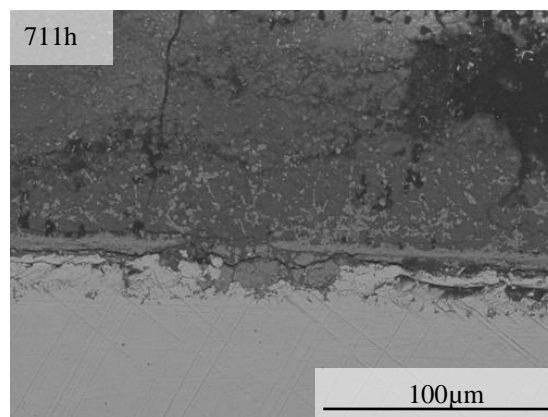
Figure 52: BSE images of polished cross-sections after 711 hours of exposure in the biomass-fired boiler

Exposures for 236 hours in a corrosive environment (only step 2) generated large amounts of deposit and much of this was lost during handling and is therefore not shown in the cross-section in Figure 53a. The corrosion products layer is about 100 µm thick and can be divided into three different layers: a layer of iron and nickel-rich with some chlorine (inner part), a layer of mainly iron chloride (middle part) and layer of a metal chloride matrix with some embedded regions consisting of chromium-rich oxides (other part).

The samples exposed in the biomass/waste/biomass-environment (i.e. step 1-3) imitate the effect of varying the fuels in the boiler in order to decrease the corrosion attack. Again

large amounts of deposits were formed which resulted in spallation during sample handling and preparation. However, some parts of the deposit remained on the sample and consisted of sodium, potassium and sulphur (see Figure 53b). The corrosion product layer consists of an outer chromium-rich and an inner nickel-iron-rich part. In some regions a small amount of chlorine and/or sulphur is detected. The thickness of the oxide is somewhat thinner than the oxide layer formed in the waste-fired boiler (Figure 53a). By contrast, the sample exposed in biomass/waste/biomass-environment was exposed for a total of 711 hours, while the sample in the waste-fired boiler was exposed for only 236 hours.
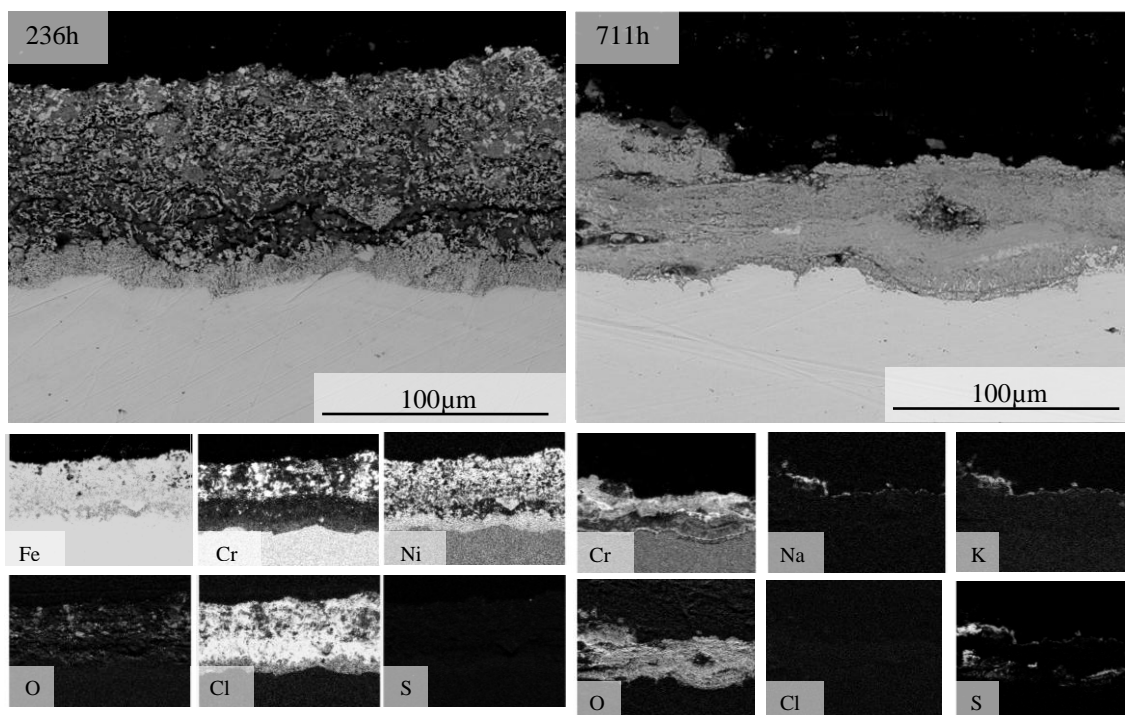
Figure 53: BSE images of polished cross-section of a sample exposed in a) waste-fired boiler for 236h (step 2 only) and b) biomass boiler for 313h + waste-fired boiler for 236h + biomass boiler for 162h (step 1-3)

By switching from a corrosive fuel (step 2) to a less corrosive fuel (step 3), the corrosive deposit formed in step 2 is converted to a K_2SO_4-rich and less corrosive deposited. As shown in section 6.2, sulphation of an alkali chloride-rich deposit can result in chlorination and sulphidation of the steel grain boundaries. However, since the first exposure (step 1) was performed in less corrosive environment, a thin oxide was formed, covered by a non-corrosive deposit. This initial deposit/corrosion product layer acts therefore as a protection against the corrosive environment in step 2. However, since the

72

non-corrosive deposit (formed in step 1) was so thin it could not resist the corrosive atmosphere in step 2 and after the last exposure (in the less corrosive atmosphere) the oxide thickness is almost five times thicker than in the reference case (Figure 52). Important to emphasise is though that the corrosion product layer formed in the varied environment, with a total exposure time of 711 hours (Figure 53b), was thinner compared to the corrosion product layer formed after only 236 hours of exposure in just a corrosive environment (Figure 53b). Furthermore, almost no metal chlorides were found after exposures in a varied environment. Thus the exposures with a less corrosive fuel (step 1) gave protection against the corrosive environment in step 2 even if this protection was inadequate. In addition, the final step (in the less corrosive environment) sulphated the corrosive alkali chlorides formed in step 2. The result from the exposures performed in biomass/waste/biomass-environment shows that the corrosion rate can be reduced by varying the fuel composition in the right way.

7. Conclusions

Combustion of biomass and waste often results in a flue gas with high amounts of alkali chlorides and low concentrations of SO_2. This in turn leads to formation of thick deposits rich in corrosive alkali chlorides. Exposures with stainless steel, 304L at 600°C for 24 hours, in a waste-fired boiler show that a corrosive environment results in a corrosion morphology consisting of two types of corrosion attack: general corrosion and steel grain boundary attack. The general corrosion has been proved to be initiated by chromate formation while the steel grain boundary attack is suggested to be chlorine induced.

Previous studies in the laboratory have shown that small amounts of KCl accelerate the corrosion attack of stainless steels. This was explained by the formation of K_2CrO_4 which depletes the protective oxide in chromium and a poorly protective and fast growing iron-rich oxide is formed instead. The present study showed that NaCl is as corrosive as KCl and the formation of Na_2CrO_4 depletes the protective oxide in chromium, resulting in a thick oxide scale. Similar to KCl and NaCl, $CaCl_2$ may also deplete the protective oxide in chromium by the formation of $CaCrO_4$. However, under the experimental conditions in the investigation, $CaCl_2$ was rapidly converted to CaO. Calcium oxide may also form $CaCrO_4$ but due to the poor mobility of CaO the reaction was limited.

By increasing the amount of KCl in the laboratory exposures, the general corrosion increased slightly resulting in an increased scale thickness. The most remarkable change in corrosion morphology was, however, the greatly increased oxidation along the steel grain boundaries. This attack is expected to be accelerated by the presence of chlorine, released as HCl from the chromate formation reaction.

By using sulphur-containing additives or by co-combustion with a sulphur-rich fuel, the corrosive environment in a waste-fired boiler can be mitigated. This is due to the conversion of corrosive alkali chlorides to less corrosive alkali compounds, e.g. alkali sulphates. The non-corrosive behaviour of alkali sulphates has earlier been explained by its inability to react with the chromium-rich oxide to form alkali chromates.

In this thesis it has been shown that co-firing waste (Solid Recovered Fuel) with municipal sewage sludge decreased the corrosion rate of stainless steels. If the amount of sludge was sufficiently high, most of the alkali chlorides were converted to alkali

sulphates in the flue gas and the steel material was covered by a non-corrosive deposit. This type of less corrosive deposit was also proved to be able to act as a protective layer against corrosion attacks if the flue gas became more corrosive.

With decreased amounts of sludge (i.e. insufficient to transform most of the alkali chlorides to less corrosive alkali compounds in the flue gas) similar corrosion morphology as for samples exposed without sludge was found on the sample. However, the corrosion attack was not as severe as the corresponding exposure without sludge. Here it is proposed that the corrosion attack was initiated by deposition of alkali chlorides. Since there were no signs of alkali chlorides in the deposit it is supported that the alkali chlorides have been converted to alkali sulphates on the steel surface.

Laboratory exposures of 304L sprayed with small amounts of KCl and exposed in the presence of SO_2 showed that a simultaneous formation of alkali chromate and alkali sulphate occurred. The chromate formation reaction results in chromium depletion and an iron-rich oxide is formed. The oxide growth in the presence of SO_2 was however significantly reduced compared to corresponding KCl exposure in the absence of SO_2. This is attributed to the very fast sulphation reaction between KCl and SO_2, decreasing the probability to form K_2CrO_4. Furthermore, it is also expected that SO_2 forms a thin sulphate layer on the top of the oxide decreasing the inward diffusion of oxygen.

The general corrosion attack decreased with the presence of SO_2 but the corrosion attack along the steel grain boundaries went in the opposite direction, i.e. the presence of both KCl and SO_2 accelerated the corrosion attack. The accelerated steel grain boundary attack is expected to be related to a dramatic increase of HCl due to the extremely fast sulphation reaction. In addition, the presence of SO_2 also resulted in metal sulphides. Thus, the availability of both chlorine and sulphide is suggested to be important factors for the steel grain boundary attack.

8. Acknowledgements

First of all I would like to thank my supervisors: Professor Jan-Erik Svensson, Professor Lars-Gunnar Johansson, Assisting Professor Jesper Liske and Ph.D. Torbjörn Jonsson, for the support and all the knowledge you have shared with me. I have really enjoyed working with you!

Moreover, I would like to acknowledge the High Temperature Centre (HTC), Konsortiet för Materialteknik för termiska energiprocesser (KME), Värmeforsk (VF) and the Swedish Energy Agency (SEA), with their member companies, for support and funding.

Special thanks to Docent Lars-Erik Åmand at the Department of Energy and Environment for support and nice collaboration during the work with paper III, Ph. D. Josefin Hall for performing the AES analysis in paper IV, Håkan Kassman, Research Engineer at Vattenfall, for contributing with knowledge during the authoring of Paper III and this thesis, Senior Research Engineer Anders Kvist for support with the Microscopy, Professor Vratislav Langer for support with X-ray diffraction, Sandra Gustavsson for assistance with administrative matters and Esa Väänänen and Erik Brunius for technical support.

I would also like to thank and give a huge hug to all my colleagues (both former and present) in the corrosion group as well as the rest of the Department of Chemistry and Chemical Engineering for making it so pleasant to work there. An extra hug goes to my office mate, Assisting Professor Kristina Hellström, for all the nice conversations that we have shared; both the scientific ones and those of another nature.

Finally, I would like to thank my favourite colleague Erik, for being the perfect partner, and our lovely girls Stella and Thea, for giving me so much joy in life. You three are the best of the best!

9. Reference List

1. Metz, B., Davidson, O., de Coninck, H. C., Loos, M., Meyer, L.A., *IPCC Special Report on Carbon Dioxide Capture and Storage. Prepared by Working Group III of the Intergovernmental Panel on Climate Change*, Cambridge University Press, Cambridge, (2005).

2. http://www.climatechoices.org.uk.

3. http://www.endangeredpolarbear.com/.

4. http://www.educapoles.org/.

5. Michelsen, H.P., Frandsen, F., Dam-Johansen, K., Larsen, O. H., Deposition and high temperature corrosion in a 10 MW straw fired boiler. *Fuel Processing Technology*, (1998), **54**(1–3), pp. 95–108.

6. Kassman, H., Pettersson, J., Steenari, B.-M., Åmand, L.-E., Two strategies to reduce gaseous KCl and chlorine in deposits during biomass combustion - injection of ammonium sulphate and co-combustion with peat. *Fuel Processing Technology*, (2013), **105**, pp. 170-180.

7. Miles, T.R., Baxter, L.L., Bryers, R.W., Jenkins, B. M., Oden, L.L., Boiler deposits from firing biomass fuels. *Biomass and Bioenergy*, (1996), **10**(2-3), pp. 125–138.

8. Jenkins, B.M., Baxter, L. L., Miles, T. R., Combustion properties of biomass. *Fuel Processing Technology*, (1998), **54**(1–3), pp. 17–46.

9. Davidsson, K.O., Åmand, L.-E., Leckner, B., Kovacevik, B., Svane, M., Hagström, M., Pettersson, J.B.C., Pettersson, J., Asteman, H.,Svensson, J.-E., and Johansson, L.-G., Potassium, Chlorine, and Sulfur in Ash, Particles, Deposits, and Corrosion during Wood Combustion in a Circulating Fluidized-Bed Boiler. *Energy Fuels*, (2007), **21 (1**), pp. 71–81.

10. Aho, M., Paakkinen, K., Taipale, R, Quality of deposits during grate combustion of corn stover and wood chip blends. *Fuel*, (2013), **104**, pp. 476–487.

11. Karlsson, S., Åmand, L.-E., Liske, J. Reducing high-temperature corrosion on high-alloyed stainless steel superheaters by co-combustion of municipal sewage sludge in a fluidised bed boiler. *Fuel*, (2015), **139**, pp. 482–493.

12. Grabke, H.J., Reese, E., Spiegel, M., The effects of chlorides, hydrogen chloride, and sulfur dioxide in the oxidation of steels below deposits. *Corrosion Science*, (1995), **37**(7), pp. 1023–43.

13. Jonsson, T., Froitzheim, J., Pettersson, J., Svensson, J.-E., Johansson, L.-G., Halvarsson, M., The Influence of KCl on the Corrosion of an Austenitic Stainless Steel (304L) in Oxidizing Humid Conditions at 600 degrees C: A Microstructural Study. *Oxidation of Metals*, (2009), **73**(3–4), pp. 213–239.

14. Karlsson, S., Pettersson, J., Johansson, L.-G., Svensson, J.-E., Alkali Induced High Temperature Corrosion of Stainless Steel – The influence of NaCl, KCl and CaCl2. *Oxidation of Metals*, (2012), **78**(1-2), pp. 83-102.

15. Pettersson, C., Pettersson, J., Asteman, H., Svensson, J.-E., Johansson, L.-G., , KCl-induced high temperature corrosion of the austenitic Fe–Cr–Ni alloys 304L and Sanicro 28 at 600 °C *Corrosion Science*, (2006), **48**(6), pp. 1368–1378.

16. Pettersson, J., Asteman, H., Svensson, J.-E., Johansson, L.-G., KCl Induced Corrosion of a 304-type Austenitic Stainless Steel at 600°C; The Role of Potassium. *Oxidation of Metals*, (2005), **64**(1–2), pp. 23–41.

17. Pettersson, J., Svensson, J.-E., Johansson, L.-G., KCl-Induced Corrosion of a 304-type Austenitic Stainless Steel in O-2 and in O-2 + H2O Environment: The Influence of Temperature. *Oxidation of Metals*, (2009), **72** (3-4), pp. 159-177.

18. Pickering, H., Beck, F., Fontana, M., Rapid Intergranular Oxidation of 18-8 Stainless Steel by Oxygen and Dry Sodium Chloride at Elevated Temperatures. *Transactions of the ASM*, (1961), **53**, pp. 793-803.

19. Nielsen, H.P., Frandsen, F. J., Dam-Johansen, K., Baxter, L. L., The implications of chlorine-associated corrosion on the operation of biomass-fired boilers *Progress in Energy and Combustion Science*, (2000), **26**(3), pp. 283–298.

20. Shinata, Y., Accelerated oxidation rate of chromium induced by sodium chloride. *Oxidation of Metals*, (1987), **27**(5-6), pp. 315-332.

21. Wang, C.-J., He, T.-T., Morphological development of subscale formation in Fe-Cr-(Ni) alloys with chloride and sulfates coating. *Oxidation of Metals*, (2002), **58**(3–4), pp. 415–437.

22. Kiamehr, S., *Material Solutions to Mitigate the Alkali Chloride-Induced High Temperature Corrosion* in *Department of Mechanical Engineering*. 2014, Technical University of Denmark (DTU), Lyngby, Denmark.

23. Kiamehr, S.D.K.V., Montgomery, M., Somers, M. A. J., KCl-induced high temperature corrosion of selected commercial alloys. Part II: alumina and silica-formers. *Materials and Corrosion*, (2015).

24. Pettersson, J., Pettersson, C., Folkeson, N., Johansson, L.-G., Skog, E., Svensson, J.-E., The influence of sulphur additions on the corrosive environment in a waste-fired CFB boiler. *Materials Science Forum*, (2006), **522–523**, pp. 563–570.

25. Folkeson, N., Pettersson, J., Pettersson, C., Johansson, L.-G., Skog, E., Andersson, B.-Å., Enestam, S., Tuiremo, J., Jonasson, A., Heikne, B., Svensson, J.-E., Fireside corrosion of stainless and low alloyed steels in a waste-fires CFB boiler: The effect of adding sulphur to the fuel. *Materials Science forum*, (2008), **595-598**, pp. 289–297.

26. Davidsson, K.O., Åmand, L.-E., Steenari, B.-M., Elled, A.-L., Eskilsson, D., Leckner, B., Countermeasures against alkali-related problems during combustion of biomass in a circulating fluidized bed boiler. *Chemical Engineering Science*, (2008), **63**(21), pp. 5314-5329.

27. Kassman, H., L. Bäfver, L.-E. Åmand., The importance of SO2 and SO3 for sulphation of gaseous KCl – An experimental investigation in a biomass fired CFB boiler. *Combustion and Flame*, (2010), **157**(9), pp. 1649-1657.

28. Krause, H.H., Vaughan, D.A., Boyd, W.K., Corrosion and Deposits From Combustion of Solid Waste—Part III: Effects of Sulfur on Boiler Tube Metals. *Journal for Engineering for Power*, (1975), **97**(3), pp. 448-452.

29. Aho, M., Yrjas, P., Taipale, R., Hupa, M., Silvennoinen, J., Reduction of superheater corrosion by co-firing risky biomass with sewage sludge. *Fuel*, (2010), **89**(9), pp. 2376-2386.

30. Jonsson, T., Pettersson, J., Davidsson, K., Johansson, L.-G., Svensson J.-E., *Sewage sludge as additive to reduce the initial fireside corrosion caused by combustion of shredder residues in a waste-fired BFB boiler.*, in *9th Liège Conference on Materials for Advanced Power Engineering.* 2010.

31. Vainio, E., Yrjas, P., Zevenhoven, M., Brink, A., Laurén, T., Hupa, M., Kajolinna, T., Vesala, H., The fate of chlorine, sulfur, and potassium during co-combustion of bark, sludge, and solid recovered fuel in an industrial scale BFB boiler. *Fuel Processing Technology*, (2013), **105**, pp. 59-68.

32. Elled, A.-L., Davidsson, K.-O., Åmand, L.-E., Sewage sludge as a deposit inhibitor when co-fired with high potassium fuels. *Biomass and Bioenergy*, (2010), **34**, pp. 1546-1554.

33. Andersson, S., Blomqvist, E.W., Bäfver, L., Jones, F., Davidsson, K., Froitzheim, J., Karlsson, M., Larsson, E., Liske, J., Sulfur recirculation for increased electricity production in Waste-to-Energy plants. *Waste Management*, (2014), **34**(1), pp. 67-78.

34. Viklund, P., Pettersson, R., Hjörnhede, A., Effect of sulphur containing additive on initial corrosion of superheater tubes in waste fired boiler. *Corrosion Engineering, Science and Technology*, (2009), **44**(3), pp. 234-240.

35. Åmand, L.-E., Leckner. B., Eskilsson, D., Tullin, C., Ash deposits on heat transfer tubes during co-combustion of biofuels and sewage sludge. *Fuel*, (2006), **85**, pp. 1313-1322.

36. Davidsson, K.O., Åmand, L.-E., Elled, A.-L., Leckner, B., Effect of Cofiring Coal and Biofuel with Sewage Sludge on Alkali Problems in a Circulating Fluidized Bed Boiler. *Energy & Fuels*, (2007), **21,** pp. 3180-3188.

37. Viklund, P., Kassman, H., Åmand, L.-E., Deposit chemistry and initial corrosion during biomass combustion – The influence of excess O2 and sulphate injection. *Materials and Corrosion*, (2015), **66**(2), pp. 118-127.

38. Alipour, Y., Talus, A., Henderson, P., Norling, R., he effect of co-firing sewage sludge with used wood on the corrosion of an FeCrAl alloy and a nickel-based alloy in the furnace region. *Fuel Processing Technology*, (2015).

39. Kofstad, P., *High Temperature Corrosion*, Elsevier Applied Science, London, (1988). pp. 558.

40. Khanna, A.S., *Introduction to High Temperature Oxidation and Corrosion*, ASM International, Delhi, (2002). pp. 325.

41. *http://www.doitpoms.ac.uk/tlplib/recycling-metals/ellingham.php*.

42. West, A.R., *Basic solid state chemistry*, 2nd edn., John Wiley and Sons, Chichester, (1999). pp. 480.

43. Briks, N., Meier, G. H., Pettit, F. S., *Introduction to the High Temperature Oxidation of Metals*, 2 edn., Cambridge University Press, Cambridge, (2006). pp. 352.

44. Murch, G.E., *Diffusion in Crystalline Solids*, Academic Press, Florida, (1984).

45. Kaur, I., Mishin, Y., Gust, W., *Fundamentals of Grain and Interphase Boundary Diffusion*, Wiley, New York, (1995).

46. Wagner, C., Beitrag zur Theorie des Anlaufvorgangs. *Zeitschrift für Physikalische Chemie*, (1933), **B21**, pp. 25–41.

47. Honeycombe, R.W.K., Bhadeshia, H. K. D. H., *Steels: Microstructure and Properties*, 2 edn., Butterworth-Heinemann, Oxford, (1995). pp. 324.

48. Callister Jr, W.D., *Materials Science and Engineering: An Introduction*, 5th edn., John Wiley & Sons, New York, (1999).

49. Asteman, H., Svensson, J. E., Johansson, L. G., Norell, M., Indication of chromium oxide hydroxide evaporation during oxidation of 304L at 873 K in the presence of 10% water vapor. *Oxidation of Metals*, (1999), **52**(1-2), pp. 95-111.

50. Asteman, H., Svensson, J.-E., Norell, M., Johansson, L.-G., Influence of Water Vapor and Flow Rate on the High-Temperature Oxidation of 304L; Effect of Chromium Oxide Hydroxide Evaporation. *Oxidation of Metals*, (2000), **54**(1–2), pp. 11–26.

51. Tang, J.E., Halvarsson, M., Asteman, H., Svensson, J.-E., The microstructure of the base oxide on 304L steel. *Micron*, (2001), **32**(8), pp. 799–805.

52. Halvarsson, M., Tang, J-E., Asteman, H., Svensson, J.-E., Johansson, L.-G., Microstructural investigation of the breakdown of the protective oxide scale on a 304 steel in the presence of oxygen and water vapour at 600°C. *Corrosion Science*, (2006), **48**(8), pp. 2014–2035.

53. Jonsson, T., Järdnäs, A., Svensson, J.-E., Johansson, L.-G., M. Halvarsson, The Effect of Traces of SO2 on Iron Oxidation: A Microstructural Study. *Oxidation of Metals*, (2007), **67**(3), pp. 193-213.

54. Järdnäs, A., *The Influence of SO2 on the High Temperature Corrosion of Fe and Fe-Cr Alloys*, in *Department of Chemical and Biological Engineering*. 2005, Chalmers University of Thechnology: Göteborg.

55. Jonasson, A. Personal communication. E.ON Norrköping, Sweden. (August 2011).

56. Yin, C., Rosendahl, L.A., Kær, S.K., Grate-firing of biomass for heat and power production. *Progress in Energy and Combustion Science*, (2008), **34**(6), pp. 725–754.

57. Peña, J.A.P., *Bubbling Fluidized Bed (BFB), When to use this technology?*, in *IFSA 2011, Industrial Fluidization South Africa*. 2011: Johannesburg, South Africa.

58. Viklund, P., *Superheater corrosion in biomass and waste fired boilers – Characterisation, causes and prevention of chlorine-induced corrosion*, in *Chemistry*. 2013, Kungliga Tekniska Högskolan: Stockholm.

59. Pettersson, J., *Alkali Induced High Temperature Corrosion of Stainless Steel - Experiences from Laboratory and Field*, in *Department of Chemical and Biological Engineering*. 2008, Chalmers University of Technology: Gothenburg. p. 84.

60. Folkeson, N., Johansson, L. G. Svensson, J. E., Initial stages of the HCl-induced high-temperature corrosion of alloy 310. *Journal of the Electrochemical Society*, (2007), **154**(9), pp. 515-521.

61. Lehmusto, J., Skrifvars, B.-J., Yrjas, P., Hupa, M., Comparison of potassium chloride and potassium carbonate with respect to their tendency to cause high temperature corrosion of stainless 304L steel. *Fuel Processing Technology*, (2013), **105**, pp. 98-105.

62. Proff, C., Jonsson, T., Pettersson, C., Svensson, J.-E., Johansson, L.-G., Halvarsson, M., Microstructural investigation of the KCl-induced corrosion of the austenitic alloy Sanicro 28 (35Fe27Cr31Ni) at 600°C. *Materials at High Temperature*, (2009), **26**(2), pp. 113–125.

63. Pettersson, J., Folkeson, N., Svensson, J.-E., Johansson, L.-G. , The Effects of KCl, K2SO4 and K2CO3 on the High Temperature Corrosion of a 304-type Austenitic Stainless Steel. *Oxidation of Metals*, (2011), **76**(1-2), pp. 93-109.

64. Barin, I., *Thermodynamic Data of Pure Substances*, Third Edition edn., Weinheim, New York, (1995). pp. 1885.

65. Factsage, *Center for Reserch in Computational Thermochemistry, École Polytechnique de Montréale Génie Chemique, Montreal Canada*.

66. Herstad Svärd, S., Åmand, L.-E., Bowalli, J., Öhlin, J., Steenari, B.-M., Pettersson, J., Svensson, J.-E., Karlsson, S.,Larsson, E., Johansson, L.-G., Davidsson, K., Bäfver, L., Almark, M. , *Frame work - Measures for simultaneous minimization of alkali related operating problems, Phase 3* Värmeforsk, Göteborg, Sweden, (2011).

67.   Paz, M.D., Jonsson, T., Liske, J., Karlsson, S., Davis, C., Jonasson, A., Sandberg, T., *Study of corrosion memory in boiler heat surfaces by field tests with biomass fuel mixes including sulphur and refuse fractions.*, (2015).

68.   https://www.wikipedia.org/.

69.   Folkeson, N., *Chlorine Induced Corrosion in Biomass and Waste Fired Boilers: Laboratory and Field Investigations*, in *Department of Chemical and Biological Engineering*. 2010, Chalmers University of Technology: Göteborg.

70.   Goldstein, J., Newbury, D. E., Echlin, P., Joy, D. C., Romig Jr, A. D., Lyman, C. E., Fiori, C., Lifshin, E., *Scanning Electron Microscopy and X-Ray Microanalysis: A Text for Biologists, Materials Scientists and Geologists* Kluwer Academic/Plenum Publishers, Dordrecht, Netherlands, (1992). pp. 840.

71.   Williams, D.B., Carter, C.B. , *Transmission Electron Microscopy, 2nd edition.*, Springer, New York, (2009).

72.   Pettersson, C., Svensson J.-E., Johansson, L.-G., Corrosivity of KCl(g) at Temperatures Above its Dew Point - Initial Stages of the High Temperature Corrosion of Alloy Sanicro 28 at 600°C. *Materials Science Forum* (2006), **522-523**, pp. 539-546.

73.   Jonsson, T., Karlsson, S., Hooshyar, H.H., Sattari, M., Svensson, J.-E., Johansson, L.-G., Oxidation after breakdown of the chromium rich scale on stainless steels at high temperature – internal oxidation. *Submitted to Oxidation of Metals*.

74.   Van Orman, J.A., Crispin, K. L., Diffusion in Oxides. *Mineralogy & Geochemistry*, (2010), **72** pp. 757-825.

75.   Töpfer, J.A., S. and Dieckmann, R., Point Defects and Cation Tracer Diffusion in $(Cr_xFe_{1-x})_{3-\delta}O_4$ Spinels. *Solid State Ionics*, (1995), **81**(3-4), pp. 251-266.

76.   Karlsson, S., Jonsson, T., Svensson, J.-E., Liske, J., A laboratory study of the in-situ sulphation of alkali chloride rich deposits – A corrosion perspective. *Manuscript*.

77.   Pettersson, C., Johansson, L.-G., Svensson, J.-E., The Influence of Small Amounts of KCl(s) on the Initial Stages of the Corrosion of Alloy Sanicro 28 at 600 °C *Oxidation of metals*, (2008), **70**(5–6), pp. 241–256.

78.   Karlsson, S., Jonsson, J.,Hall, J., Svensson, J.-E., Liske, J., Mitigation of Fireside Corrosion of Stainless Steel in Power Plants: A Laboratory Study of the Influences of SO2 and KCl on Initial Stages of Corrosion. *Energy Fuels*, (2014), **28**(5), pp. 3102–3109.

79.   Järdnäs, A., Svensson, J.E., Johansson, L.G., The Inhibitive Effect of Traces of SO2 on the Oxidation of Iron. *Oxidation of Metals*, (2002), **60**(5-6), pp. 427-445.

80.   Pettersson, J., Svensson, J.-E., Skog, E., Johansson, L.-G., Folkeson, N., Froitzheim, J., Karlsson, S., Larsson, E., Israelsson, N., Enestam, S., Tuiremo, J., Jonasson, A., Arnesson, B., Andersson B.-Å., Heikne, B. , *Evaluation of different fuel additives ability to master corrosion and deposition on steam superheaters in a waste fired CFB-boiler*, (2010).

81.   Folkeson, N., Jonsson, T. Halvarsson, M. Johansson, L.-G., Svensson J.-E., The influence of small amounts of KCl(s) on the high temperature corrosion of a Fe-2.25Cr-1Mo steel at 400 and 500°C. *Materials and Corrosion*, (2011), **62**(7), pp. 606–610.

82.   Paz, M.D., Zhao, D., Karlsson, S., Liske, J., Jonsson, T., *Investigating Corrosion Memory – The influence of historic boiler operation on current corrosion rate*, in *Impacts of Fuel Quality on Power Production* 2014: Utah, USA.